Electronic Structure Calculations on Bulk and Surfaces of Some Transition-Metal and f-Electron Compounds

Engin Torun

Electronic Structure Calculations on Bulk and Surfaces of Some Transition-Metal and f-Electron Compounds

Proefschrift

ter verkrijging van de graad van doctor
aan de Radboud Universiteit Nijmegen
op gezag van de rector magnificus prof. dr. Th.L.M. Engelen,
volgens besluit van het college van decanen
in het openbaar te verdedigen op donderdag 9 april 2015
om 14:30 uur precies.

door

Engin Torun
geboren op 2 maart 1983
te Tunceli, Turkije

Promotor:	Prof. dr. R. A. de Groot
Copromotor:	Dr. ir. G. A. de Wijs

Manuscriptcommissie:	Prof. dr. ir. G. C. Groenenboom (voorzitter)
	Prof. dr. A. Fasolino
	Prof. dr. T. T. M. Palstra (Rijksuniversiteit Groningen)

Engin Torun, Electronic Structure Calculations on Bulk and Surfaces of Some Transition-Metal and f-Electron Compounds
PhD Thesis, Radboud University Nijmegen, The Netherlands
With summary in Dutch
Cover: Spin density plot of RuO_2 (110) surface
ISBN: 978-90-9028881-9
Printed by Ipskamp Drukkers BV, Enschede

The work presented in this thesis is part of the "Stichting voor Fundamenteel Onderzoek der Materie (FOM)" financially supported by the "Nederlandse Organisatie voor Wetenschappelijk Onderzoek (NWO)".

Contents

CHAPTER 1

Introduction

Materials that human beings have discovered or created have shaped our culture. Human civilization and materials have been evolving together, we even lend the names of materials to the ages; the stone age, the iron age, the bronze age and recently the silicon age. Many materials have influence on human history, some of them even have an impact on the destiny of nations.[1] Today, if we glimpse at the developments in materials science or solid state physics, we can foresee that human life in the future will also be influenced by new materials.

The exotic physical phenomena that solid state systems show have been stimulating scientists to develop theories for investigating and explaining them. A thorough understanding of the fundamental concepts behind these phenomena can even provide us with an opportunity to modify the materials according to our desires.

In solid state physics one of the important points of interest is the behavior of electrons in crystals, which cannot be explained properly by classical theories. Fortunately, at the beginning of the 20th century a revolutionary change occurred in understanding nature with the development of quantum mechanics. Quantum mechanics is a theory which has a much richer scope and applicability than classical theories.[2] Several physical phenomena which cannot be explained by classical theories such as wave-particle duality or blackbody radiation could be explained with the help of quantum mechanics.

The applicability of quantum mechanics to many-body systems in practice is rather limited. This is the main drawback of this theory for investigating the real materials. So, to explain many-body systems scientists needed to have more specialized theories based on the laws of quantum mechanics. Among these theories density functional theory (DFT) is one of the most successful methods to analyze the physical properties of solid state systems. DFT can provide accurate information about the bonding characteristics and electronic structure of most of the solid systems. In this thesis, we use DFT to examine the properties of several condensed matter systems. The aim is to understand the fundamental physics behind these properties by investigating the electronic structure of these materials.

In **Chapter 2**, we focus on the electronic structures of RuO_2 and OsO_2. These compounds have Dirac-like linear energy dispersion in their band structure around Fermi level like graphene which is a two dimensional monolayer carbon material. Graphene has become popular lately because it exhibits new physical phenomena and has several potential applications.[3,4] The unique linear band structure of graphene certainly plays an important role in these exotic properties. Graphene has a Dirac point in its band structure at the Fermi level. At this special point the valence and the conduction bands cross each other and show linear energy dispersion. That is why the electrons in graphene imitate relativistic particles and they are called Dirac Fermions which have zero mass. So, the electrons in graphene are described by the Dirac equation instead of the Schrödinger equation. This unique phenomenon undoubtedly has consequences for the transport properties of graphene.[5,6]

RuO_2 and OsO_2 have abnormal thermal expansion, the a and b lattice parameters expand whereas the c lattice parameter stays constant for OsO_2 and shrinks for RuO_2 with increasing temperature.[7–9] This means that the c/a ratio of the compounds changes drastically with temperature. Our DFT calculations show that the starting point of the linear dispersion relative to the Fermi level depends on the c/a ratio of the compounds.

Having linear bands at the Fermi energy has an effect on the physical properties of the materials. Since the bands can maintain perfect linearity only in a small range, it is important that their starting point coincides with the Fermi level.

RuO_2 is known as one of the best metals at low temperatures in terms of electrical conductivity. In **Chapter 2**, we also discuss the possible relation between the Dirac-like linear energy spectrum of RuO_2 and its low temperature high electrical conductivity.

1.1 The oxygen molecule and the electrolysis of water

In **Chapter 3** and **Chapter 4**, we investigate why RuO_2 is one of the best anodes for electrolysis of water in terms of the overvoltage. In this section we will provide brief background information on the properties of the oxygen molecule and the electrolysis of water.

The oxygen molecule is a remarkable molecule. It is indispensable for the aerobic life on Earth, it would end in ten minutes without oxygen. In addition to its importance, it also has a very interesting physical property: it is magnetic. The ground state of the oxygen molecule has two unpaired electrons which occupy the twofold degenerate anti-bonding π^* orbital (the molecular orbital diagram is shown in Figure 1.1), so the oxygen molecule has a 2 μ_B magnetic moment in its ground state.[10] The energy difference between the magnetic ground state and the (non-magnetic) first excited state of the oxygen molecule is around 1 eV.[11]

Chemical reactions are controlled by selection rules, and angular momentum conservation (spin selection rule) is one of the key selection rules in chemical reactions.[12] The angular momentum conservation can be the rate limiting factor for chemical reactions in which only one of the reactants or products is magnetic. That is why it is essential for chemical reactions in which the oxygen molecule is involved, such as electrolysis of water. In the literature, the spin selection rule was used to explain several phenomena which include oxygen molecule-surface interactions. For example, the low sticking parameter of the oxygen molecule on the Al(111) surface and the narrow barrierless oxidation channel of the Si(001) surface are explained by the spin selection rule.[13–16]

Electrolysis of water is important for the production of hydrogen; however its efficiency is relatively low because of the high overvoltage. Under ideal conditions, 1.23 volts is enough to separate the water molecule to oxygen and hydrogen. However, a larger voltage is necessary to drive this reaction in reality. The excess voltage which is needed to initiate this reaction is called overvoltage or overpotential.

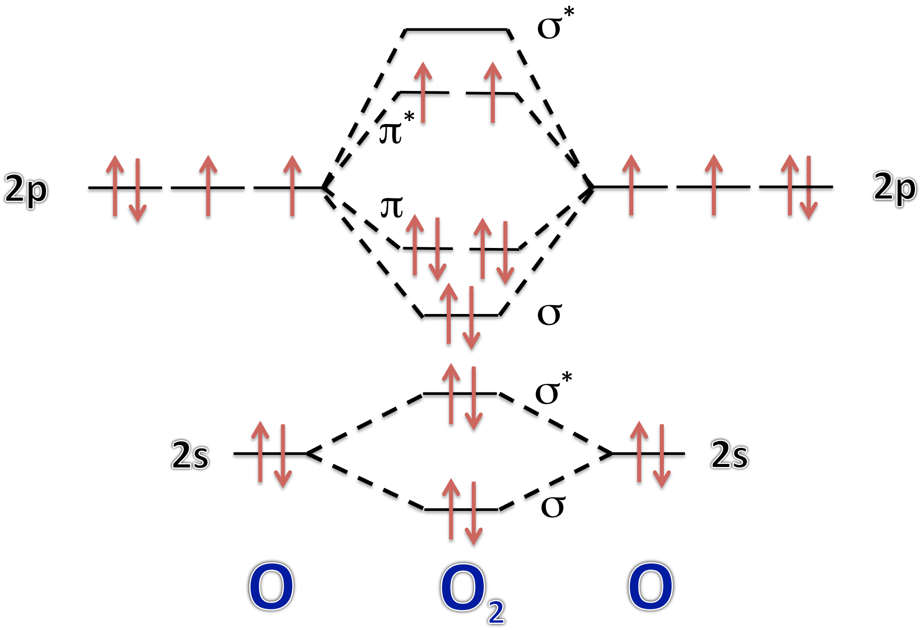

Figure 1.1: Molecular orbital diagram of triplet oxygen molecule

In electrolysis of water, neither water nor hydrogen is magnetic so the oxygen molecule is the only magnetic entity. That is why angular momentum seems not to be conserved in this reaction. This can have a significant contribution to the overpotential. In order to produce an oxygen molecule in its ground state while respecting angular momentum conservation, a second magnetic entity is needed. For example a magnetic anode may provide a mechanism to produce magnetic oxygen molecules while conserving angular momentum.

One of the best anodes for electrolysis is based on the RuO_2 (110) surface because of its low overvoltage.[17,18] First-principle calculations on clean and oxygen covered RuO_2 (110) surfaces, which are presented in **Chapter 3**, reveal that both surfaces carry magnetization which fits our earlier prediction.

The electrolysis of water has two half reactions; the hydrogen evolution reaction (HEO) which is happening at the cathode and the oxygen evolution reaction (OER) which is happening at the anode. Only the OER contributes to the overpotential significantly.[19]

The mechanism for the OER on the RuO_2 (110) surface, which is suggested in reference 17, starts with splitting of a water molecule[17]

$$S + H_2O \rightarrow S - OH + H^+ + e^-, \tag{1.1}$$

where S is the active surface site. Then OH loses its proton

$$S - OH \rightarrow S - O + H^+ + e^-. \tag{1.2}$$

Then two OH molecules on the surface combine

$$S - OH + S - OH \rightarrow S - O + S + H_2O, \tag{1.3}$$

finally O_2 is produced by a surface oxygen coupling step

$$S - O + S - O \rightarrow O_2 + 2S. \tag{1.4}$$

A further investigation of this mechanism is the subject of **Chapter 4**. Experimental studies show that doping a second metal into the RuO_2 (110) surface changes the oxygen evolution activity (OEA) of the anode. In **Chapter 4** we show correlations between the experimental OEA of doped RuO_2(110)-surface-based anodes and the modification of the surface magnetism due to the dopants by using first-principle calculations.

1.2 Magnetism in condensed matter

Magnetism is one of the main concepts that we study in this thesis. So, we will provide a brief description on magnetism in condensed matter systems and its relation with the electronic structure of materials in this section. Most of the derivations which are presented in this section are taken from references 20 and 21.

Magnetism has been subject of interest for around 3000 years; lodestone is the first magnetic material which attracted attention among Greek scientists. The magnetic compass, which was invented as a result of these studies, is one of the earliest technological products which uses the magnetic field of Earth for navigational purposes.[20] Despite its old history, magnetism in condensed matter is still an important subject. In this thesis most of the materials that we study are metallic. So in this section, magnetism in metallic systems and its relation with the electronic structure of materials will be discussed.

Magnetism in metals can be associated with delocalized electrons which are recognized as *itinerant* or else it can be due to localized magnetic moments. Band ferromagnetism, which is also known as itinerant ferromagnetism should be taken into consideration when the magnetic moment per atom in the system is non-integer. This situation cannot be explained by localized moments on atoms and it is due to spontaneous spin-split bands.

In molecular field theory there is an average exchange field λM which is produced by the neighbor atoms. M is the magnetization and λ is a parameter which measures the strength of the magnetization. All the spins in this system experience this average field. The molecular field can magnetize the system due to Pauli paramagnetism and the resulting magnetism is in fact responsible for the molecular field. If λ is large enough, this chicken-and-egg scenario can lead to spontaneous magnetism in condensed matter systems. The essential point is whether the system gains energy or not by becoming magnetic.

In Figure 1.2 the density of states (DOS) demonstrating the spontaneous energy band splitting without an applied magnetic field is shown. The left side of the figure shows the DOS for spin up and the right side shows the DOS for spin down electrons. The figure shows that some of the spin down electrons, which have energies up to $E_f - \delta E$ around Fermi surface, transferred to spin up bands. The total number of electrons which are transferred is $g(E_f)\delta E/2$. They increase in energy by δE so the kinetic energy change is

$$\Delta E_{KE} = \frac{1}{2} g(E_f)(\delta E)^2. \tag{1.5}$$

According to Equation 1.5 this process costs energy to the system so it may not be favorable. However, the interaction between the molecular field and the magnetization that appears after the transfer may compensate this cost. The number density of the spin up and the spin down electrons is given as $n_\uparrow = \frac{1}{2}(n + g(E_f)\delta E)$ and $n_\downarrow = \frac{1}{2}(n - g(E_f)\delta E)$, respectively. So, the magnetization is $M = \mu_\mathrm{B}(n_\uparrow - n_\downarrow)$. The energy

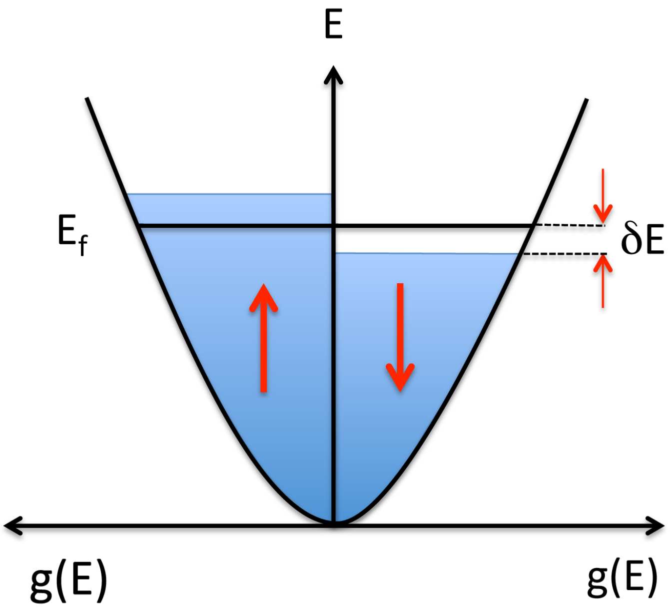

Figure 1.2: Density of states without an applied magnetic field.

of the molecular field (ΔE_{MF}) can be obtained by solving the following integral

$$\begin{aligned}\Delta E_{MF} &= -\int_0^M \mu_0(\lambda M')dM' = -\frac{1}{2}\mu_0\lambda M^2 \\ &= -\frac{1}{2}\mu_0\mu_B^2\lambda(n_\uparrow - n_\downarrow)^2.\end{aligned} \tag{1.6}$$

The total energy change is

$$\begin{aligned}\Delta E &= \Delta E_{KE} + \Delta E_{MF} \\ &= \frac{1}{2}g(E_f)\,(\delta E)^2\,(1 - \mu_0\mu_B^2\lambda g(E_f)).\end{aligned} \tag{1.7}$$

The spontaneous ferromagnetism will occur when $\Delta E < 0$ which leads to;

$$\mu_0\mu_B^2\lambda g(E_f) \geq 1. \tag{1.8}$$

Equation 1.8 is known as the **Stoner criterion** of magnetism. Magnetism appears when the Coulomb effects in the system are strong and also the DOS at the Fermi level is large. If the requirements are fulfilled then the spin up and the spin down electrons are split by an energy Δ which is the exchange energy when there is no external magnetic field.

In **Chapter 5**, we investigate an unsolved problem: the origin of weak magnetism in materials like $TiBe_2$ and $ZrZn_2$ which crystallize in the C15 structure. Actually, none of the elements which form $TiBe_2$ and $ZrZn_2$ are magnetic as solid. The position of titanium and zirconium is at the left side of the transition metal series and the other constituting atoms are main group elements.

Since the chemical composition is not the reason of the magnetism in these materials, the special symmetry of the C15 structure should be the reason. Electronic structure calculations show a high peak at the Fermi level of both $TiBe_2$ and $ZrZn_2$. Our analytical investigation shows that there is no crystal field splitting (CFS) for the *d* orbitals in these compounds. This is the reason of a high DOS at the Fermi level and consequently the magnetism in these materials *via* the Stoner criterion of magnetism.

As an extension of this work we perform a similar analysis for the *f*-electron compounds, which crystallize in the C15 structure. Unlike the case of *d* levels, CFS for *f* orbitals can be explained with two parameters. The ratio of these two parameters and the local point symmetry of the compounds determine the characteristics of CFS in these materials.

1.3 Crystal Field Theory Formalism

Since the crystal field theory (CFT) is used in **Chapter 5** we will give a brief introduction of it in this section. Most of the derivations in this section are performed with the help of references 22 and 23.

The total Coulomb potential at a point in space can be calculated by taking into account the contributions from all of the individual charges surrounding it. This can be stated as

$$V(x,y,z)=\sum_{i=1}^{n}\frac{ez_i}{r_{ij}}. \tag{1.9}$$

In Equation 1.9, r_{ij} is the distance between the charge and the point of interest where the total potential is aimed to be calculated. In a crystal the ligands cause the Coulomb potential which affects the splitting of the *d* and *f* levels of the central atom. The effect of this crystal field potential (CFP) on the *d* and *f* orbitals should be investigated by perturbation theory. The energy of the *n*-fold degenerate orbitals can be found by solving the following Schrödinger equation

$$H_0\psi_i(r,\theta,\phi)=E_0\psi_i(r,\theta,\phi). \tag{1.10}$$

Where $i\rightarrow 1,\ldots,n$, and for the *d* orbitals "*n*" should be taken as 5 and for the *f* orbitals it should be taken as 7.

The CFP can be treated as a perturbation to the old Hamiltonian (H_0). So, ψ_i is no longer the eigenfunction of $H^{'}=(H_0+V)$ nor is E_0 its eigenvalue. The Schrödinger equation of the perturbed system can be written as

$$(H_0+V)\psi_j^{'}(r,\theta,\phi)=E_j^{'}\psi_j^{'}(r,\theta,\phi). \tag{1.11}$$

The eigenvalues of (H_0+V) are $E_j^{'}(j \rightarrow 1, 2, ...n)$ and the corresponding eigenfunctions are $\psi_j^{'}$. The eigenfunctions of new perturbed Hamiltonian $(\psi_j^{'})$ can be written as linear combination of the old eigenfunctions (ψ_i) of the unperturbed Hamiltonian

$$\begin{aligned} \psi_j^{'} &= c_{1j}\psi_1 + c_{2j}\psi_2 + \dots c_{nj}\psi_n, \\ &= \sum_{i=1}^{n} c_{ij}\psi_i, \end{aligned} \tag{1.12}$$

with normalization

$$\sum_{i=1}^{n} c_{ij}^{*}c_{ij} = 1. \tag{1.13}$$

The spatial variation of the orbitals can be separated into 2 parts: the radial and the angular part

$$\psi_{nlm_l}(r,\theta,\phi) = R_{nl}(r)Y_l^{m_l}(\theta,\phi), \tag{1.14}$$

where n is the principal quantum number describing the electron shell and l (from 0 to n-1) is the azimuthal quantum number providing the subshell information. It gives the magnitude of the angular momentum through the relation

$$L^2Y_l^{m_l}(\theta,\phi) = \hbar^2 l(l+1)Y_l^{m_l}(\theta,\phi). \tag{1.15}$$

m_l is the specific orbital within the subshells (from $-l$ to l). So, for the d orbitals l is 2 and m_l is -2,-1,0,1,2 and for the f orbitals l is 3 and m_l is -3,-2,-1,0,1,2,3.

In order to find the eigenvalues and the eigenfunctions of a perturbed system, the secular matrix should be diagonalized:

$$\begin{array}{c|cccc|c} & \psi_1 & \psi_2 & & \psi_n & \\ \psi_1 & H_{1,1}^{'} - E^{'} & H_{1,2}^{'} & \cdots & H_{1,n}^{'} & \\ \psi_2 & H_{2,1}^{'} & H_{2,2}^{'} - E^{'} & \cdots & H_{2,n}^{'} & = 0 \\ \vdots & \vdots & \vdots & \ddots & \vdots & \\ \psi_n & H_{n,1}^{'} & H_{n,2}^{'} & \cdots & H_{n,n}^{'} - E^{'} & \end{array} \tag{1.16}$$

where

$$H_{i,j}^{'} = \int \psi_i^{*}(r,\theta,\phi)H^{'}\psi_j(r,\theta,\phi)\ d\tau. \tag{1.17}$$

In order to find the splitting of the d orbitals the secular determinant of a 5×5 matrix should be constructed. It has the following form

$$\begin{array}{c|ccccc|}
 & (2) & (1) & (0) & (-1) & (-2) \\
(2) & H_{2,2}-E & H_{2,1} & H_{2,0} & H_{2,-1} & H_{2,-2} \\
(1) & H_{1,2} & H_{1,1}-E & H_{1,0} & H_{1,-1} & H_{1,-2} \\
(0) & H_{0,2} & H_{0,1} & H_{0,0}-E & H_{0,-1} & H_{0,-2} \\
(-1) & H_{-1,2} & H_{-1,1} & H_{-1,0} & H_{-1,-1}-E & H_{-1,-2} \\
(-2) & H_{-2,-2} & H_{-2,1} & H_{-2,0} & H_{-2,-1} & H_{-2,-2}-E
\end{array} = 0 \quad (1.18)$$

The matrix elements are

$$H_{m_l,m_l'} = e\int (m_l)^* V_{(x,y,z)} (m_l)' d\tau, \tag{1.19}$$

where the m_l represent the spherical harmonics, $Y_l^{m_l}$.

The next procedure is to write $V(x,y,z)$ (Equation 1.9) in terms of spherical harmonics using

$$\frac{1}{r_{ij}} = \sum_{n=0}^{\infty}\sum_{m=-n}^{n} \frac{4\pi}{2n+1}\frac{r_<^n}{r_>^{n+1}} Y_{nj}^{m}(\theta,\phi) Y_{ni}^{m^*}(\theta,\phi). \tag{1.20}$$

In Equation 1.20, the second spherical harmonic corresponds to the ligand atoms and the first one to the d or f orbitals of the central atom. With the help of this definition, the matrix elements and consequently the splitting of the d and f levels due to the ligands can be obtained. This is basically the procedure that we follow in **Chapter 5**.

1.4 Density functional theory formalism

In this section, we will give a brief description of DFT formalism since we use it as a method in this thesis. In quantum mechanics all of the information about a system is contained in its wave function, ψ. The wave function of the system can be obtained by solving the Schrödinger equation. The difficulty in solving the Schrödinger equation depends on the complexity of the given potential for single-body systems, or the number of interacting particles present in the many-body systems. The latter is the case for the materials that we deal with in this thesis.

The Schrödinger equation for a single electron in a potential is

$$\begin{aligned}
\widehat{H}\psi(\mathbf{r}) &= E\psi(\mathbf{r}), \\
\left(\widehat{T}+\widehat{V}\right)\psi(\mathbf{r}) &= E\psi(\mathbf{r}), \\
\left[-\frac{1}{2}\nabla^2 + v(\mathbf{r})\right]\psi(\mathbf{r}) &= E\psi(\mathbf{r}).
\end{aligned} \tag{1.21}$$

where the operators $\widehat{H}$, $\widehat{T}$, and $\widehat{V}$ represent the Hamiltonian, kinetic energy, and potential energy of the given system, respectively. Most of the condensed matter systems contain many interacting particles. In order to investigate these systems the many-body Schrödinger equation should be solved, instead of single-body Schrödinger equation (Equation 1.21). The many-body Schrödinger equation is

$$\begin{gathered}\left(\widehat{T}+\widehat{V}+\widehat{U}\right)\psi\left(\mathbf{r_1},\mathbf{r_2}...,\mathbf{r_N}\right)=E\psi\left(\mathbf{r_1},\mathbf{r_2}...,\mathbf{r_N}\right), \\ \left[-\sum_i\frac{1}{2}\nabla_i^2+\sum_{ik}\frac{Q_kq}{|\mathbf{r}_i-\mathbf{R}_k|}+\sum_{i<j}\frac{q^2}{|\mathbf{r}_i-\mathbf{r}_j|}\right]\psi\left(\mathbf{r_1},\mathbf{r_2}...,\mathbf{r_N}\right)=E\psi\left(\mathbf{r_1},\mathbf{r_2}...,\mathbf{r_N}\right).\end{gathered} \tag{1.22}$$

The first term in Equation 1.22 is the kinetic energy operator. The second term represents the potential produced by the nuclei in the system and the third term is the electron-electron Coulomb interaction energy operator.[24] The position of the i^{th} electron is r_i and R_k is the position of the k^{th} nucleus. In this equation, the wave function $\psi(\mathbf{r_1},\mathbf{r_2}...,\mathbf{r_N})$ of the system depends only on electronic coordinates for given R_k. The nuclear degrees of freedom are present only in the potential because the Born-Oppenheimer approximation is used to write this equation. The core of the Born-Oppenheimer approximation is that the electrons are much lighter and are moving more rapidly than the nuclei in solid. The electrons adapt themselves accurately to the much slower nuclear motion.[25]

Solving the many-body Schrödinger equation is still not a simple task, even though the Born-Oppenheimer approximation simplifies it. There are basically two different methods to solve Equation 1.22: wave function methods and the methods based on the electron density such as DFT. Actually, DFT is more than just another way of solving a many-body Schrödinger equation. It is a robust method to approach any interacting problem by mapping it to a non-interacting problem which is easier to solve.[26]

The essential part of DFT are the Hohenberg-Kohn theorems. In general these theorems take the electron density, $n(\mathbf{r})$, as the basic variable and investigate its relation with the external potential produced by the nuclei in the system. In an interacting electron system which is under the influence of an external potential $v(\mathbf{r})$, $n(\mathbf{r})$ is a functional of $v(\mathbf{r})$ but the reverse is not trivial. The first Hohenberg-Kohn theorem proves that $v(\mathbf{r})$ is a unique functional of $n(\mathbf{r})$, indeed.[27] The proofs of these theorems are given below.

For the moment assume that there are two external potentials differing by more than a constant; $v_1(\mathbf{r})$ and $v_2(\mathbf{r})$ which have the same ground state density, $n_0(\mathbf{r})$. $v_1(\mathbf{r})$ and $v_2(\mathbf{r})$ belong to different Hamiltonians $\widehat{H}_1$ and $\widehat{H}_2$ which correspond to different ground state wave functions $\psi_1(\mathbf{r})$ and $\psi_2(\mathbf{r})$, respectively. The minimum energy of $\widehat{H}_1$ can be obtained only by $\psi_1(\mathbf{r})$, so the following inequality holds if the ground state is non-degenerate

$$E_1 = \langle \psi_1 | \widehat{H}_1 | \psi_1 \rangle < \langle \psi_2 | \widehat{H}_1 | \psi_2 \rangle. \tag{1.23}$$

Since these two potentials have the same ground state density, Equation 1.23 can be written as

$$\langle \psi_1 | \widehat{H}_1 | \psi_1 \rangle < \langle \psi_2 | \widehat{H}_2 | \psi_2 \rangle + \int d\mathbf{r} \left[\mathrm{v}_1 (\mathbf{r}) - \mathrm{v}_2 (\mathbf{r}) \right] \mathrm{n}_0 (\mathbf{r}) \, . \tag{1.24}$$

If the labels are exchanged then Equation 1.23 can be written as

$$\langle \psi_2 | \widehat{H}_2 | \psi_2 \rangle < \langle \psi_1 | \widehat{H}_1 | \psi_1 \rangle + \int d\mathbf{r} \left[\mathrm{v}_2 (\mathbf{r}) - \mathrm{v}_1 (\mathbf{r}) \right] \mathrm{n}_0 (\mathbf{r}) \, . \tag{1.25}$$

If Equation 1.24 and 1.25 are added the following inequality is obtained

$$E_1 + E_2 < E_2 + E_1. \tag{1.26}$$

The inconsistency in Equation 1.26 is apparent so the assumption that leads to this inconsistency should be wrong. This proves that $n(\mathbf{r})$ uniquely determines $v(\mathbf{r})$ within an arbitrary constant. The proof of the first Hohenberg-Kohn theorem is based on *reductio ad absurdum*.

Since $v(\mathbf{r})$ is uniquely determined by $n(\mathbf{r})$ and $n(\mathbf{r})$ in turn fixes $\widehat{H}$, the ground state energy of the system, $E[n]$, should be a unique functional of $n(\mathbf{r})$. The second Hohenberg-Kohn theorem states that there is a *universal* functional, $F[n]$, which is independent of $v(\mathbf{r})$ so identical for *any* interacting electron system that is influenced by *any* external potential for the total energy functional $E[n]$. The exact ground state energy of the system is the global minimum of $E[n]$. Since $F[n]$ is composed of the kinetic energy and the electron-electron interaction energy, the total energy functional can be defined as

$$E[n] = F[n] + \int v(\mathbf{r}) n(\mathbf{r}) d\mathbf{r}. \tag{1.27}$$

According to the variational principle a different density gives higher energy than the ground state energy E_0,

$$E[n'] = F[n'] + \int v(\mathbf{r}) n'(\mathbf{r}) d\mathbf{r} > E_0. \tag{1.28}$$

If F[n] is known for an interacting electron system, obtaining the ground state energy and the density for a given potential would be easy. Since the energy is a functional of the density which is a three dimensional function, the requirement is to minimize the energy functional only in three dimensions. The complication however, is to determine F[n] accurately for the interacting electron systems.

One of the earliest examples of the universal functional F[n] is based on the Thomas-Fermi approach.[28,29] In this approach F[n] is written as

$$F[n] = \frac{3}{10} \left(3\pi^2 \right)^{\frac{2}{3}} \int n^{5/3} d\mathbf{r} + \frac{1}{2} \iint \frac{n(\mathbf{r}) n(\mathbf{r}')}{|\mathbf{r} - \mathbf{r}'|} d\mathbf{r} d\mathbf{r}'. \tag{1.29}$$

The first term in Equation 1.29 assigns to each volume element $d\mathbf{r}$ the kinetic energy density of a uniform electron gas with density $n(\mathbf{r})$, i.e. it is a local density approximation to the kinetic energy of a non-uniform electron gas. The second term is the electron-electron Coulomb interaction term which is called the Hartree term. The practical usage of this universal functional is limited because of its deficiencies. For example, the Thomas-Fermi method fails to predict molecules because isolated atoms have lower energy than bound molecules.[30]

The most important step towards making DFT a powerful tool was put forward by Kohn and Sham.[31] Kohn and Sham suggested a universal functional of a non-interacting electron system which has the same ground state density as the original interacting electron system as follows

$$F[n] = T[n] + \frac{1}{2}\iint \frac{n(\mathbf{r})n(\mathbf{r}^{'})}{|\mathbf{r}-\mathbf{r}^{'}|} d\mathbf{r}d\mathbf{r}^{'} + E_{xc}[n]. \tag{1.30}$$

The first two terms in Equation 1.30 are in the non-interacting picture and the missing many-body effect is accounted for an exchange-correlation term, $E_{xc}[n]$. The charge density is written using the non-interacting orbitals $\phi_i(\mathbf{r})$ as

$$n(\mathbf{r}) = \sum_{n}^{N} |\phi_i(\mathbf{r})|^2. \tag{1.31}$$

In the non-interacting picture the kinetic energy is easily and accurately calculated as

$$T[n] = -\frac{1}{2}\sum_i \int \phi_i^*(\mathbf{r})\nabla^2\phi_i(\mathbf{r})\, d\mathbf{r}. \tag{1.32}$$

The famous Kohn-Sham equations are obtained by substituting the universal functional into the ground state total energy and minimizing it under the constraint of orthonormal orbitals $\phi_i(\mathbf{r})$. The Kohn-Sham equations are

$$\left[-\frac{1}{2}\nabla^2 + \int \frac{\mathrm{n}(\mathbf{r}^{'})}{|\mathbf{r}-\mathbf{r}^{'}|} d\mathbf{r}^{'} + v_{xc}(\mathbf{r}) + v(\mathbf{r})\right]\phi_i(\mathbf{r}) = \epsilon_i\phi_i(\mathbf{r}), \tag{1.33}$$

where

$$v_{xc}(\mathbf{r}) = \frac{\delta E_{xc}[\mathrm{n}]}{\delta n}. \tag{1.34}$$

The Kohn-Sham equations are a set of non-interacting single-particle equations so they are easier to solve than the many-body Schrödinger equation. However, the exchange and correlation part is unknown and should be approximated.

The first, widely used, approximation was the local density approximation (LDA), that approximates E_{xc} locally with the exchange-correlation energy density of a uniform electron gas. In the LDA, E_{xc} depends only on the local density $n(\mathbf{r})$. This can be extended to the local spin-density approximation, which considers two spin densities, one for the majority $n^{\uparrow}(\mathbf{r})$ and one for the minority $n^{\downarrow}(\mathbf{r})$ spin electrons. A great improvement in accuracy was reached with the so-called generalized gradient corrected functionals (GGA), that also consider the gradient of the density as[32]

$$E_{xc}^{GGA}[n^{\uparrow}, n^{\downarrow}] = \int n(\mathbf{r})\epsilon_{xc}(n^{\uparrow}, n^{\downarrow}, |\nabla n^{\uparrow}|, |\nabla n^{\downarrow}|)d\mathbf{r} \tag{1.35}$$

The way to construct these functionals is not unique. Many “flavours” are available in the literature. In this thesis we use the widely-used functional by Perdew, Burke and Ernzerhof (PBE).[33]

The Kohn-Sham equation should be solved self-consistently: by the use of an initial guessed $n(\mathbf{r})$, all the terms in Equation 1.33 should be obtained. By solving Equation 1.33 the new $n(\mathbf{r})$ can be evaluated. If the new $n(\mathbf{r})$ and the initial $n(\mathbf{r})$ are the same, then the self-consistency is reached, else the $n(\mathbf{r})$ should be changed until the new and the initial $n(\mathbf{r})$ are the same.

1.5 Outline of this thesis

In this section, we summarize the structure of this thesis.

In **Chapter 2**, we focus on the Dirac-like dispersion at the Z point in the band structure of rutile RuO_2 and OsO_2. We show that the starting point of two linear bands relative to the Fermi level is very sensitive to the c/a ratio of the systems. We also show that there is a special c/a ratio for which the starting point of the linear dispersion and the Fermi level coincide. This could be important for the electrical conductivity of these materials.

In **Chapter 3**, we show, by using first-principle calculations, that the clean and oxygen covered RuO_2 (110) surfaces carry local magnetic moments. We discuss the importance of the surface magnetism for the oxygen evolution part of the electrolysis of water reaction.

In **Chapter 4**, as a further analysis of **Chapter 3**, we perform first-principle calculations on transition metal doped RuO_2 (110) surfaces. A correlation is shown between the experimental OEA of doped RuO_2(110)-surface-based anodes and the modification of the surface magnetism because of dopants. A general discussion on the effect of the surface magnetism on the interaction between an oxygen molecule and surfaces is carried out, too.

In **Chapter 5**, the origin of the weak itinerant magnetism of $TiBe_2$ and $ZrZn_2$ is investigated. We show that the high peak in the density of states, which is responsible for magnetism in these materials, is due to having vanishingly small CFS for the d levels. In this chapter we also investigate CFS in f-electron compounds which crystallize in the C15 structure. We observe that the situation for f levels is different and more complicated than for d levels. The reason is that the characteristics of the CFS for the f levels can be explained with two parameters unlike the case for the d levels. The local point symmetry and the ratio of these two parameters determine the CFS in f-electron compounds. Our DFT calculations on these materials show that the CFS changes from one compound to another which fits our analytical analysis.

Bibliography

1. S. L. Sass. The Substance of Civilization, Arcade Publishing (2011).
2. J. J. Sakurai. Modern Quantum Mechanics, Addison-Wesley Publishing Company (1994).
3. K. S. Novoselov, A. K. Geim, S. V. Morozov, D. Jiang, Y. Zhang, S. V. Dubonos, I. V. Grigorieva, and A. A. Firsov, Science **306**, 666 (2004).
4. A. K. Geim and K. S. Novoselov, Nature Materials **6**, 183 (2007).
5. K. S. Novoselov, A. K. Geim, S. V. Morozov, D. Jiang, M. I. Katsnelson, I. V. Grigorieva, S. V. Dubonos, and A. A. Firsov, Nature **438**, 197 (2005).
6. A. H. Castro Neto, F. Guinea, N. M. R. Peres, K. S. Novoselov, and A. K. Geim, Rev. Mod. Phys. **81**, 109 (2009).
7. Y. C. Venudhar, L. Iyengar, and K. V. K. Rao, Crystal Research and Technology **20**, 1393 (1985).
8. K.-I. Murai, Y. Akune, Y. Suzuki, T. Moriga, and I. Nakabayashi, International Journal of Modern Physics B **20**, 4111 (2006).
9. K. V. K. Rao and L. Iyengar, Acta Crystallographica Section A-Crystal Physics Diffration Theoretical and General **25**, 302 (1969).
10. C. Schweitzer and R. Schmidt, Chemical Reviews **103**, 1685 (2003).
11. L. Bytautas, N. Matsunaga, and K. Ruedenberg, The Journal of Chemical Physics **132**, 074307 (2010).
12. E. Wigner, Nachr. Ges. Wiss. Goett. Math-Phys, 1927.
13. K. Kato, T. Uda, and K. Terakura, Phys. Rev. Lett. **80**, 2000 (1998).
14. J. Behler, B. Delley, S. Lorenz, K. Reuter, and M. Scheffler, Phys. Rev. Lett. **94**, 036104 (2005).
15. J. Behler, K. Reuter, and M. Scheffler, Phys. Rev. Lett. **96**, 079802 (2006).
16. C. Carbogno, J. Behler, A. Gross, and K. Reuter, Phys. Rev. Lett. **101**, 096104

(2008).

17. G. Lodi, E. Sivieri, A. Debattisti, and S. Trasatti, Journal of Applied Electrochemistry **8**, 135 (1978).
18. C.-C. Chang and T.-C. Wen, Journal of Applied Electrochemistry **27**, 355 (1997).
19. M. H. Miles, E. A. Klaus, B. P. Gunn, J. R. Locker, W. E. Serafin and S. Srinivasan, Electrochimica Acta **23**, 521 (1978).
20. S. Blundell, Magnetism in Condensed Matter, Oxford University Press (2001).
21. J. Kübler, Theory of Itinerant Electron Magnetism, Oxford Science Publications (2000).
22. B. N. Figgis, Introduction to Ligand Fields, Interscience (1966).
23. C. J. Ballhausen, Introduction to Ligand Field Theory, McGraw-Hill Book Company (1962).
24. K. Capelle, arXiv:cond-mat, 0211443v5, 2006.
25. M. Born and J. R. Oppenheimer, Ann. Phys. **84**, (1927).
26. K. Burke, The ABC of DFT, (2007).
27. P. Hohenberg and W. Kohn, Phys. Rev. **136**, B864 (1964).
28. E. Fermi, Zeitschrift für Physik **48**, 73 (1928).
29. L. H. Thomas, Proc. Cambridge Phil. Soc **23**, 542 (1927).
30. E, Teller, Rev. Mod. Phys. **34**, 627 (1962).
31. W. Kohn and L. J. Sham, Phys. Rev. **140**, A1133 (1965).
32. R. M. Martin, Electronic Structure Basic Theory and Practical Methods, Cambridge University Press, (2005).
33. J. P. Perdew, K. Burke, and M. Ernzerhof, Phys. Rev. Lett. **77**, 3865 (1996).

CHAPTER 2

Dirac-like Dispersion in the Band Structure of Ruthenium Dioxide

Abstract

Presence of a Dirac point at the Fermi level leads to interesting physical properties. In spite of the fact that the band structure of RuO_2 has been known for decades, the Dirac-like linear energy dispersion along the Z-Γ direction as well as its possible relation with the low temperature high electron mobility of RuO_2 has been overlooked. In this chapter, we perform first-principle calculations including spin-orbit coupling (SOC) for various c/a ratios with fixed volume and analyze the band structures and the Fermi surfaces of RuO_2 and OsO_2. We observe that for a specific c/a ratio the degenerate states at the Z point, which is the starting point of the linear dispersion in the Brillouin zone (BZ), coincide with the Fermi level.

A manuscript based on this chapter has been submitted for publication by E. Torun, C. M. Fang and R. A. de Groot.

2.1 Introduction

Ruthenium dioxide in its rutile form has been subject of interest for several decades due to its potential important applications such as electrical contact material[1,2], super-capacitor[3], cathode material in high power Li-ion batteries[4,5], in spintronics as nanowires[6] and because of its low overpotential in electrolysis: it is one of the best electrocatalysts for oxygen evolution.[7,8] Another very important property which makes RuO_2 a widely used material is its unusual high electrical conductivity at low temperature.[9–14]

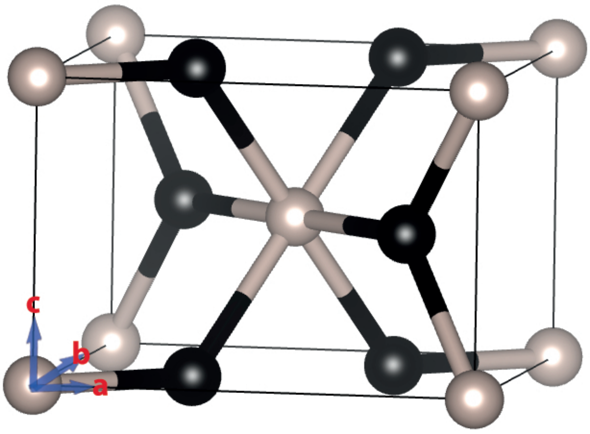

Figure 2.1: The crystal structure of rutile RuO_2 and OsO_2. The grey atoms are metal and the black ones are oxygen atoms.

Graphene, which recently has become a very popular 2D material, has a unique band structure: It has a Dirac point at the Fermi level. At this special point the conduction and the valence bands cross each other and show a linear energy dispersion. Because of this linear energy dispersion the charge carriers of graphene behave like massless Dirac fermions.[15–20] Several exotic physical phenomena can be investigated with the help of this special band structure. In graphene, the Dirac point is the *only* intersection of the conduction band with the Fermi energy. This special band structure certainly has effect on the electron transport of graphene, which is known to be a very good conductor.

Dirac points are not rare in general: they are an intrinsic property of space groups, more often of non-symmorphic ones. Having a Dirac point at the Fermi level is quite special, however. This very important property is not limited to 2D crystals, it has been reported that in 3D crystals Dirac points and semi-Dirac points occur as well.[21–27]

Like in graphene, Dirac-like linear dispersion is present in the band structure of RuO_2. In spite of the fact that the electronic structure of rutile RuO_2 has attracted

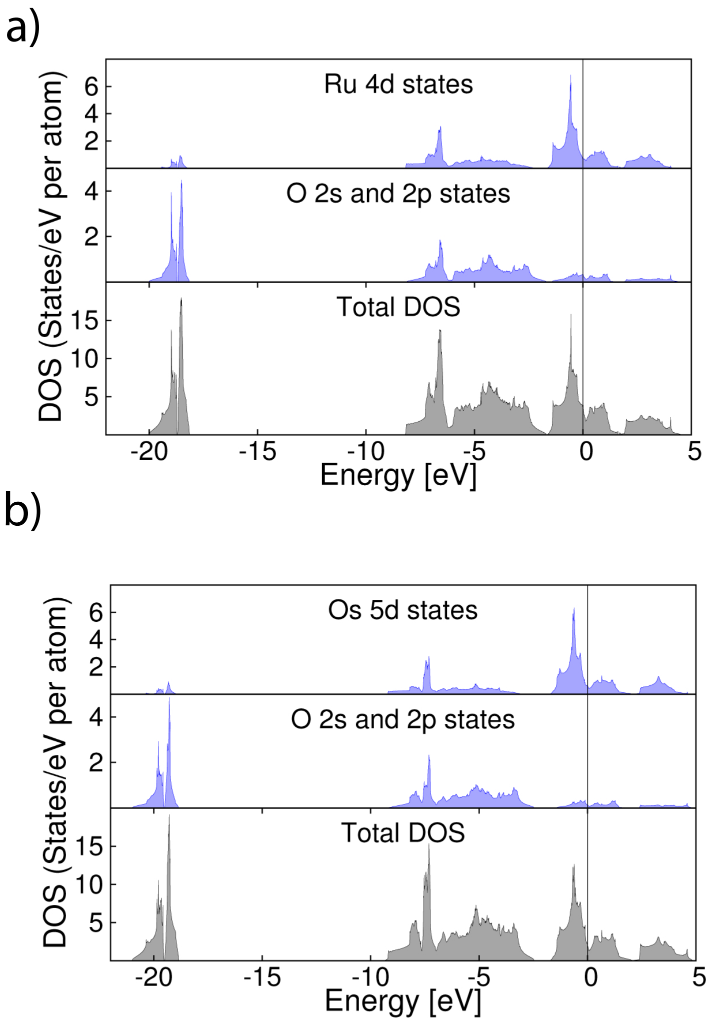

Figure 2.2: The partial and the total DOS of a) RuO_2 and b) OsO_2 rutile

theoreticians for a long time, this observation never received attention.[28–37] Traditionally the subjects of interest in solids are often associated with a high density of states (DOS) at the Fermi energy. Such phenomena usually do not depend much on (small) variations of the compound. The contrary is the case here. The starting point of the linear dispersion is easily shifted relative to the Fermi energy by small deformations[a]. That could be the reason why the transport properties of RuO_2 are very sensitive to the small variations in chemical composition.

In this chapter, we report first-principle calculations on bulk rutile RuO_2 including SOC. We show that change in c/a ratio does not have much effect on the general appearance of the Fermi surface but does have an effect on the starting point of the

---

[a] In graphene the Dirac points are the only contribution to the Fermi surface. Hence, in graphene, the Fermi level should remain at the Dirac points when the lattice slightly deformed.

Dirac-like dispersion relative to the Fermi level. For comparison, we also report the electronic structure of OsO_2 because it is iso-structural and iso-electronic with RuO_2.

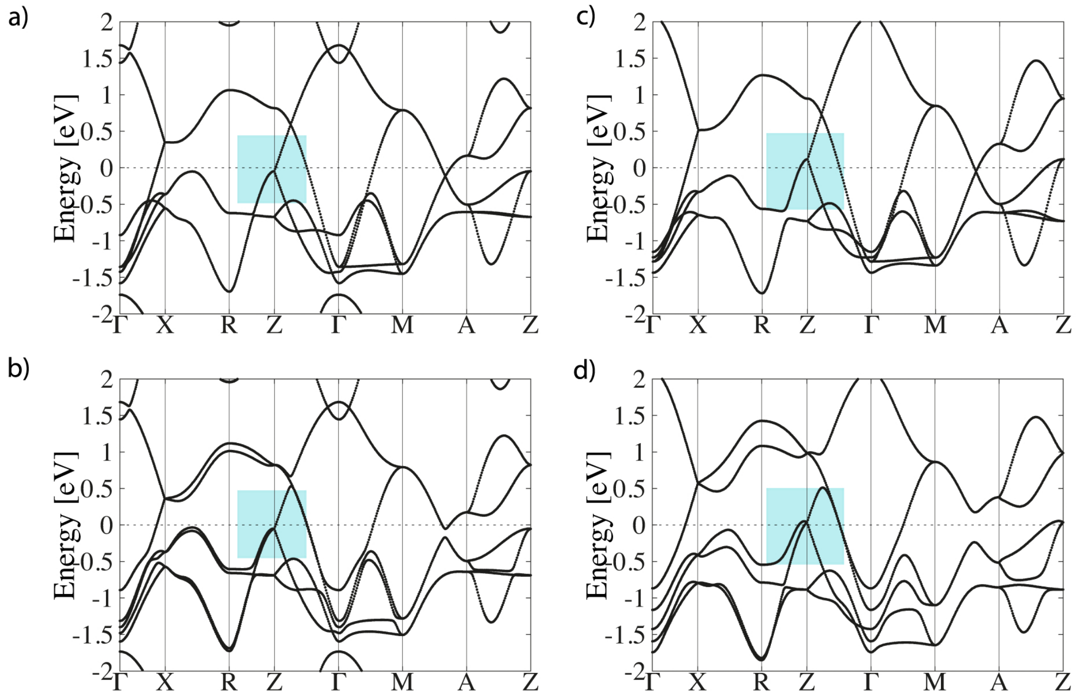

Figure 2.3: Band structures of optimized bulk RuO_2 (without (a) and with (b) SOC) and OsO_2 (without (c) and with (d) SOC). The bands which have linear dispersion along Z-Γ direction are highlighted in color for all cases.

2.2 Results and Discussions

All calculations were carried out in the framework of density functional theory (DFT)[38,39] using the first-principles code "Vienna ab initio simulation program" (VASP)[40,41] and the projector augmented wave method (PAW).[42,43] The generalized gradient approximation (GGA) by Perdew, Burke and Ernzerhof (PBE)[44] was employed for the exchange and correlation energy terms. The electronic wave functions were sampled on an $8 \times 8 \times 12$ k-mesh using the Monkhorst-Pack method.[45] The structures are relaxed until the forces on the atoms are smaller than the 0.0001 eV/Å.

RuO_2 and OsO_2 have the rutile structure (Figure 2.1) with space group $P4/mnm$ (# 136).[10,46] The ruthenium and osmium atoms occupy the $2a(0,0,0)$ and the oxygen atoms are at the $4f(u,u,0)$ Wyckoff positions. The lattice parameters a and c, as well as the internal coordinate parameter of oxygen (u) determine the crystal structure. The optimized lattice parameters of $a = 4.52$ Å and $c = 3.12$ Å for RuO_2 and

$a = 4.52$ Å and $c = 3.22$ Å for OsO_2 are used. The experimental data for RuO_2 and OsO_2 from the literature are included for comparison in Table 2.1 and Table 2.2, respectively.

Table 2.1: The optimized and previously reported lattice and internal parameters of RuO_2. TW stands for "this work" and V is the volume of the unit cell.

RuO_2	GGA(TW)	GGA	LDA	Experiment
a(Å)	4.52	4.5246[37], 4.5059[37]	4.56[30],4.47[35]	4.51[46]
			4.474[34],4.4336[37]	4.4906[10]
c(Å)	3.12	3.1355, 3.1059	3.16 ,3.08	3.11
			3.092 ,3.091	3.1064
c/a	0.69027	0.6930, 0.6893	0.6930 ,0.6890	0.6896
			0.6911 ,0.6972	0.6918
u(O)	0.30573	0.3067, 0.3058	0.3068 , —	—
			0.3058 ,0.3072	—
V(Å^3/fu)	32.42	32.10, 31.53	32.85 ,30.77	31.63
			30.95 ,30.38	31.32

Since RuO_2 and OsO_2 are iso-structural and iso-electronic, their electronic structures exhibit similarities. The calculated electronic structures for both materials basically agree with the former theoretical work for RuO_2[28–37] and OsO_2.[28,47] That is why we will discuss and compare the electronic structure of these two materials only briefly here.

Figure 2.2 shows the total and the partial DOS of RuO_2 and OsO_2, respectively. The valence bands of RuO_2 and OsO_2 can be recognized as two well-separated parts. For RuO_2 the oxygen 2s states form a band with a width of 2 eV (from -20 eV to -18 eV), which is slightly narrower than for the OsO_2, its 2s states form a band with a width of 2.5 eV. The upper part of the valence bands starts at approximately -9.5 eV for OsO_2 and -8 eV for RuO_2, with the lower part dominated by oxygen 2p states. There is a pseudo-gap between oxygen 2p states and the ruthenium 4d and osmium 5d states which dominate the bands around the Fermi level (at 0 eV). The e_g-t_{2g} splitting can be easily recognized in both compounds. The e_g bands are above the Fermi level and form a broad band with a width of 3 eV (from around 2 eV to 5 eV). The Fermi level is in the middle of t_{2g} bands. The sharp peak around -0.5 eV matches

Table 2.2: The optimized and previously reported lattice and internal parameters of OsO_2. TW stands for "this work" and V is the volume of the unit cell.

OsO_2	GGA(TW)	Experiment
a(Å)	4.52	4.51[46],4.4968[10]
c(Å)	3.22	3.19 ,3.182
c/a	0.71239	0.7073 ,0.7076
$u(O)$	0.30845	—
V(Å^3/fu)	32.895	32.44 ,32.18

the sharp peak measured spectroscopically.[48,49] A similar peak exists for OsO_2 as well.

Figure 2.3 shows the band structures of rutile RuO_2, without (Figure 2.3a) and with (Figure 2.3b) SOC, respectively. The Dirac-like energy dispersion along the Z-Γ direction in the BZ can be seen clearly in both band structures. In Figure 2.3a, the doubly degenerate states along R-Z, split into two linearly dispersing bands at Z and continue linearly along Z-Γ till almost one third of this direction. An important conclusion is that the linear dispersion and degeneracy of these states are *unaffected* by the inclusion of the SOC (Figure 2.3b). The double degeneracy of these states along R-Z is lifted slightly however, they merge at Z and split into bands with linear dispersion along Z-Γ. For the optimized RuO_2, the doubly degenerate states are 0.05 eV lower in energy with respect to the Fermi level. The effect of the SOC appears mostly along the X-R and R-Z directions. The doubly degenerate states at -0.62 and 1.06 eV at R, split into pairs of two bands with gaps of 0.05 and 0.1 eV, respectively.

Figure 2.3 shows the band structures of OsO_2 in the rutile structure without (2.3c) and with (2.3d) SOC, respectively. Dirac-like energy dispersion along the Z-Γ direction in the BZ is present, similar to RuO_2. Osmium is much heavier than ruthenium because of the presence of the lanthanides in the periodic table, so the effect of SOC in the band structure is more prominent for OsO_2. This is quite obvious for the states which are in the X-R and R-Z direction. The doubly degenerate states at -0.6 and 1.2 eV at R split into two bands with gaps of 0.25 and 0.35 eV, respectively. In spite of having larger SOC in OsO_2, the linear dispersion and degeneracy of the linear bands at Z are *unaffected*. Similarly, these states merge at Z then split into bands with linear dispersion again along the Z-Γ direction. For the optimized OsO_2 the degenerate states at Z are 0.12 eV above the Fermi level. The effect of the SOC around the Fermi level appears along the M-A direction where two crossing bands are split because of the SOC.

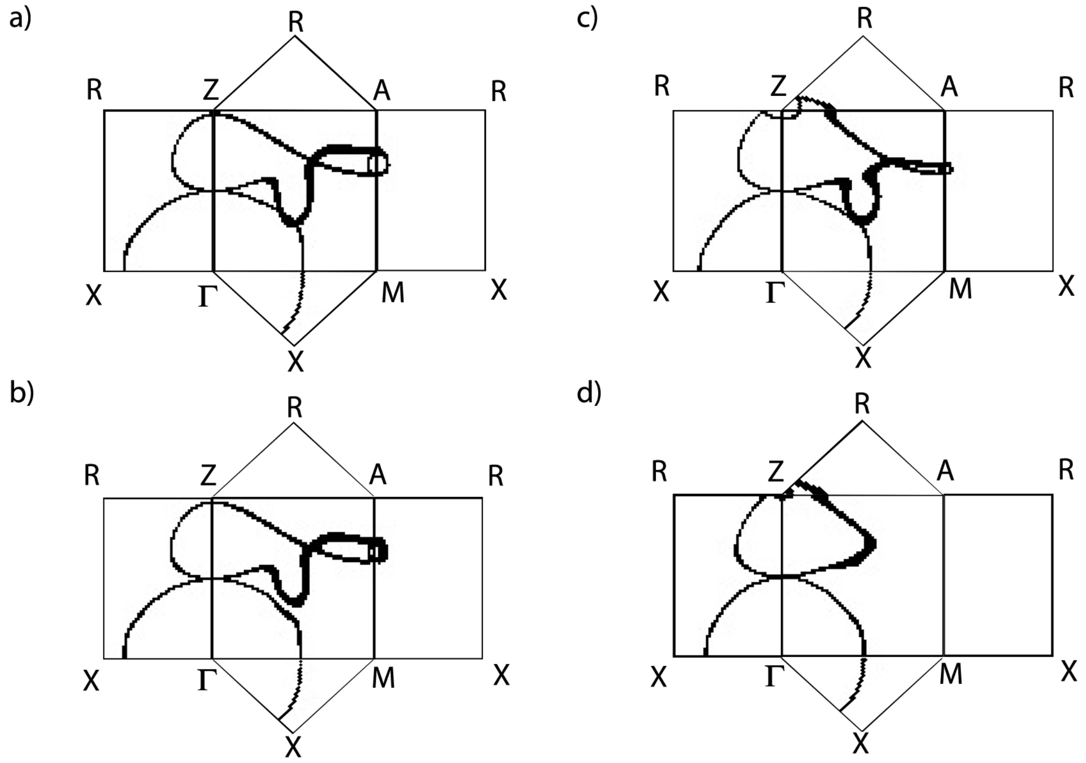

Figure 2.4: Fermi surfaces of optimized bulk RuO_2 (without (a) and with (b) SOC) and OsO_2 (without (c) and with (d) SOC). The width of the lines is a measure of the effective mass of the charge carrier.

The Fermi surfaces of optimized bulk RuO_2 and OsO_2 are shown in Figure 2.4 with and without SOC. The Fermi surface of RuO_2 hardly changes because of the SOC. However, the effect of the SOC on the Fermi surface is greater for OsO_2 (Figure 2.4c and d), as expected because the SOC is almost 9 times stronger compared with RuO_2. The topology of the Fermi surface in the ΓZAM plane changes drastically with the inclusion of the SOC into the calculation.

RuO_2 and OsO_2 have abnormal thermal expansion. With increasing temperature the a and b lattice parameters expand but the c lattice parameter shrinks for RuO_2 and stays constant for OsO_2.[50–52] That is why a small change in temperature affects the c/a ratio of the lattice significantly. In order to investigate the effect of the change in c/a ratio on the electronic structure we perform several calculations including SOC for a different c/a ratio while keeping the volume of the unit cell constant.

Figure 2.5 shows the energy of the Fermi level and the energy of degenerate states at Z as a function of the c/a ratio for RuO_2 and OsO_2. We keep the Fermi energy at 0 eV for each calculation and plot the relative energy of the degenerate states at Z. At low c/a ratios the energy of the degenerate states stays below the Fermi level. For a

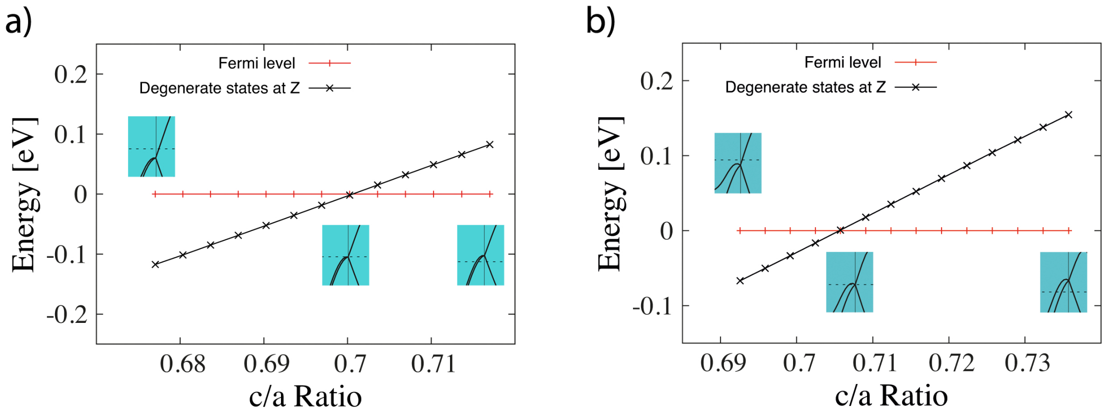

Figure 2.5: The energy of degenerate states at point Z in the BZ and the Fermi level of the bulk RuO_2 (a) and OsO_2 (b) as a function of c/a ratio. The subfigures show the position of Fermi level and the degenerate states for specific c/a ratio; 0.677, 0.700 and 0.717 for RuO_2 and 0.693, 0.705 and 0.735 for OsO_2 from left to right, respectively.

specific c/a ratio the Fermi level and the degenerate states are the same, this is 0.700 for RuO_2 and 0.705 for OsO_2. Then, for higher c/a ratios the energy of these states are above the Fermi level. Since these degenerate states have linear dispersion along Z to Γ, they are expected to have a large contribution to the electrical conductivity when they coincide with the Fermi level of the system.

The linearity of the bands at the Fermi level matters for the physical properties of the materials. Perfectly linear bands at the Fermi level can be obtained when the Fermi energy and the starting point of these bands coincide with each other. The reason is that the bands can actually keep their perfect linearity only in a small range.

In Figure 2.6 a 3 dimensional energy dispersion plot of the bands which have linear energy dispersion at Z in the BZ is shown. We calculate the energy values including SOC for the ΓXRZ plane in the vicinity of the Fermi surface. Then we plot the eigenvalues of the bands which have linear energy dispersion at Z for RuO_2 (Figure 2.6a) and OsO_2 (Figure 2.6b). The calculations are performed using the specific c/a ratio where the starting point of the Dirac-like dispersion and the Fermi level coincide. In order to show the linearity of the bands more explicitly, we double the ΓXRZ plane while plotting the energy values. The effect of SOC on the electronic structure of the materials can also be seen in Figure 2.6. Since the SOC is $\sim$ 9 times stronger in OsO_2 compared to RuO_2, the splitting of two sheets is more obvious in Figure 2.6b.

The evolution of the Fermi surface with changing the c/a ratio of the system can be seen in Figure 2.7 and Figure 2.8. The Fermi surfaces do not change drastically with changing c/a ratio. The main modification happens around Z for both materials. The hole around Z disappears when the c/a ratio is reduced. In addition, for RuO_2

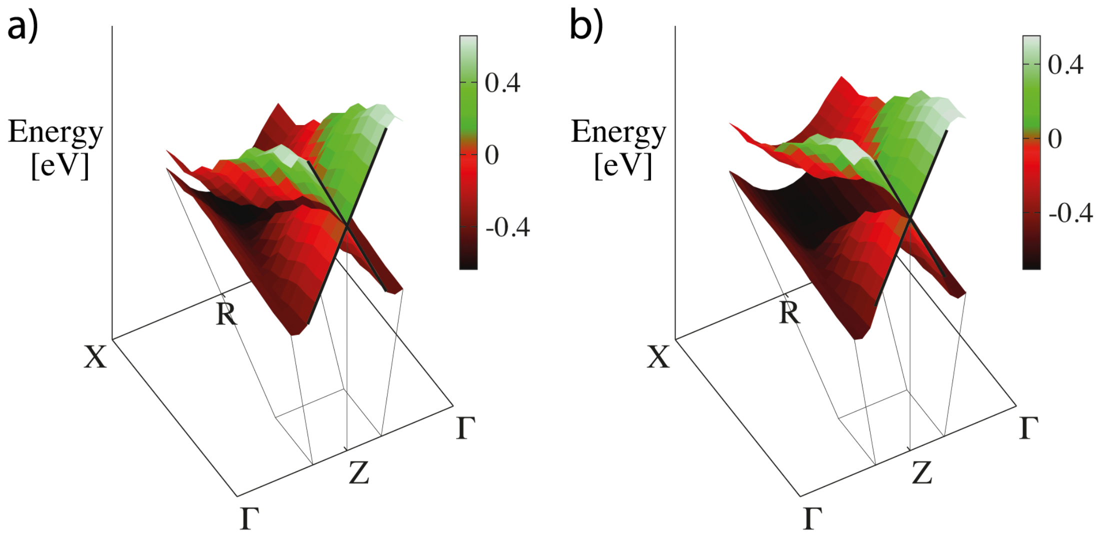

Figure 2.6: 3 dimensional energy dispersion for the bands which have linear energy dispersion at Z in the BZ of a) RuO_2 and b) OsO_2.

some states appear in the ΓXRZ plane for smaller c/a ratio.

2.3 Conclusions

In this chapter, we report electronic structure calculations on RuO_2 and OsO_2 including SOC. We stress the importance of the Dirac-like linear energy dispersion in the band structure of RuO_2 and OsO_2 along the Z-Γ direction. We show that SOC has no influence on neither the linear dispersion of the bands along the Z-Γ direction nor the degeneracy of the bands at Z in the BZ.

Since RuO_2 and OsO_2 have abnormal thermal expansion, small variations in temperature have considerable effect on the c/a ratio of the compounds. Our calculations reveal that the variation in c/a ratio does not have serious effect on the general appearance of the Fermi surface. However, it has significant effect on the starting point of the Dirac-like dispersion at Z relative to the Fermi level. In addition, we show that for a specific c/a ratio , the degenerate states at Z in the BZ coincide with the Fermi energy. This should be important for the electron transport of these two materials at low temperature. The sensitivity of the electron mobility of RuO_2 to small variations in chemical composition can be related to this observation, also.

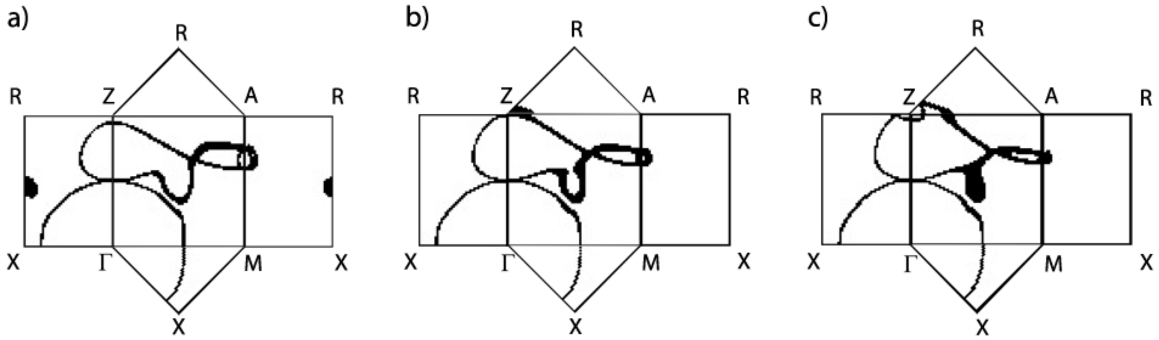

Figure 2.7: The evolution of Fermi surface of RuO_2 rutile with increasing c/a ratio including SOC, a) 0.677, b) 0.700 and c) 0.717. The width of the lines is a measure of the effective mass of the charge carrier.

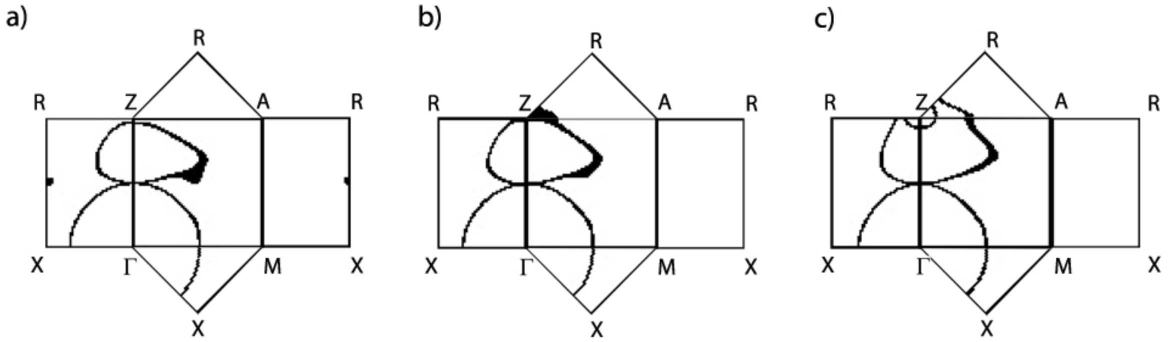

Figure 2.8: The evolution of Fermi surface of OsO_2 rutile with increasing c/a ratio including SOC, a) 0.693, b) 0.705 and c) 0.735. The width of the lines is a measure of the effective mass of the charge carrier.

Bibliography

1. E. Kolawa, F. C. T. So, E. T. Pan, and M. Nicolet, Applied Physics Letters **50**, 854 (1987).
2. D. J. Pedder, ElectroComponent Science and Technology **2**, 259 (1976).
3. O. Barbieri, M. Hahn, A. Foelske, and R. Kötz, Journal of Electrochemical Society **153**, A2049 (2006).
4. P. Balaya, H. Li, L. Kienle, and J. Maier, Advanced Functional Materials **13**, 621 (2003).
5. A. M. Stux and K. E. Swider-Lyons, Journal of Power Sources **165**, 635 (2007).
6. Y.-L. Chueh, C.-H. Hsieh, M.-T. Chang, L.-J. Chou, C. S. Lao, J. H. Song, J.-Y. Gan, and Z. L. Wang, Advanced Materials **19**, 143 (2007).
7. G. Lodi, E. Sivieri, A. Debattisti, and S. Trasatti, Journal of Applied Electrochemistry **8** 135 (1978).
8. C.-C. Chang and T.-C. Wen, Journal of Applied Electrochemistry **27**, 355 (1997).
9. H. Schäfer, G. Schneidereit, and W. Gerhardt, Zeitschrift für anorganische und allgemeine Chemie **319**, 327 (1963).
10. D. B. Rogers, R. D. Shannon, A. W. Sleight, and J. L. Gillson, Inorganic Chemistry **8**, 841 (1969).
11. W. D. Ryden, and A. W. Lawson, and C. C. Sartain, Phys. Rev. B **1**, 1494 (1970).
12. W. D. Ryden, Lawson A.W., and C. C. Sartain, Physics Letters A **26**, 209 (1968).
13. R. A. de Groot, M. W. Shafer, and B. L. Olson, IBM Technical Disclosure Bulletin **124**, 843 (1977).
14. J. J. Lin, S. M Huang, Y. H. Lin, T. C. Lee, H. Liu, X. X. Zhang, R. S. Chen, and Y. S. Huang, Journal of Physics: Condensed Matter **16**, 8035 (2004).
15. D. P. Divincenzo and E. J. Mele, Phys. Rev. B **29**, 1685 (1984).

16. F. D. M. Haldane, Phys. Rev. Lett. **61**, 2015 (1988).
17. K. S. Novoselov, A. K. Geim, S. V. Morozov, D. Jiang, Y. Zhang, S. V. Dubonos, I. V. Grigorieva, and A. A. Firsov, Science **306**, 666 (2004).
18. K. S. Novoselov, A. K. Geim, S. V. Morozov, D. Jiang, M. I. Katsnelson, I. V. Grigorieva, S. V. Dubonos, and A. A. Firsov, Nature **438**, 197 (2005).
19. A. K. Geim and K. S. Novoselov, Nature Materials **6**, 183 (2007).
20. A. H. Castro Neto, F. Guinea, N. M. R. Peres, K. S. Novoselov, and A. K. Geim, Rev. Mod. Phys. **81**, 109 (2009).
21. S. M. Young, S. Zaheer, J. C. Y. Teo, C. L. Kane, E. J. Mele, and A. M. Rappe, Phys. Rev. Lett. **108**, 140405 (2012).
22. S. Y. Zhou, G.-H. Gweon, J. Graf, A. V. Fedorov, C. D. Spataru, R. D. Diehl, Y. Kopelevich, D.-H. Lee, S. G. Louie, and A. Lanzara, Nature Phys. **2**, 595 (2006).
23. V. Pardo and W. E. Pickett, Phys. Rev. Lett. **102**, 166803 (2009).
24. S. Banerjee, R. R. P. Singh, V. Pardo, and W. E. Pickett, Phys. Rev. Lett. **103**, 016402 (2009).
25. V. Pardo and W. E. Pickett, Phys. Rev. B **81**, 035111 (2010).
26. J. A. Steinberg, S. M. Young, S. Zaheer, L. Kane, C., J. Mele, E., and A. M. Rappe, Phys. Rev. Lett. **112**, 036403 (2014).
27. S. M. Young, S. Chowdhury, E. J. Walter, E. J. Mele, C. L. Kane, and A. M. Rappe, Phys. Rev. B **84**, 085106 (2011).
28. L. F. Mattheiss, Phys. Rev. B **13**, 2433 (1976).
29. J. H. Xu, T. Jarlborg, and A. J. Freeman, Phys. Rev. B **40**, 7939 (1989).
30. K. M. Glassford and J. R. Chelikowsky, Phys. Rev. B **49**, 7107 (1994).
31. O. V. Krasovska, E. E. Krasovskii, and V. N. Antonov, Phys. Rev. B **52**, 11825 (1995).
32. B. Yu. Yavorsky, O. V. Krasovska, E. E. Krasovskii, A. N. Yaresko, and V. N. Antonov, Physica B: Condensed Matter **225** 243 (1996).
33. G. L. Zhao, D. Bagayoko, and T. D. Williams, Phys. Rev. B **60**, 1563 (1999).
34. J. S. Tse, D. D. Klug, K. Uehara, Z. Q. Li, J. Haines, and J. M. Léger, Phys. Rev. B **61**, 10029 (2000).
35. R. Wu and W. H. Weber, Journal of Physics: Condensed Matter **12**, 6725 (2000).
36. H. W. Hugosson, G. E. Grechnev, R. Ahuja, U. Helmersson, L. Sa, and O. Eriksson, Phys. Rev. B **66**, 174111 (2002).
37. K.-P. Bohnen, R. Heid, O. de la Peña Seaman, B. Renker, P. Adelmann, and H. Schober, Phys. Rev. B **75**, 092301 (2007).
38. P. Hohenberg and W. Kohn, Phys. Rev. **136**, B864 (1964).

39. W. Kohn and L. J. Sham, Phys. Rev. **140**, A1133 (1965).
40. G. Kresse and J. Furthmüller, Phys. Rev. B **54**, 11169 (1996).
41. G. Kresse and J. Furthmüller, Comput. Mat. Sci. **6**, 15 (1996).
42. P. E. Blöchl, Phys. Rev. B **50**, 17953 (1994).
43. G. Kresse and D. Joubert, Phys. Rev. B **59**, 1758 (1999).
44. J. P. Perdew, K. Burke, and M. Ernzerhof, Phys. Rev. Lett. **77**, 3865 (1996).
45. H. J. Monkhorst and J. D. Pack, Phys. Rev. B **13**, 5188 1976.
46. R. W. G. Wyckoff, Crystal structures volume 1, Wiley (1963).
47. Y. Hayakawa, S. Kohiki, M. Arai, H. Yoshikawa, S. Fukushima, K. Wagatsuma, M. Oku, and F. Shoji, Phys. Rev. B **59**, 11125 (1999).
48. R. R. Daniels, G. Margaritondo, C.-A. Georg, and F. Lévy, Phys. Rev. B **29**, 1813 (1984).
49. H. M. Tsai, P. D. Babu, C. W. Pao, J. W. Chiou, J. C. Jan, K. P. Krishna Kumar, F. Z. Chien, W. F. Pong, M.-H. Tsai, C.-H. Chen, L. Y. Jang, J. F. Lee, R. S. Chen, Y. S. Huang, and D. S. Tsai, Applied Physics Letters **90**, 042108 (2007).
50. Y. C. Venudhar, L. Iyengar, and K. V. K. Rao, Crystal Research and Technology **20**, 1393 (1985).
51. K.-I. Murai, Y. Akune, Y. Suzuki, T. Moriga, and I. Nakabayashi, International Journal of Modern Physics B **20**, 4111 (2006).
52. K. V. K. Rao and L. Iyengar, Acta Crystallographica Section A-Crystal Physics Diffration Theoretical and General **25**, 302 (1969).

CHAPTER 3

Role of magnetism in Catalysis: RuO_2 (110) surface

Abstract

Angular momentum seems not to be conserved in chemical reactions where *one* of the reactants or products is magnetic; consequently, such reactions show a high activation barrier. An example is the production of hydrogen by electrolysis of water: practically all losses occur in the production of (magnetic) oxygen molecules. Anodes with a low overvoltage (a measure of the losses) are based on the ruthenium dioxide (110) surface. In this chapter we present first-principles electronic structure calculations show that this surface itself carries magnetic moments. This magnetic surface enables the production of oxygen molecule in the ground state while conserving angular momentum.

Most of this chapter has been published in J. Phys. Chem. C **117**, 6353 (2013) by E. Torun, C. M. Fang, G. A. de Wijs and R. A. de Groot.

3.1 Introduction

Electrolysis of water is a potential source of hydrogen on a large scale. A measure of the inefficiency in electrolysis is the overvoltage: the voltage needed to drive the process in excess of the voltage under thermodynamical equilibrium conditions. The contribution of the oxygen evolution to the overvoltage dominates overwhelmingly.[1] One of the best anodes in this respect is based on the RuO_2 (110) surface because of its low overvoltage.[2,3] Several experimental and theoretical attempts are performed to figure out the details of oxygen evolution reaction (OER) on RuO_2, particularly for its (110) surface. The RuO_2 (110) surface is a very active catalyst for oxidation For example, the initial sticking parameter of O_2 on this specific surface is 0.7[4], this means that O_2 adsorption is not a limiting step for oxidation catalysis. Presence of bridging and terminal oxygen species on the surface and having moderate adsorption energy of reactants are listed as the important properties which make RuO_2 an active catalyst.[5]

The OER on the RuO_2 (110) surface starts with splitting of a water molecule according to the mechanism suggested in reference 2

$$S + H_2O \rightarrow S - OH + H^+ + e^-, \tag{3.1}$$

where S is the active surface site. Then OH loses its proton

$$S - OH \rightarrow S - O + H^+ + e^-. \tag{3.2}$$

Then two OH molecules on the surface merge

$$S - OH + S - OH \rightarrow S - O + S + H_2O. \tag{3.3}$$

Finally the oxygen molecule is produced by a surface oxygen coupling step

$$S - O + S - O \rightarrow O_2 + 2S. \tag{3.4}$$

In this reaction path the rate limiting step shifts at ~ 1.52 V from the step in which OH losses its proton (Equation 3.2) to the first step of the reaction path (Equation 3.1). The oxygen coupling step (Equation 3.4) is not the rate limiting step for electrolysis of water on the RuO_2 (110) surface.[2]

Very valuable informations about the OER on RuO_2 (110) is also reported in theoretical work. For example, Nørskov and co-workers suggest that the binding energies of intermediate products (O, HO and HOO) are crucial for electrocatalytic activity of the anodes. They conclude that the reason why RuO_2 shows lower overpotential than other metal anodes is a result of weak O but strong HO binding to the RuO_2 (110) surface.[6–8] Another important conclusion is reached by Liu and co-workers. They suggest that the terminal O atom plays an important role in the H_2O activation. That is why the differential adsorption energy of the terminal O atom has considerable effect on the OEA.[9] All these discussions shed light on the underlying mechanism of the OER but the complete picture is not clear yet.

Because oxygen evolution produces magnetic O_2 from non-magnetic water, the inclusion of the effects of surface magnetism could be highly relevant.[10] Neither water nor hydrogen is magnetic, so O_2 can be produced only in a non-magnetic excited state without violating conservation of angular momentum on a non-magnetic anode. The two lowest excited states of the oxygen molecule are singlet states, $^1\Delta_g$ and $^1\Sigma_g$, 1 and 1.6 eV above the $^3\Sigma_g$ ground state.[11] The ground state of the oxygen molecule is a spin triplet in which two unpaired electrons occupy a twofold degenerate anti-bonding π^* orbital.[12] So, the ground state O_2 carries a paramagnetic moment of 2 μ_B.

For non-magnetic anodes, we associate the high overvoltage with the notion that O_2 is produced initially in its non-magnetic excited state and decays slowly to the ground state by higher order processes. A detailed study of the energetics of the oxygen evolution on the RuO_2 (110) surface was reported by Rossmeisl et al.[13] This work did not include the influence of magnetism, however.

Here we report on the local electronic and magnetic properties of RuO_2 (110) surfaces. We show that the RuO_2 (110) surface is magnetic. This is an unexpected property because bulk RuO_2 is not magnetic. Magnetism in 4d and 5d metals and their compounds is rare but not unique[14–16]; for example magnetic properties of RuO_2 nanoparticles have been investigated.[17,18] The surface magnetism that we report here is an important property because it provides the necessary degree of freedom to allow the production of O_2 in its magnetic ground state while conserving angular momentum.

3.2 Details of the Calculations

Experimental[19–22] and theoretical analyses[23–31] show that the RuO_2 (110) surface has two different ruthenium atoms, one with six-fold coordination by oxygen (Ru2) and one with a five-fold coordination (Ru1). The latter is regarded as the active site in catalysis.[19–31] Previous studies have focused on surface morphologies and local atomic structure. Scheffler et al. found that the clean surface exists in an oxygen-poor environment. Whereas in oxygen-rich environment the stable form of the RuO_2 (110) surface has terminal oxygen on top of the Ru1 atoms.[26–29]

RuO_2 can be regarded as consisting of alternate layers of oxygen and Ru_2O_2 layers along the (110) direction. We cleave the crystal in the O atomic layer; a surface oxygen atom (O_1) bridges two Ru2 atoms. A unit cell of 3.14 Å × 6.43 Å × 25.00 Å containing 24 atoms in 9 atomic layers in a slab with 12 Å vacuum between them was

Table 3.1: Calculated results (lattice parameters and coordinates of oxygen atoms) of bulk RuO_2 rutile using the DFT-GGA method. V is the volume of the unit cell.

	this work	previous calculations	experiments
a (Å)	4.55	4.554[40], 4.56[41]	4.51[42],4.4919[43] 4.4906[44]
c (Å)	3.14	3.137, 3.16	3.11, 3.1066 3.1064
c/a	0.69	0.6888, 0.6930	0.6896, 0.6916 0.6918
$u(\mathrm{O})$	0.306	0.3054, 0.3067	0.3058
V($Å^3$/ fu)	32.42	32.53, 32.10	31.63, 31.32 31.32

employed.

First-principle calculations were carried out using the first-principles code "Vienna Ab initio Simulation Program" (VASP)[32–35] employing density functional theory (DFT), and the Projector-Augmented Wave (PAW) method.[36,37] The generalized gradient approximation (GGA) by Perdew, Burke, and Ernzerhof (PBE)[38,39] was employed for the exchange and correlation potentials. The Brillouin zone (BZ) integration used an $8 \times 8 \times 12$ k-mesh or 105 k-points in the irreducible BZ of bulk RuO_2. For the (110) surfaces the electronic wave functions were sampled on a $12 \times 6 \times 1$ k-mesh or 28 k-points in the irreducible BZ. The cutoff energy of the wave functions was 500 eV. The structures are optimized until all forces were smaller than 0.01 eV/Å . The convergences with the cutoff energies and k-meshes have been verified. In this chapter we perform spin-polarized DFT calculations in which the effect of spin-orbit coupling is not included. This means that we do not have a spin quantization axis in our calculations. The magnetic moments provided in this chapter are the difference between the majority and the minority spin charge densities.

3.3 Clean RuO_2 (110) Surface

The results of structural relaxations of bulk RuO_2 are in line with former calculations[40,41]; see Table 3.1. Calculations for the relaxed RuO_2 (110) surface using the spin-polarized DFT-GGA method resulted in a magnetic solution 38 meV lower in energy compared with the non-magnetic solution. The spin-polarization is confined

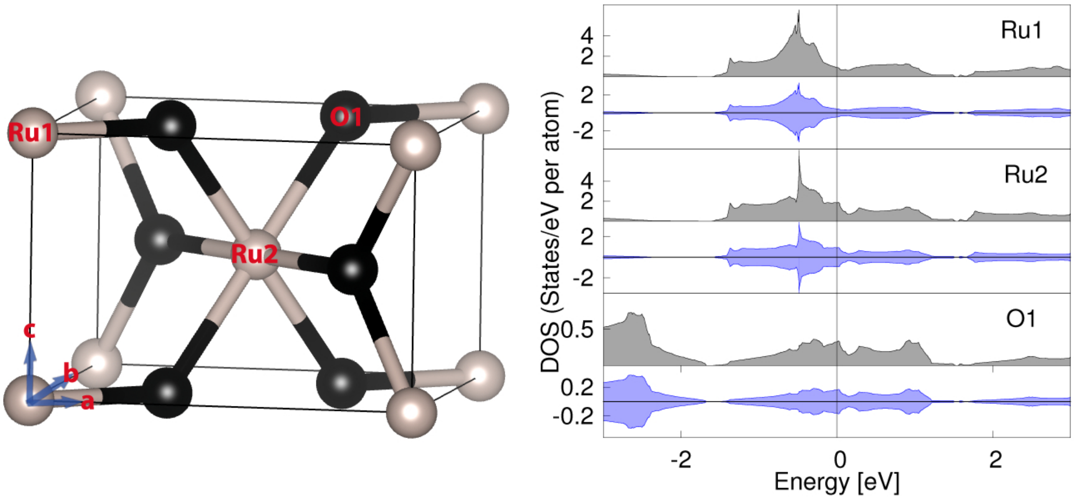

Figure 3.1: Crystal structure of rutile RuO_2 and partial DOS' of indicated atoms in the Figure. The first black channels are the non-spinpolarized, the second and third blue ones are the spin up and spin down partial DOS' for each atom.

to the surface atoms: 0.60 μ_B for Ru2, -0.24 μ_B for Ru1 and 0.19 μ_B at the bridging oxygen site (O1) (See Table 3.2). The total magnetization of each surface of the slab is 0.55 μ_B. Figure 3.3 reveals the origin of the surface magnetism: it shows the partial density of states (DOS) of the surface ruthenium 4d and oxygen 2p states around the Fermi level for the non-magnetic and the magnetic cases. Both non-magnetic DOS' peak at the Fermi level which is not present in the DOS of bulk rutile RuO_2 (Figure 3.1). The spin-polarization causes a moderate splitting of the DOS of the Ru1 4d states, consistent with its magnetic moment (about -0.24 μ_B). The shape of the partial DOS of the surface ruthenium 4d states is significantly different from that of the bulk due to a different crystal field splitting.

The O1 2p states have a density of $\sim$ 0.80 states/eV per atom at the Fermi level. That is significantly larger than those in the sub-surface layer and bulk (typically around 0.2 states/eV per atom). Calculations show a spin splitting of about 0.8 eV with a peak at about -0.3 eV for the spin-up electrons and another peak at about 0.5 eV for the spin-down electrons. As a result, there is a magnetic moment of $\sim$ 0.19 μ_B at the bridging oxygen site. The spin-polarization shows little effect on the subsurface O atoms.

Because surface magnetism is a subtle effect, we also perform WIEN2k[45] calculation for clean RuO_2 (110) surface to make a benchmark. We chose WIEN2k for benchmarking because WIEN2k and VASP are different DFT methods. WIEN2k is a full potential linearized augmented plane wave (LAPW) method where VASP is a plane-wave method. For WIEN2k calculations, a 3.14 Å × 6.43 Å × 25.00 Å unit cell was used that contains 24 atoms in 9 atomic layers and also approximately 12 Å vac-

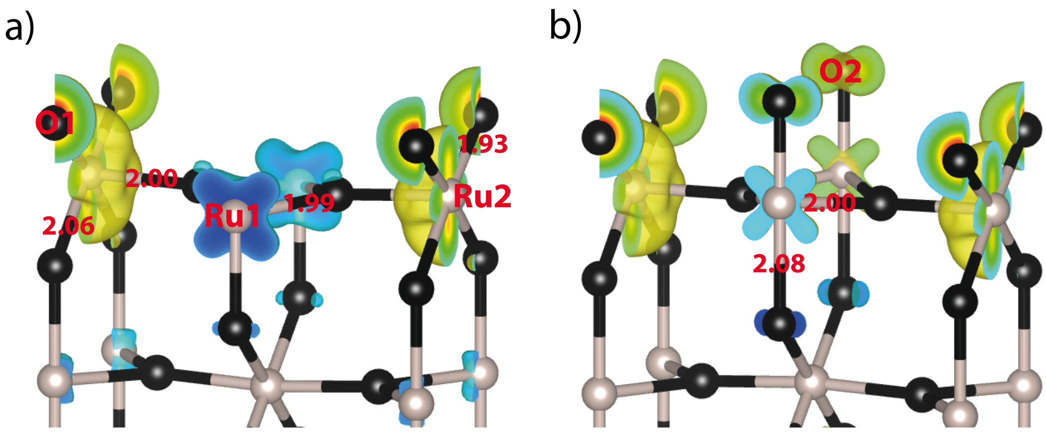

Figure 3.2: Local coordination and the spin density of the RuO$_2$ (110) surfaces. Blue corresponds to negative; red corresponds to positive spin density. (a) Bridging O (O1) atoms, six-fold coordinated Ru atoms (Ru2), and five-fold coordinated Ru atoms (Ru1).(b) surface with oxygen coverage: the Ru1 is covered by one O (O2). The numbers represent the Ru-O bond lengths (in Angstroms).

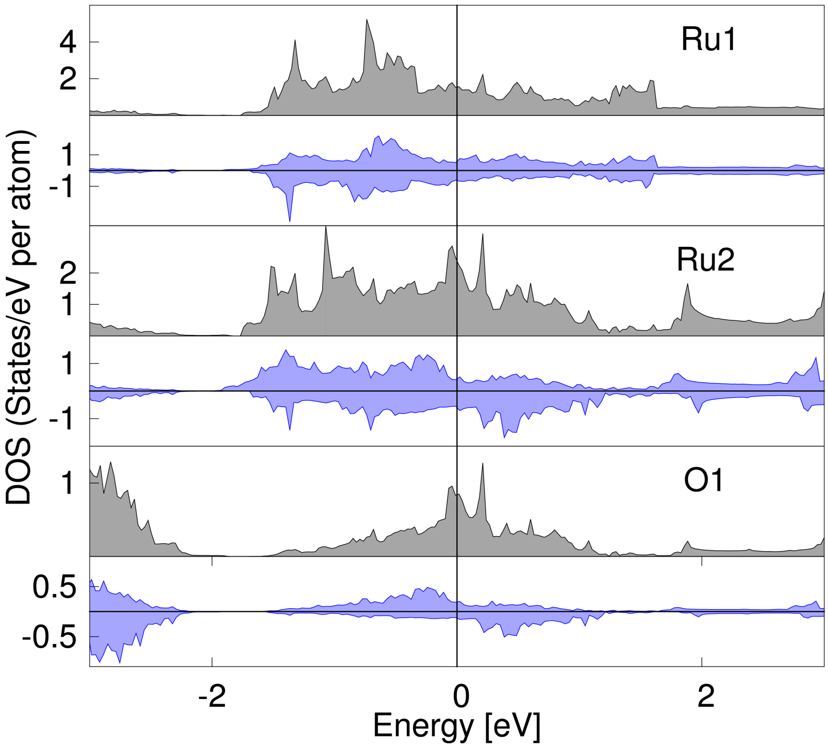

Figure 3.3: Partial DOS' of the surface O and Ru states of the RuO$_2$ (110) surface showing the effect of spin-polarization. The first black channels are the non-spinpolarized, the second and third blue ones are the spin up and spin down partial DOS' for each atom. Remark the maxima at the Fermi energy for several non-spinpolarized cases.

Table 3.2: Surface energy and local moments of RuO$_2$ rutile (110) and (110)-O surfaces using the DFT-GGA method.

	moment (μ_B)				E$_{surf}$ (J/m^2)		E$_{sp}$-E$_{nm}$ (meV/cell)
	Ru1	Ru2	O1	O2	present	literature	
(110)	-0.24	0.60	0.19		1.04	1.14[22],1.03[23]	-38
(110)-O	0.10	0.69	0.29	0.14			-53

uum. This is the same unit cell that we use in VASP calculations. The electronic wave functions are sampled on 12 × 6 × 1 k-mesh or 18 k-points in the irreducible BZ using the Monkhorst-Pack method.[46] Finally, we observe that the relaxed geometries for VASP and WIEN2k are almost the same. The total magnetic moments per surface unit cell for VASP and WIEN2k are close to each other, 0.56 and 0.52 μ_B respectively, which we consider to be a good agreement. So, WIEN2k calculations confirm that the RuO$_2$ (110) surface is magnetic.

3.4 O-Covered RuO$_2$ (110) Surface

In Figure 3.2b the oxygen covered RuO$_2$ (110) surface is shown. The addition of oxygen on top of Ru1 (Figure 3.2b) has a profound influence; see Table 3.2. The Ru1 shifts 0.09 Å outward, in contrast with the clean surface, where it moved 0.07 Å inward. The new Ru-O bond is short, 1.73 Å, on the expense of the Ru-O bond to the oxygen below, which expands from 1.90 Å in the clean surface to 2.08 Å in case of an extra oxygen. The addition of an oxygen atom on top of the Ru1 atom slightly perturbs the local coordination of the Ru2 atom. The Ru2 atom and the bridging O atom move slightly inward. The magnetic ground state is more stable by 53 meV compared with the non-magnetic case, which is 15 meV more compared with the case without oxygen coverage.

Figure 3.4 shows the calculated partial DOS' of the ruthenium 4d and oxygen 2p states of the oxygen-covered surface. The peak positions and widths of the densities of states of the Ru2 4d and the bridging O 2p states are basically the same as those of the clean surface. Spin-polarization has a significant influence on the non-magnetic partial DOS'.

The partial density of the Ru1 4d states of the oxygen-covered surface have significantly different shape as compared with that of the clean surface (Figures 3.3 and 3.4). There are two strong peaks at about -1.0 eV and +0.4 eV. Spin-polarization

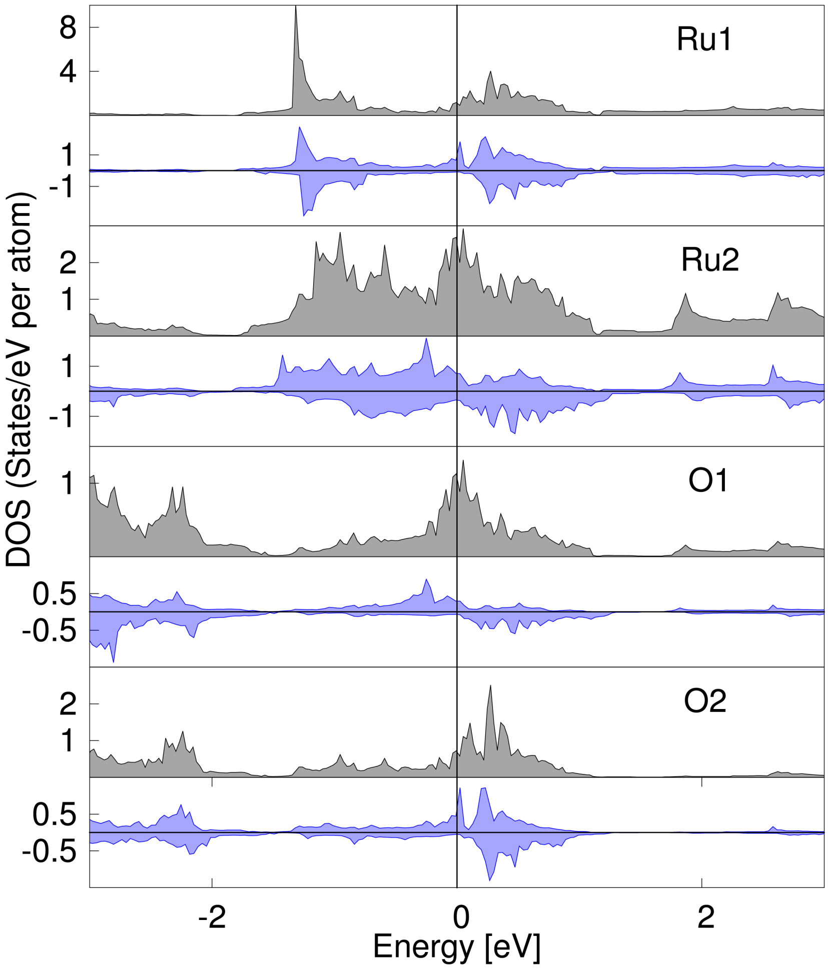

Figure 3.4: Partial DOS' of the surface O and Ru states of the RuO_2 (110) surface with oxygen coverage on top of Ru1 showing the effect of spin-polarization. The first black channels are the non-spinpolarized, the second and third blue ones are the spin up and spin down partial DOS' for each atom. Remark the maxima at the Fermi energy for several non-spinpolarized cases.

has much less influence on the Ru1 4d and terminal O (O2) 2p states. The magnetic moments of the Ru2 and Ru1 are parallel, in contrast with the case of the clean surface.

On the oxygen-covered RuO_2 (110) surface, the local magnetic moments of the Ru2 and bridging O atoms are close to those for the clean surface. The moment of the Ru1 on the oxygen-covered surface remains very small ($\sim 0.1\ \mu_B$), but aligns parallel. Therefore, the total magnetic moment of the oxygen-covered surface increases to 1.22 μ_B per unit cell from 0.55 μ_B per unit cell for the clean (110) surface.

3.5 Role of Surface Magnetism in Electrolysis of Water

One of the suggested reaction mechanisms for water electrolysis on the 2×1 RuO_2 (110) surface is proposed by Rossmeisl et al. [13] as follows

$$\begin{aligned} 2H_2O &\rightarrow S - HO + H_2O + H^+ + e^-, \\ &\rightarrow S - O + H_2O + 2H^+ + 2e^-, \\ &\rightarrow S - HOO + 3H^+ + 3e^-, \\ &\rightarrow O_2 + 4H^+ + 4e^-. \end{aligned} \tag{3.5}$$

Where S is the active surface site. This reaction mechanism is different from the suggested experimental mechanism that we discussed previously. However, it is widely used to model the electrolysis of water on the RuO_2 (110) surface.

The conservation of angular momentum and the surface magnetism are playing a vital role, mostly at the final step of this reaction path, because O_2 is produced as a final product. That is why, to elucidate the importance of the surface magnetism for electrolysis of water, we perform DFT total energy calculations for the last step of this reaction path. In Figure 3.5, the initial and the final states of the final step of electrolysis of water can be seen. Initially, OOH is adsorbed on the coordinately unsaturated site (CUS), which is the position of the fivefold coordinated ruthenium atom, of the 2×1 RuO_2 (110) surface and finally O_2 desorbs from the surface after removal of the H atom.

We performed two different sets of calculation that we name as “Singlet” and “Triplet”. In the “Singlet” case, we assume that the RuO_2 (110) surface is not magnetic so the O_2 should be produced initially in its non-magnetic singlet excited state. For this scenario, we obtained the total energy difference between these two states from non-spinpolarized DFT calculations. For the “Triplet” case, surface magnetism enables the production of O_2 in its magnetic ground state. First, we performed spin-polarized DFT calculations to find the magnetic moments of the atoms in the initial

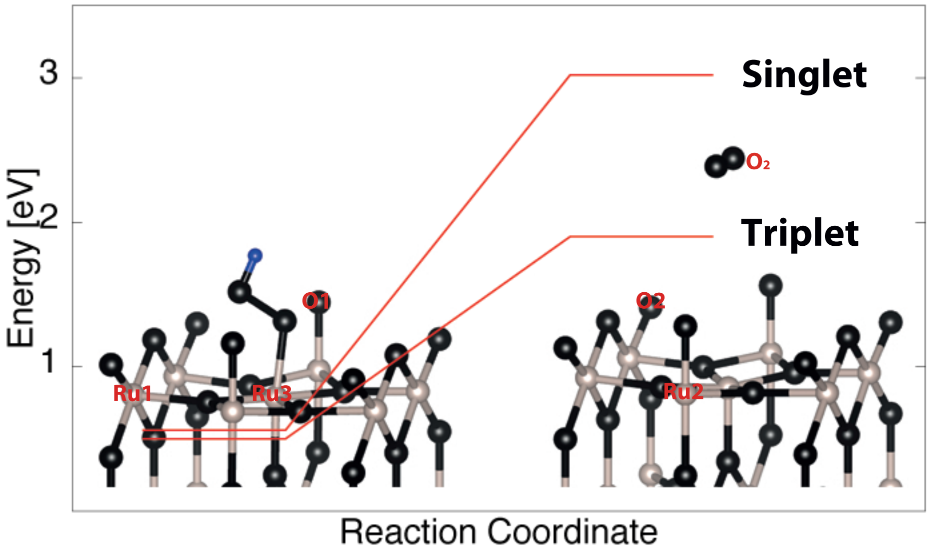

Figure 3.5: Calculated total energy change for the last step of the water electrolysis, for magnetic ("Triplet") and non-magnetic ("Singlet") anode. The energy of $1/2H_2$ is added to the final-state total energies.

Table 3.3: Total and Local Magnetic Moments for the Initial and the Final States of the Last Step of the Water Electrolysis.

			moment (μ_B)				
	Ru1	Ru2	Ru3	O1	O2	O_2	Total
Initial	0.49	0	0	0	0.17	–	2.41
Final	-0.49	-0.22	0	-0.24	-0.19	2	2.41

state (Table 3.3). Then we imposed the same total spin angular momentum on the final state and obtained the oxygen molecule in its triplet magnetic ground state. We observe that surface atoms rearrange their moments to conserve total spin angular momentum in the unit cell while obtaining the O_2 in its magnetic ground state. We also observe that the total energy change in the "Triplet" case is $\sim$ 1 eV *lower* than the "Singlet" case, which can be seen in Figure 3.5.

3.6 Conclusions

Magnetism usually occurs in materials containing elements where a certain angular momentum appears first. The orthogonality of the valence electrons (that carry the magnetic moment) to the core is always fulfilled, so no constraints exist on the radial Schrödinger equation (any constraint increases the energy and hence the delocalization of these states), but several exceptions exist; for example, strontiumruthenate is ferromagnetic. In general, surfaces with atoms with a lower coordination show an increased tendency toward magnetism. Magnetism is the rule rather than the exception in isolated atoms, but also isolated 4d atoms in an alkali-metal matrix show local moments.[47]

The calculations presented here show that both the (110) stoichiometric and the oxygen-covered surfaces of ruthenium dioxide show local magnetic moments. The relevance of the surface magnetism reported in this chapter is in electrolysis. The importance of surface magnetism for electrolysis of water is also illustrated.

The spin-conservation rule (or angular momentum conservation) is a key selection rule for chemical reactions.[48] The importance of the spin-selection rule can be seen in work by Scheffler's group.[49] They suggest that the origin of the low sticking parameter of O_2 on the Al(111) surface is having O_2 in a triplet and the Al(111) surface in a singlet state. Another example is in a recent review where Chretien and Metiu pointed out that from a quantum mechanics point of view, reactions in which the total spin of the reactants differs from the total spin of the products are very slow.[10]

A comparison with the most fundamental form of oxygen-evolution, photosynthesis, is in order here. In photosynthesis, carbon dioxide and water are transformed into oxygen and organic compounds by sunlight, a process in which magnetic oxygen is the only magnetic reactant as well. Photosynthesis is *impossible* without traces of manganese. The production of oxygen in photosynthesis is a four step process that involves a polynuclear, magnetic cluster containing four manganese ions.[50] A second magnetic entity seems ubiquitous in the production of molecular oxygen.

Bibliography

1. M. H. Miles, E. A. Klaus, B. P. Gunn, J. R. Locker, W. E. Serafin and S. Srinivasan, Electrochimica Acta **23**, 521 (1978).
2. G. Lodi, E. Sivieri, A. Debattisti, and S. Trasatti, Journal of Applied Electrochemistry **8**, 135 (1978).
3. C.-C. Chang and T.-C. Wen, Journal of Applied Electrochemistry **27**, 355 (1997).
4. A. Böttcher and H. Niehus, Phys. Rev. B **60**, 14396 (1999).
5. H. Over, Chemical Reviews **112**, 3356 (2012).
6. J. Rossmeisl, A. Logadottir, and J.K. Norskov, Chemical Physics **319**, 178 (2005).
7. J. Rossmeisl, Z.-W. Qu, H. Zhu, G.-J. Kroes, and J.K. Norskov, Journal of Electroanalytical Chemistry **607**, 83 (2007).
8. I. C. Man, H.-Y. Su, F. Calle-Vallejo, H. A. Hansen, J. I. Martínez, N. G. Inoglu, J. Kitchin, T. F. Jaramillo, J. K. Norskov, and J. Rossmeisl, ChemCatChem **3**, 1159 (2011).
9. Y.-H. Fang and Z.-P. Liu, Journal of the American Chemical Society **132**, 18214 (2010).
10. S. Chretien and H. Metiu, Journal of Chemical Physics **129**, 074705 (2008).
11. L. Bytautas, N. Matsunaga, and K. Ruedenberg, Journal of Chemical Physics **132**, 074307 (2010).
12. C. Schweitzer and R. Schmidt, Chemical Reviews **103**, 1685 (2003).
13. J. Rossmeisl, Z. W. Qu, H. Zhu, G. J. Kroes, and J. K. Norskov, Journal of Electroanalytical Chemistry **607**, 83 (2007).
14. J.M. Longo, P. M. Raccah, and J. B. Goodenough, J. Appl. Phys. **39**, 1327 (1968).
15. O. Eriksson, R. C. Albers, and A. M. Boring, Phys. Rev. Lett. **66**, 1350 (1991).

16. P. K. De Boer and R. A. De Groot, Phys. Rev. B **59**, 9894 (1999).
17. C. Diaz, M. L. Valenzuela, E. Spodine, Y. Moreno, and O. Pena, Journal of Cluster Science **18**, 831 (2007).
18. K. Biswas and C. N. R. Rao, Journal of Nanoscience and Nanotechnology **7**, 1969 (2007).
19. H. Over, A. P. Seitsonen, E. Lundgren, M. Schmid, and P. Varga, Surface Science **515**, 143 (2002).
20. H. Over, Applied Physics A-Materials Science & Processing **75**, 37 (2002).
21. H. Over and M. Muhler, Progress in Surface Science **72**, 3 (2003).
22. Y. D. Kim, S. Schwegmann, A. P. Seitsonen, and H. Over, The Journal of Physical Chemistry B **105**, 2205 (2001).
23. H. Wang and William F. Schneider, Journal of Chemical Physics **127**, 064706 (2007).
24. P. Liu, J. T. Muckerman, and R. R. Adzic, Journal of Chemical Physics **124**, 141101 (2006).
25. A. Kiejna, G. Kresse, J. Rogal, A. De Sarkar, K. Reuter, and M. Scheffler, Phys. Rev. B **73**, 035404 (2006).
26. K. Reuter and M. Scheffler, Phys. Rev. B **65**, 035406 (2002).
27. K. Reuter, M. V. Ganduglia-Pirovano, C. Stampfl, and M. Scheffler, Phys. Rev. B **65**, 165403 (2002).
28. K. Reuter and M. Scheffler, Phys. Rev. B **68**, 045407 (2003).
29. K. Reuter and M. Scheffler, Phys. Rev. Lett. **90**, 046103 (2003).
30. Q. Sun, K. Reuter, and M. Scheffler, Phys. Rev. B **67**, 205424 (2003).
31. B. Temel, H. Meskine, K. Reuter, M. Scheffler, and H. Metiu, Journal of Chemical Physics **126**, 204711 (2007).
32. G. Kresse and J. Hafner, Phys. Rev. B **47**, 558 (1993).
33. G. Kresse and J. Hafner, Phys. Rev. B **49**, 14251 (1994).
34. G. Kresse and J. Furthmüller, Comput. Mat. Sci. **6**, 15 (1996).
35. G. Kresse and J. Furthmüller, Phys. Rev. B **54**, 11169 (1996).
36. G. Kresse and D. Joubert, Phys. Rev. B **59**, 1758 (1999).
37. P. E. Blöchl, Phys. Rev. B **50**, 17953 (1994).
38. J. P. Perdew, K. Burke, and M. Ernzerhof, Phys. Rev. Lett. **77**, 3865 (1996).
39. J. P. Perdew, K. Burke, and M. Ernzerhof, Phys. Rev. Lett. **78**, 1396 (1997).
40. J. S. Tse, D. D. Klug, K. Uehara, Z. Q. Li, J. Haines, and J. M. Leger, Phys. Rev. B **61**, 10029 (2000).
41. K. M. Glassford and J. R. Chelikowsky, Phys. Rev. B **47**, 1732 (1993).
42. R. W. G. Wyckoff, Crystal structures volume 1, Wiley (1963).
43. C. E. Boman, Acta Chemica Scandinavica **24**, 116 (1970).

44. D. B. Rogers, R. D. Shannon, A. W. Sleight, and J. L. Gillson, Inorganic Chemistry **8**, 841 (1969).

45. K. Blaha, P.and Schwarz, G. Madsen, and J. Kvasnicka, D.and Luitz, WIEN2k, An Augmented Plane Wave + Local Orbitals Program for Calculating Crystal Properties (Karlheinz Schwarz, Tech. Universität Wien, Austria). (2001).

46. H. J. Monkhorst and J. D. Pack, Phys. Rev. B **13**, 5188 (1976).

47. D. Riegel, K. D. Gross, and M. Luszik-Bhadra, Phys. Rev. Lett. **59**, 1244 (1987).

48. E. Wigner, Nachr. Ges. Wiss. Goett. Math-Phys, (1927).

49. J Behler, B Delley, S Lorenz, K Reuter, and M Scheffler, Phys. Rev. Lett. **94**, 036104 (2005).

50. V. K. Yachandra, K. Sauer, and M. P. Klein, Chemical Reviews **96**, 2927 (1996).

CHAPTER 4

Surface magnetism of transition metal doped RuO_2 (110) and its role in the electrolysis of water

According to experimental studies, replacing part of the ruthenium with other transition metals has an influence on the oxygen evolution activity (OEA) of RuO_2(110)-surface-based anodes. In this chapter we show correlations between the experimental OEA of tungsten, nickel and iridium doped RuO_2(110)-surface-based anodes and the modification of the surface magnetism due to dopants by using first-principle calculations. We also perform Nudged Elastic Band (NEB) calculations to discuss the effect of the surface magnetism in the adsorption process of oxygen molecules on surfaces.

4.1 Introduction

In Chapter 3 we show that, according to first-principle calculations, the RuO_2 (110) surface is magnetic.[2] In the same chapter we address the importance of the magnetic surface for the production of magnetic oxygen molecules out of non-magnetic water. We propose that having a magnetic surface is one of its key properties which makes RuO_2 the best anode for electrolysis of water.

The energy loss in electrolysis is not negligible even for the best anodes like RuO_2. That is why several attempts have been reported to improve the efficiency of RuO_2 by doping with Ti[3], Ni[4], W[5], Sn[6], Ce[7], Ir[8] and Co.[9] Among them Ni, W and Co enhance however, Ir diminishes the OEA of the anode.

The aim of this chapter is to discuss the correlations between the surface magnetism of transition metal doped RuO_2 (110) surfaces and their experimental OEA. At first, we investigate the surface magnetism of doped RuO_2 (110) surfaces. Then, we explore the magnetic moments of the terminal oxygen atoms for each transition metal doped RuO_2 (110) surface. Finally, we discuss the effect of the surface magnetism on the oxygen molecule-surface interactions.

4.2 Calculation Details

All calculations were carried out in the framework of density functional theory (DFT)[10,11] using the first-principles computation code “Vienna ab initio simulation program” (VASP)[12,13] and the projector augmented wave method (PAW).[14,15] The generalized gradient approximation (GGA) by Perdew, Burke and Ernzerhof (PBE)[16] was employed for the exchange and correlation energy terms. The electronic wave functions were sampled on a gamma centered $12 \times 6 \times 1$ for the 1×1 and $6 \times 6 \times 1$ k-mesh for the 2×1 surface unit cells. The cutoff energy of the wave functions was 500 eV. The optimized bulk RuO_2 lattice parameters of $a = 4.52$ and $c = 3.12$ Å are used. For the 1×1 slab, a $3.12 \times 6.39 \times 25.00$ Å^3 and for the 2×1 slab, a $6.24 \times 6.39 \times 25.00$ Å^3 unit cell is used. Both slabs consist of 11 atomic layers and there is ~ 12 Å vacuum between the slabs and their periodic images. The structures are relaxed until the forces on the atoms are smaller than 0.03 eV/Å.

4.3 Transition metal doped RuO_2 (110) surface

As discussed previously, experimental work show that doping with Ni, Co and W enhances, however Ir decreases the OEA of the RuO_2(110)-surface-based anodes. In order to investigate this trend we replace part of the ruthenium in 1×1 and 2×1 RuO_2 (110) surfaces with W, Ni and Ir and analyze their electronic structure. Here we report

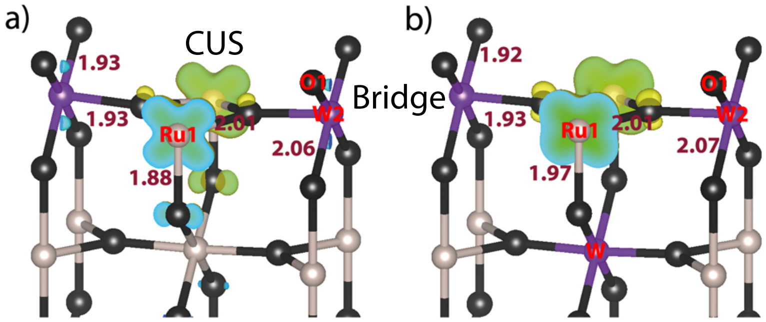

Figure 4.1: Spin density plots of the most stable configurations of single and two tungsten atom doped 1×1 RuO_2 (110) slabs. The numbers are the bond lengths between the metal and the oxygen atoms (in Angstroms). CUS and the bridge site of the surfaces are shown in the figure.

the configurations which are energetically the most stable. The total energies and the magnetic moments of the surface atoms for the other configurations are reported in the appendix. As expected, doping transition metals changes the surface structure slightly so the bond lengths are shown in the figures.

4.3.1 Tungsten doped RuO_2 (110) surface

Tungsten is a 5d element which has the $5d^4$ $6s^2$ valence configuration (Ru: $4d^7$ $5s^1$). Its oxides do not show magnetism. Figure 4.1 shows the most stable configurations of the single (a) and two (b) W atoms doped 1×1 RuO_2 (110) surface. According to the calculations, the single W case has its lowest energy when W occupies the bridge site of the slab. For the case of 2 W, the slab has its lowest energy when one of the W occupies the first layer bridge and the other W occupies the position which is in the second layer under the coordinately unsaturated site (CUS). CUS is the position of the fivefold coordinated metal atom on the surface, its position is shown in Figure 4.1. As expected, doping with W modifies the surface magnetism: W itself has no magnetic moment but the local magnetic moment at the CUS enhances for both cases. The local magnetic moments of the surface atoms are listed in Table 4.1.

Doping W into the 2×1 surface has similar consequences: the system has its lowest energy when W occupies the bridge site (Figure 4.2). W has no magnetic moment, however the moments of the Ru1 and Ru2 atoms increase compared to the bare surface. Doping W into the 2×1 surface has a larger effect on the surface magnetism: the local moments of the atoms at the CUS of the 2×1 surface increase more compared with the 1×1 surface. The local magnetic moments are listed in Table 4.2.

Table 4.1: The local magnetic moments of the surface atoms corresponding to the configurations shown in Figure 4.1.

	Magnetic Moment (μ_B)			
	Ru1	Ru2	W2	O1
Bare Surface	-0.18	0.62	—	0.19
a	0.22	—	-0.07	0.00
b	0.33	—	0.00	0.00

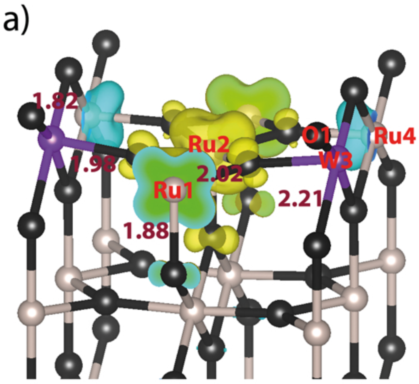

Figure 4.2: Spin density plot of the most stable configuration of single tungsten atom doped 2×1 RuO_2 (110) slab. The numbers are the bond lengths between the metal and the oxygen atoms (in Angstroms).

4.3.2 Nickel doped RuO_2 (110) surface

Ni is a 3d element which has the $3d^8$ $4s^2$ valence configuration. Its oxides usually show magnetic behavior because of the localized 3d states. Figure 4.3 shows the most stable configurations of single (a) and two (b) Ni atoms doped 1×1 RuO_2 (110) surfaces. The single Ni doped case has its lowest energy when Ni occupies the CUS of the surface. For the 2 Ni case, the minimum energy is obtained when one of the Ni atom occupies the CUS and the other occupies the position which is in the second layer under the surface bridge site. As expected, Ni enhances the surface magnetism for both cases especially at the CUS of the slab. The magnetic moments of the atoms are listed in Table 4.3.

The same behavior is observed for the 2×1 surface. The slab has its lowest energy when Ni occupies the CUS of the surface (Figure 4.4). For all Ni doped cases, the Ni atom at the surface carries a 1 μ_B local magnetic moment. This is rather interesting because the Ni atom carries 0.62 μ_B in bulk and 2 μ_B in its oxide. A 1 μ_B local magnetic moment is rather unusual. According to our calculations Ni prefers to stay

Table 4.2: The local magnetic moments of the surface atoms corresponding to the configuration shown in Figure 4.2. The positions of Ru3 and Ru4 are shown in the figure.

	Magnetic Moment (μ_B)					
	Ru1	Ru2	Ru3	Ru4	W3	O1
Bare Surface	-0.18	-0.18	0.62	0.62	—	0.19
a	0.38	0.40	—	-0.19	0.01	0.00

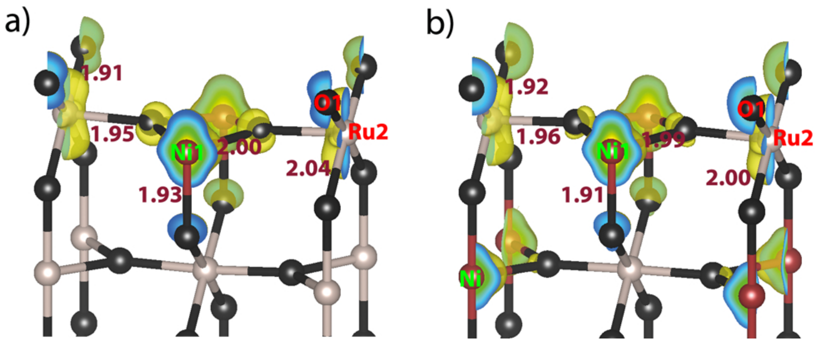

Figure 4.3: Spin density plots of the most stable configurations of single and two nickel atom doped 1×1 RuO$_2$ (110) slabs. The numbers are the bond lengths between the metal and the oxygen atoms (in Angstroms).

at the CUS of the slab, contrary to W.

4.3.3 Iridium doped RuO$_2$ (110) surface

Ir is a 5d element which has the 5d^7 6s^2 valence configuration. Its oxides do not show magnetism, like W. Figure 4.5 shows the most stable configurations of the single (a) and two (b) Ir atoms doped 1×1 RuO$_2$ (110) surfaces. Similar to the W case, the single Ir case has its lowest energy when Ir occupies the bridge site of the surface.

Table 4.3: The local magnetic moments of the surface atoms corresponding to the configurations shown in Figure 4.3.

	Magnetic Moment (μ_B)			
	Ru1	Ru2	Ni1	O1
Bare Surface	-0.18	0.62	—	0.19
a	—	0.36	0.98	0.14
b	—	0.48	0.99	0.25

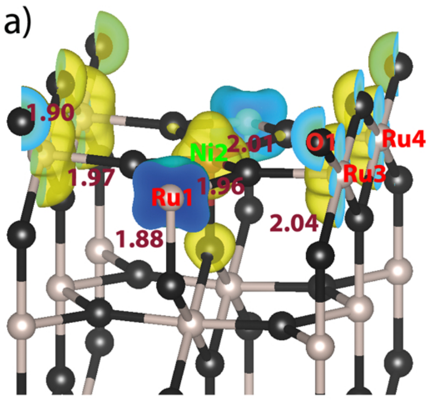

Figure 4.4: Spin density plot of the most stable configuration of single nickel atom doped 2×1 RuO_2 (110) slab. The numbers are the bond lengths between the metal and the oxygen atoms (in Angstroms).

Table 4.4: The local magnetic moments of the surface atoms corresponding to the configurations shown in Figure 4.4.

	Magnetic Moment (μ_B)					
	Ru1	Ru2	Ru3	Ru4	Ni2	O1
Bare Surface	-0.18	-0.18	0.62	0.62	—	0.19
a	-0.54	—	0.60	0.60	1.08	0.20

Unlike the W and Ni cases, the 2 Ir doped surface has its lowest energy when one of the Ir atoms stays at the bridge site and the other one stays in the position under the bridge site (Figure 4.5b) . We observe that doping Ir into the 1×1 RuO_2 (110) slab reduces the surface magnetism drastically.

The Ir doped 2×1 slab has its lowest energy when Ir is present in the second layer of the slab under the surface bridge site (Figure 4.6). Doping a single Ir atom into 2×1 slab has almost no effect on the surface magnetism.

4.3.4 Magnetic properties of terminal oxygen atoms on the transition metal doped RuO_2 (110) surface

According to the experimental reaction mechanism, a surface oxygen coupling step ($O + O \rightarrow O_2$) is the last step of the electrolysis of water on the RuO_2 (110) surface. Therefore, the magnetic properties of the terminal oxygen atoms are important to investigate.

We use the most stable configurations of the transition metal doped 2×1 surfaces and adsorb two oxygen atoms at the CUS of the surfaces (Figure 4.7). The magnetic

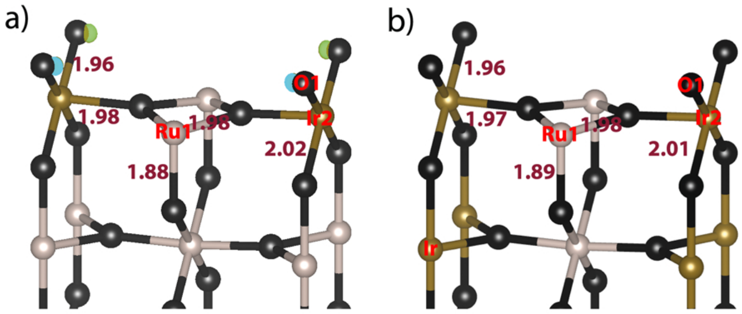

Figure 4.5: Spin density plots of the most stable configurations of single and two iridium atom doped 1×1 RuO$_2$ (110) slabs. The numbers are the bond lengths between the metal and the oxygen atoms (in Angstroms).

Table 4.5: The local magnetic moments of the surface atoms corresponding to the configurations shown in Figure 4.5.

	Magnetic Moment (μ_B)			
	Ru1	Ru2	Ir2	O1
Bare Surface	-0.18	0.62	—	0.19
a	-0.05	—	0.03	0.02
b	-0.05	—	0.01	0.01

moments of the terminal oxygen atoms are listed in Table 4.7. According to our calculations, the Ot1 and the Ot2 atoms on the bare 2×1 RuO$_2$ (110) surface carry 0.1 μ_B local magnetic moments. The magnetic moments of these atoms slightly change for the W and Ir doped cases. The terminal oxygen atom which is adsorbed on the Ni atom carries 0.9 μ_B magnetic moment. This can be very important for the spin conservation at the last step of the water electrolysis on the Ni doped 2×1 RuO$_2$ (110) surface.

Table 4.6: The local magnetic moments of the surface atoms corresponding to the configurations shown in Figure 4.6.

	Magnetic Moment (μ_B)				
	Ru1	Ru2	Ru3	Ru4	O1
Bare Surface	-0.18	-0.18	0.62	0.62	0.19
a	-0.16	-0.16	0.62	0.62	0.20

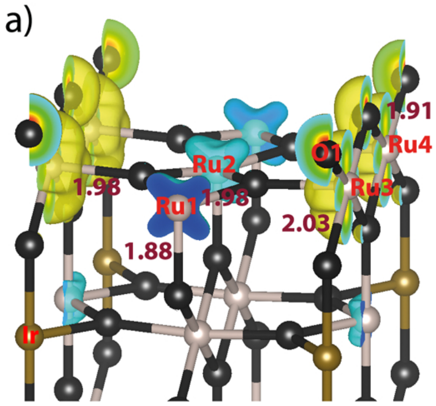

Figure 4.6: Spin density plot of the most stable configuration of single iridium atom doped 2×1 RuO_2 (110) slab. The numbers are the bond lengths between the metal and the oxygen atoms (in Angstroms).

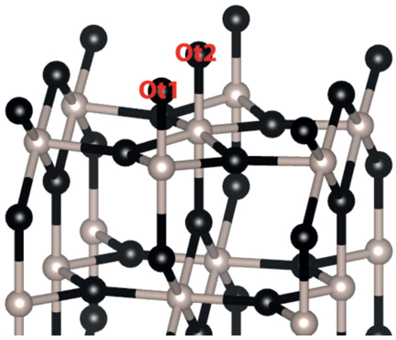

Figure 4.7: Optimized geometric structure of oxygen covered RuO_2 (110) surface. The terminal oxygen atoms are shown as Ot1 and Ot2.

4.4 Effect of surface magnetism on oxygen molecule-surface interactions

The importance of angular momentum conservation in electrolysis can be generalized to other oxygen molecule-surface interactions. This phenomenon is discussed on the interaction of the Si(001) surface with an oxygen molecule by Kato et al.[17] In this reaction, the final configuration is a spin singlet so the oxygen molecule is the only entity which is magnetic. Kato et al. conclude that the oxygen molecule should change its spin state from the magnetic triplet ground state to a non-magnetic singlet excited state to react with the singlet Si(001) surface. This change is responsible for the narrow channel of barrierless oxidation channel of the Si(001) surface. A similar kind of conclusion is reached for the explanation of the low sticking probability of an oxygen molecule on the Al(111) surface.[18–20] This statement is valid for the oxygen molecule-surface interactions in general. It is more critical when the metal has a low

Table 4.7: The local magnetic moments of terminal oxygen atoms on transition metal doped 2×1 RuO_2 (110) surface shown in Figure 4.7

	Magnetic Moment (μ_B)	
	Ot1	Ot2
2×1 (110)	0.10	0.10
W doped surface	0.08	0.07
Ni doped surface	-0.02	0.90
Ir doped surface	0.10	0.11

density of states at the Fermi level.[18–20]

In the literature there is no investigation on the effect of the surface magnetism on the oxygen molecule-surface interactions. That is why in this section we will analyze the effect of the surface magnetism on this interaction.

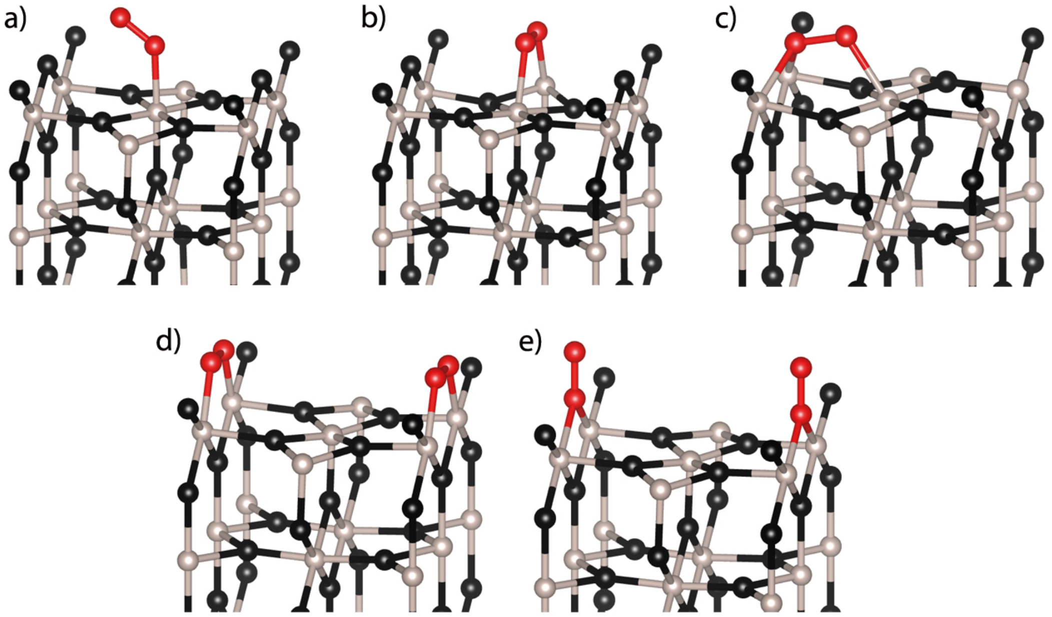

Figure 4.8: Several adsorption configurations of oxygen molecule on the RuO_2 (110) surface. The adsorbed oxygen molecules are shown in red and the magnetic moments of them can be seen in Table 4.8.

Initially, we investigate the magnetic moments of oxygen species on the RuO_2 (110) surface which are shown in Figure 4.8. The corresponding magnetic moments are listed in Table 4.8. The atomic configuration of oxygen species on the RuO_2 (110) surface has been analyzed previously.[21] We use the reported structures as initial

Table 4.8: The local magnetic moments of O_2 on RuO_2 (110) surface shown in Figure 4.8

	Case a	Case b	Case c	Case d	Case e
Magnetic moment of O_2 (μ_B)	0.94	0.23	0.00	0.00	0.26

guess and optimized them by using spin-polarized DFT and investigate the magnetic moments of the adsorbed oxygen species. As can be seen from Table 4.8, there are some adsorbed states in which the oxygen molecule carries a local magnetic moment. When the oxygen molecule is adsorbed perpendicular to the surface at the CUS (Figure 4.8a), it carries 1 μ_B magnetic moment. The oxygen molecule carries 0.23 μ_B when it is adsorbed parallel at the CUS (Figure 4.8b) and 0.26 μ_B when it is adsorbed perpendicular at the bridge site (Figure 4.8e). For the other configurations the oxygen species do not carry magnetization (Figure 4.8c and d).

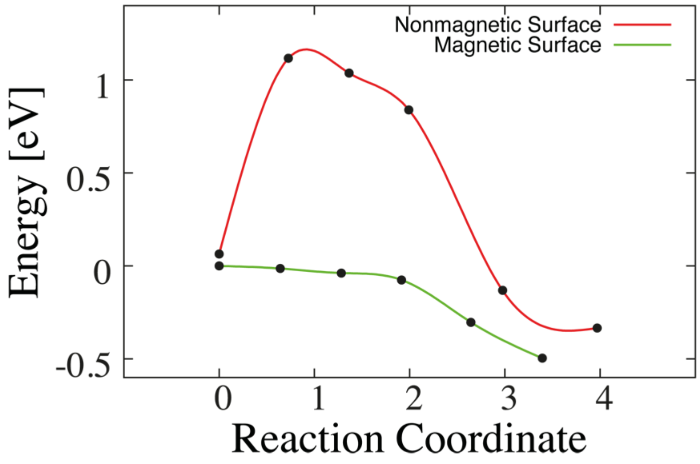

Figure 4.9: NEB calculation for adsorption of O_2 on magnetic and non-magnetic surfaces.

We performed two sets of NEB[22] calculations in order to investigate the effect of the surface magnetism on oxygen molecule-surface interactions. NEB is a method which finds the minimum energy paths between the products and the reactants in a chemical reaction. We used the configuration shown in Figure 4.8a as the adsorption state of the oxygen molecule.

At first, we calculated the total energies of magnetic and non-magnetic RuO_2 (110) surfaces with a magnetic oxygen molecule more than 5 Å away from them. The first two data points at the left of Figure 4.9 correspond to these energies. Then we started our NEB calculations. In the first set of NEB calculation, we do not consider the surface magnetism. So to have a reaction between oxygen molecule and the surface, the oxygen molecule should change its spin state from the magnetic triplet ground state to a non-magnetic excited state. The minimum energy path of this reaction is shown in Figure 4.9 in red. The barrier caused by the angular momentum conservation can be seen clearly. In the second calculation the oxygen molecule does not need to change its spin state because the magnetic RuO_2 (110) surface provides a mechanism to react with the triplet oxygen molecule while conserving angular momentum. The minimum energy path of these reactions is shown in Figure 4.9 in green. As can be seen from the figure, a barrier is not observed in this case. These results could be the explanation of the high initial sticking probability of oxygen molecules on the RuO_2 (110) surface, which is 0.7 experimentally.[1]

The interaction between oxygen molecule and metal surface is important also for other technological applications such as fuel cells.[23] Adsorption of oxygen molecules on the platinum surfaces is suggested as the rate limiting step of the oxygen reduction in fuel cells. This reaction does not include charge transfer.[24] A discussion similar to ours on RuO_2 is relevant here: since the platinum surface is not magnetic the oxygen molecule-surface interaction exhibits a high activation barrier because of the conservation of angular momentum. Therefore, we suggest that doping a magnetic entity inside the platinum electrode may increase the activity of fuel cells.

4.5 Conclusions

A paramagnetic anode can provide a mechanism to overcome any spin angular momentum restriction along the reaction path of the electrolysis of water. For example, the last step of the electrolysis, where two terminal oxygen atom couple and create an oxygen molecule on the RuO_2 (110) surface is not the rate limiting step. Since the RuO_2 (110) surface carries magnetization this is an expected observation.

In this chapter we dope Ni, W and Ir into several sites of 1×1 and 2×1 RuO_2 (110) surfaces. Without proposing a detailed analysis here, we show a correlation between the surface magnetism of the transition metal doped RuO_2 (110) surfaces and their experimental OEA. In experiments it is observed that W and Ni doping are enhancing, whereas, Ir is reducing the OEA of the anode. In our calculations we observe that W and Ni doping enhance, whereas, Ir reduces the surface magnetism especially at the CUS of the surfaces.

We also investigate the magnetic properties of terminal oxygen atoms of bare and transition metal doped 2×1 RuO_2 (110) surfaces. We observe that the magnetic moments of terminal oxygen atoms do not change much for the W and Ir doped surfaces compared with the bare slab. However, the terminal oxygen atom carries a 0.9 μ_B magnetic moment for the Ni doped slab.

We show that the surface magnetism could play a role in the adsorption process of oxygen molecules on metal surfaces. This discussion should also be valid for the desorption of oxygen molecules from a metal surface. The very low desorption temperature of oxygen molecules from RuO_2 (110) surfaces[25] could be the consequence of having a magnetic surface.

Bibliography

1. A. Böttcher and H. Niehus, Phys. Rev. B **60**, 14396 (1999).
2. E. Torun, C. M. Fang, G. A. de Wijs, and R. A. de Groot, The Journal of Physical Chemistry C **117**, 6353 (2013).
3. L. A. De Farìa and S. Trasatti, Journal of Electroanalytical Chemistry **340**, 145 (1992).
4. K. Macounová, J. Jirkovský, M. V. Makarova, J. Franc, and P. Krtil, Journal of Solid State Electrochemistry **13**, 959 (2009).
5. M. W. Shafer and R. A. de Groot, IBM Technical Disclosure Bulletin **21**, 5070 (1979).
6. J. Gaudet, A. C. Tavares, S. Trasatti, and D. Guay, Chemistry of Materials **17** 1570 (2005).
7. L. A. De Farìa, J. F. C. Boodts, and S. Trasatti, Electrochimica Acta **37**, 2511 (1992).
8. M. E. G. Lyons and S. Floquet, Phys. Chem. Chem. Phys. **13**, 5314 (2011).
9. J. Jirkovskỳ, M. Makarova, and P. Krtil, Electrochemistry Communications **8**, 1417 (2006).
10. P. Hohenberg and W. Kohn, Phys. Rev. **136**, B864 (1964).
11. W. Kohn and L. J. Sham, Phys. Rev. **140**, A1133 (1965).
12. G. Kresse and J. Furthmüller, Phys. Rev. B **54**, 11169 (1996).
13. G. Kresse and J. Furthmüller, Comput. Mat. Sci. **6**, 15 (1996).
14. P. E. Blöchl, Phys. Rev. B **50**, 17953 (1994).
15. G. Kresse and D. Joubert, Phys. Rev. B **59**, 1758 (1999).
16. J. P. Perdew, K. Burke, and M. Ernzerhof, Phys. Rev. Lett. **77**, 3865 (1996).
17. K. Kato, T. Uda, and K. Terakura, Phys. Rev. Lett. **80**, 2000 (1998).
18. J. Behler, B. Delley, S. Lorenz, K. Reuter, and M. Scheffler, Phys. Rev. Lett.

94, 036104 (2005).

19. J. Behler, K. Reuter, and M. Scheffler, Phys. Rev. Lett. **96**, 079802 (2006).
20. C. Carbogno, J. Behler, A. Gross, and K. Reuter, Phys. Rev. Lett. **101**, 096104 (2008).
21. H. Wang, W. F. Schneider, and D. Schmidt, The Journal of Physical Chemistry C **113**, 15266 (2009).
22. G. Mills, H. Jonsson, and G. K. Schenter, Surface Science **324**, 305 (1995).
23. N. Ramaswamy and S. Mukerjee, Advances in Physical Chemistry **2012**, 491604 (2012).
24. E. Yeager, M. Razaq, D. Gervasio, A Razaq, and D. Tryk, Proceedings of the Electrochemical Society **92**, 440 (1992).
25. Y. D. Kim, A. P. Seitsonen, S. Wendt, J. Wang, C. Fan, K. Jacobi, H. Over, and G. Ertl, The Journal of Physical Chemistry B **105**, 3752 (2001).

CHAPTER 5

Origin of Weak Magnetism in Compounds with Cubic Laves Structure

The origin of the weak itinerant magnetism in materials like $TiBe_2$ and $ZrZn_2$ is investigated. The huge peak in the density of states at the Fermi energy is attributed to a special symmetry of the C15 structure: no crystal field splitting of the *d* levels occurs in the case of coordination by spherical ligands. Crystal field splitting is also investigated for the *f* orbitals in C15 structures like $PuZn_2$ and $ThMg_2$. It is observed that the situation in *f* levels is more complicated than the *d* levels because the characteristics of the crystal field splitting in *f* levels cannot be described only with the local point symmetry of the compounds.

A manuscript based on this chapter has been submitted for publication by E. Torun, A. Janner and R. A. de Groot.

5.1 Introduction

The description of common magnetic materials is based on local magnetic moments that are ordered at zero temperature. With increasing temperature the ordering of the moments is reduced until, at the critical temperature, the net magnetization vanishes. The size of the moments is independent of temperature - at least in good approximation. Weak, itinerant magnetism is quite distinct: here the magnetic moments disappear at the Curie temperature. An overwhelming majority of the magnetic materials falls in the first category, which is usually called strong magnetism (strong refers to the robustness of the magnetic moments with respect to temperature and disorder).

The chemical compositions of weak, itinerant and strong magnetic materials are also quite distinct. Strong magnets contain elements from the right hand side of the periodic table where a certain angular momentum appears first: the 2p, 3d and 4f series. The absence of such an angular momentum in the electron-core favors localization of the corresponding valence states. This is because the requirement of orthogonality to the core states is satisfied already by the angular dependent part of the Schrödinger equation. Hence, there is no constraint on the radial Schrödinger equation which determines the degree of localization. A constraint increases the energy and thus induces delocalization. This is the case, for example, in 3p, 4d and 5f materials.

The presence of magnetic moments in a solid competes with chemical bonding. This is best exemplified by the simplest case, Mn^{2+}. In the high spin case the majority spin d shell is completely filled, while the minority d shell is completely empty, hence, the d electrons do not participate in chemical bonding. In the non-magnetic case the states for the two spin directions are degenerate and consequently the half filled d shell can contribute maximally to the chemical bonding. Heating a weak magnet above its Curie-temperature releases degrees of freedom for chemical bonding.

Two phenomena require the combination of both strong and weak magnetism in one compound, but in a distinct way: the invar effect[1–3] and the giant magneto caloric effect.[4] Invar materials show negligible thermal expansion over a certain temperature range. The explanation is based on the existence of a phase with a relatively low volume and low magnetic moment and a phase with higher volume and higher magnetic moments, the latter being slightly lower in energy. Thermal excitations to the weaker magnetic phase increase the strength of the chemical bonding and this compensates the usual thermal lattice expansion over a certain temperature range.

The origin of the giant magneto caloric effect is the coexistence of weak itinerant and strong magnetism in alternate atomic layers in one material. The degrees of freedom for chemical bonding released in the weakly magnetic layers in the hexagonal structure induce a crystallographic phase-transition at the Curie temperature that is responsible for the large caloric effect. The strongly magnetic layers are responsible for the relatively high Curie temperatures (room temperature and above).[4]

Examples of the weak itinerant magnets are compounds like $TiBe_2$ and $ZrZn_2$ with chemical compositions that are in sharp contrast with that of strong magnets: titanium and zirconium are positioned at the left side of the transition metal series and the latter one is not even a 3d element. Zinc and beryllium are main-group elements (the latter one has no 2p electrons). Consequently none of the constituting elements is itself magnetic as a solid.

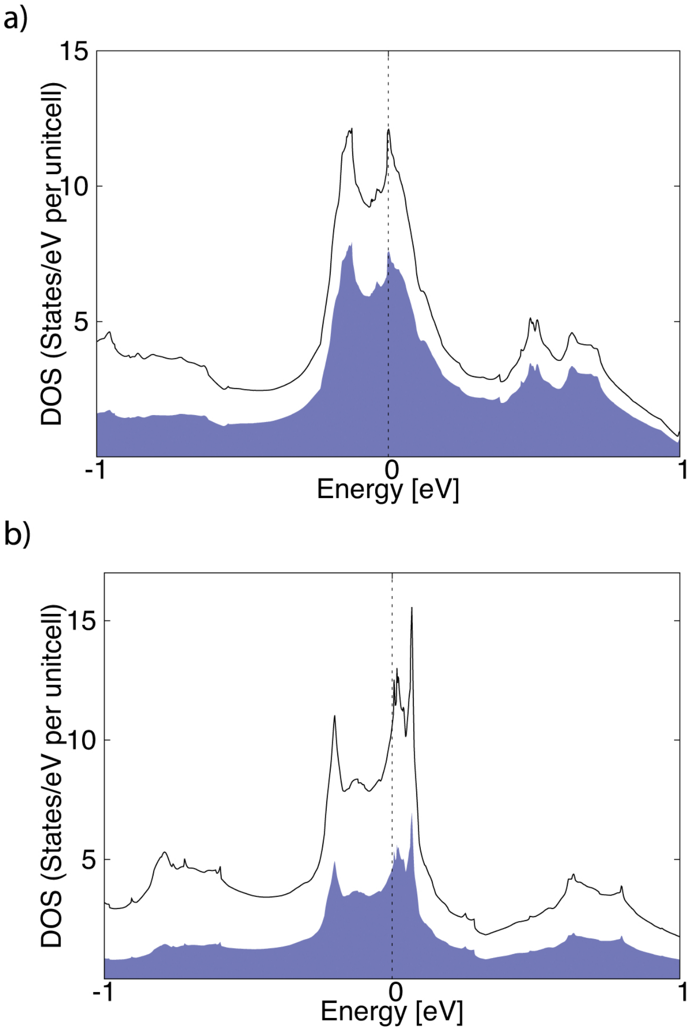

Figure 5.1: The total and the partial DOS of a) $TiBe_2$ and b) $ZrZn_2$. The partial DOS of the *d* orbitals is shown in blue. The Fermi level is at 0 eV.

The ferromagnetism in $ZrZn_2$ was first described by Matthias and Bozorth[5], who reported a magnetic moment of 0.13 μ_B per molecule and a Curie temperature of

35 K. Mattocks and Melville also reported very small comparable magnetic moments.[6] Measurements of the specific heat, magnetic susceptibility and nuclear magnetic resonance by Knapp, Fradin and Culber[7] determined the origin of the ferromagnetism: the presence of a sharp ($\sim$ 0.05 eV half width), high (5.4 states/eV) peak in the density of states (DOS) at the Fermi energy. Enz and Matthias[8] discovered that (partial) substitution of CuAl for Zn_2 destroys the magnetism in $ZrZn_2$. The importance of this staggering observation has escaped the attention: CuAl and Zn_2 are iso-electronic and equal in size - why then do they behave so differently here? Band structure calculations confirm the existence of the high, narrow peak at the Fermi energy in the case of $ZrZn_2$, ruling out intrinsic many-body explanations.[9,10]

$TiBe_2$ is iso-electronic and iso-structural with $ZrZn_2$. It was found to be an itinerant antiferromagnet.[11,12] Subsequent work describes it as a strongly enhanced paramagnet that becomes ferromagnetic by partial substitution of beryllium by copper.[13,14] This reduction of the Néel temperature and subsequent increase in Curie temperature is a continuous process as function of the copper content. But partial substitution of beryllium by gallium has an unexpected effect: it leads to a strong reduction of the DOS at the Fermi energy.[15]

The Stoner criterion for the occurrence of magnetism is valid independent of the type of magnetism and consequently weak, itinerant magnets also show high density of states at the Fermi energy. Since the chemical composition of the C15 structure is clearly not the origin of the magnetism, the explanation must be contained in the crystal structure. In many cases magnetism is suppressed by the application of pressure. Also a large majority of the elements of the periodic table are magnetic in the form of isolated atoms. So a possible explanation could be that the crystal structure of the compounds showing weak itinerant magnetism is a loosely packed, open structure. But exactly the opposite is the case: the volume of $ZrZn_2$, for example, is 6 % less than the sum of the volumes of the constituting elements that all crystallize in the hexagonal close packed structure.

Electronic structure calculations do show a high DOS at the Fermi energy for $ZrZn_2$ and $TiBe_2$ so the possible explanation for the occurrence of weak itinerant magnetisms could only be in a special symmetry of the crystal structure. The identification of this aspect of the C15 structure is the subject of this chapter. Preliminary work about this topic has been done by A. Janner and R. A. de Groot. In this chapter, we show that the C15 structure has the unique property that it shows a vanishingly small crystal field splitting (CFS) for d electrons provided that the coordinating atoms have a spherical charge density. This chapter is organized as follows: at first we investigate how CFS changes from octahedral to tetrahedral symmetry via C15 structure on a continuous path by taking into account the effect of only the nearest neighbor atoms. Then, we include the effect of the complete lattice and compare these two cases. As an extension of this work we apply a similar approach for the *f* levels in the C15 structure and compare the results with the *d* levels.

5.2 Calculation Details

Electronic structure calculations were carried out in the framework of density functional theory (DFT)[18,19] using the first-principles computation code "Vienna ab initio simulation program" (VASP)[20,21] and the projector augmented wave method (PAW).[22,23] The generalized gradient approximation (GGA) by Perdew, Burke and Ernzerhof (PBE)[24] was employed for the exchange and correlation energy terms. The cutoff energy of the wave functions was 500 eV. The experimental lattice parameters of the compounds are used in the calculations, a table which contains the lattice parameters of the compounds is provided in the appendix.

5.3 Crystal Field Splitting of the d Orbitals in the Cubic Laves Structure

The space group of $TiBe_2$ and $ZrZn_2$, which crystallize in the C15 structure, is Fd3m (# 227); the transition metals form a diamond structure (Wyckoff position 8a), the main-groups atoms occupy Wyckoff position 16d. This leads to a coordination of the transition metal by 12 nearest neighbor main group atoms forming equidistant chains along the [110] direction. The second coordination sphere consists of four transition metals.

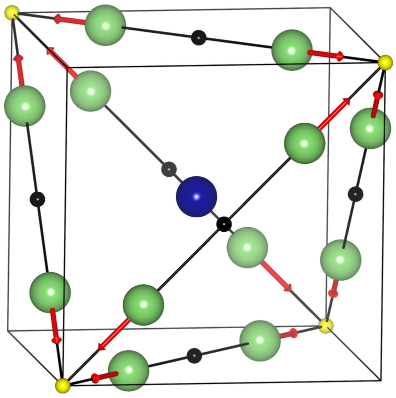

Figure 5.2: The positions of nearest neighbor atoms (green) relative to the central atom (blue) in the C15 structure. The black dots are the positions of octahedral symmetry. The continuous path from octahedral to tetrahedral symmetry starts from the black dot (octahedral position) and runs *via* the C15 structure to the yellow point (tetrahedral symmetry).

The total DOS' of $TiBe_2$, $ZrZn_2$ and the partial DOS' of the *d* orbitals are shown in Figure 5.1. The peaks at the Fermi level are evident in the figures. The *d* levels are mostly localized around the Fermi level. The narrow splitting in the *d* orbitals leads to a peak at the Fermi level for both systems. Consequently, this high DOS is responsible for the magnetic property of both systems *via* the Stoner criterion of magnetism.

In crystal field theory (CFT) the influence of the lattice on the d (or f) orbitals of the central atom is taken into account by considering the influence of nearest neighbors by replacing them by point charges. The effect of point charges give rise a Coulomb potential which is called crystal field potential (CFP). Using the perturbation theory formalism and taking the CFP as the perturbative potential the secular matrix (the size of the secular determinant is 5×5 and 7×7 for d and f orbitals, respectively) should be set up and eigenvalues of the secular determinant should be obtained. The energy splitting in the energy of the orbitals corresponds to the CFS for the d and f levels for the particular symmetry. This simple model represents the zero order approach of understanding the magnetic and optical properties of compounds and we apply it in an adapted form here.

As a thought experiment we investigate a continuous variation from an octahedral coodinaated central atom via the C15 structure to a tetrahedral coordination. This can be accomplished by describing the ligands in the Wyckoff position 32e. The continuous path from octahedral to tetrahedral symmetry starts from the black dot (octahedral position) via C15 structure to yellow point (tetrahedral symmetry) as shown in Figure 5.2. In one direction two atoms will merge leading to an octahedral coordination of the central atom. In the opposite direction, three atoms will merge to form a tetrahedral coordination. The positions of nearest neighbor atoms in terms of the "*u*" parameter are given in Table B.1 and all the missing derivations throughout the chapter are provided in the appendix.

In order to investigate how the CFS changes from octahedral (where $u = 0$) to tetrahedral (where u=1) symmetry, the CFP is needed to be written in terms of the "*u*" parameter. As discussed in the introductory chapter the CFP is

$$V(x, y, z) = \sum_{i=1}^{n} \frac{ez_i}{r_{ij}}, \tag{5.1}$$

where

$$\frac{1}{r_{ij}} = \sum_{n=0}^{\infty} \sum_{m=-n}^{n} \frac{4\pi}{2n+1} \frac{r_<^n}{r_>^{n+1}} Y_{nj}^m Y_{ni}^{m^*}. \tag{5.2}$$

Our main task is to write $1/r_{ij}$ in terms of the "*u*" parameter. After this procedure the CFP can be written as follows

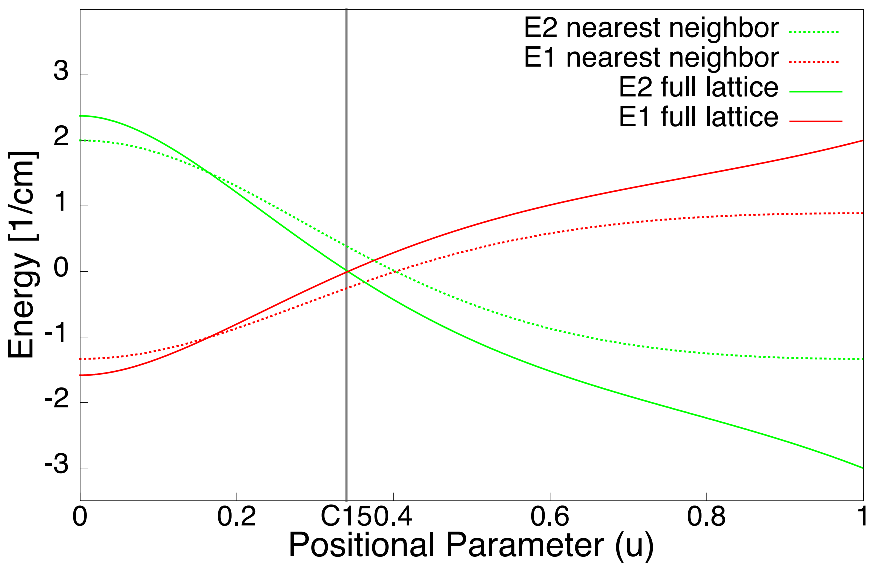

Figure 5.3: Evolution of energies of triplet (E1) and doublet (E2) states from octahedral to tetrahedral symmetry *via* the C15 structure. The y-axis is the energy and the x-axis is the positional parameter (u) of non-transition metal atoms. See Figure 5.2

.

$$\begin{aligned} V(u) =& \frac{1}{a} + \frac{42\sqrt{\pi}}{9}\frac{ze\overline{r^4}}{a^5}Y_4^0(\theta,\phi)\left(\frac{-u^4-6u^2+1}{(2u^2+1)^2}\right) \\ &+ \sqrt{\frac{70\pi}{9}}\frac{ze\overline{r^4}}{a^5}(Y_4^4(\theta,\phi)+Y_4^{-4}(\theta,\phi))\left(\frac{-u^4-6u^2+1}{(2u^2+1)^2}\right). \end{aligned} \tag{5.3}$$

The first part of Equation 5.3 corresponds to an equal shift for all the five *d* orbitals where “a” is the distance between the ligand and the central atom. Since it has no contribution to the splitting of the *d* levels, it is not necessary to take it into account for the discussion here. Using this potential the secular determinant which is given in Equation 1.18 of the introduction can be constructed. It is:

$$\begin{array}{c|ccccc|} & (2) & (1) & (0) & (-1) & (-2) \\ (2) & D-E & 0 & 0 & 0 & 5D \\ (1) & 0 & -4D-E & 0 & 0 & 0 \\ (0) & 0 & 0 & 6D-E & 0 & 0 \\ (-1) & 0 & 0 & 0 & -4D-E & 0 \\ (-2) & 5D & 0 & 0 & 0 & D-E \end{array} = 0 \tag{5.4}$$

where,

$$D = \frac{1}{3}\frac{ze\overline{r_2^4}}{a^5}\left(\frac{-u^4-6u^2+1}{(2u^2+1)^2}\right). \tag{5.5}$$

The secular matrix shown in Equation 5.4 has two eigenvalues.

$$\begin{aligned} E1 &= \frac{-4}{3}\frac{ze\overline{r^4}}{a^5}\left(\frac{-u^4-6u^2+1}{(2u^2+1)^2}\right), \\ E2 &= \frac{6}{3}\frac{ze\overline{r^4}}{a^5}\left(\frac{-u^4-6u^2+1}{(2u^2+1)^2}\right). \end{aligned} \tag{5.6}$$

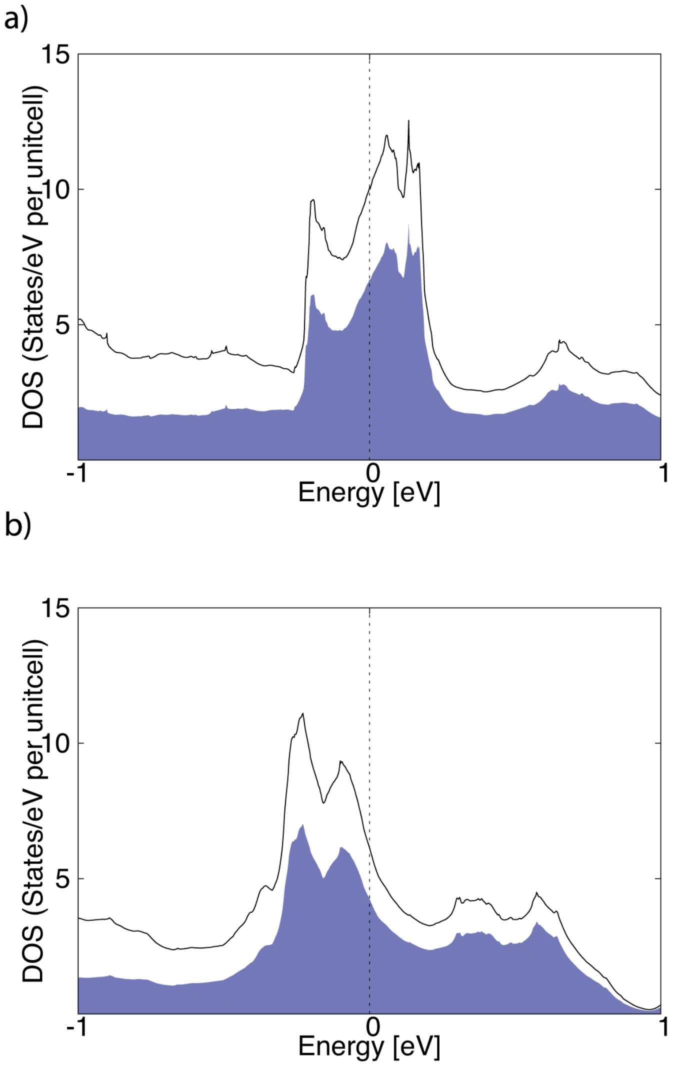

Figure 5.4: The total and the partial DOS of a) $TiBe_{1.5}Cu_{0.5}$ and b) $TiBe_{1.5}Ga_{0.5}$. The partial DOS of the *d* orbitals is shown in blue. The Fermi level is at 0 eV.

Since the ordering of triplet (E1) and doublet (E2) are opposite at the end points of the *u* range, they are degenerate in at least one point along the trajectory. The dotted line in Figure 5.3 shows how the E1 and E2 eigenvalues are evolving from octahedral to tetrahedral symmetry *via* the C15 structure while taking into account only nearest neighbor non-transition metal atoms. The degeneracy in the energy is observed when the positional parameter u is 0.402.

As the next step we include the effect of the complete structure by using a Matlab code. In Figure 5.3 the result of this approach can be seen in solid lines. The degeneracy shifts to 0.34 if the complete lattice is taken into account rather than the nearest neighbors only. This is within 2 % of 1/3, the u value of the C15 structure. This shows that the C15 structure has negligible CFS for the d levels. This is the reason for having a high peak at the Fermi level and consequently the magnetic behaviour of $TiBe_2$ and $ZrZn_2$.

As discussed previously experimental works show that replacing part of the beryllium with copper makes the compound an itinerant ferromagnet[13,14], however, $TiBe_2$ losses its magnetism when part of the beryllium is substituted by gallium.[15] Figure 5.4 shows the total DOS for this two cases. As expected, the high DOS at the Fermi level remains for the case that copper is substituted (Figure 5.4a). However, a reduction in the DOS at the Fermi level is observed for the case that gallium is substituted (Figure 5.4b). The reason is that gallium, unlike copper, does not have spherical charge density.

5.4 Crystal Field Splitting of the f Orbitals in the Cubic Laves Structure

While analyzing the CFS for the f-electron compounds, it is necessary to separate the discussion into two parts; the lanthanide and the actinide series. The reason is that the effect of the crystal field is different for lanthanide and actinide series compounds. In addition, the effect of the crystal field is much smaller in these compounds than in the transition metal compounds.

In the transition metal series the perturbations which remove the degeneracy of the energy levels are in the following order[16,17]

$$e^2/r \sim V_{\mathrm{oct}} > \lambda.L.S > kT. \tag{5.7}$$

The inter-electronic repulsion term (the first term) which is responsible for the splitting of free-ion energies, is of the same order of magnitude as the crystal field that is due to the octahedral symmetry. These two terms are larger than the spin orbit coupling (SOC) and the thermal energy of the d systems at room temperature.

In the actinide series, the magnitude of the crystal field is one order of magnitude smaller than the d systems. And the effects are ordered as follows

$$e^2/r > V_{\mathrm{oct}} \sim \lambda.L.S > kT. \tag{5.8}$$

Here, the effect of the octahedral field is comparable to the SOC and larger than the thermal energy.

The effect of the crystal field in the lanthanide elements is negligible. $\mathrm{V_{oct}}$ is smaller than the SOC and the inter-electronic repulsion. The order is given as

$$\mathrm{e}^2/\mathrm{r} > \lambda.L.S > \mathrm{V_{oct}} \sim k\mathrm{T}. \tag{5.9}$$

The f orbitals in the lanthanide elements are more localized and the outerlying s and p orbitals protect them from perturbing effects. This shielding makes the chemical properties of lanthanide series elements similar to each other[16].

Even though the strength of the crystal field effect in f series compounds is not as substantial as in the d series compounds it is still worth to apply an analytical analysis like we obtained for the d levels. Similar to the approach that we perform for the d levels, we need to write CFP in terms of the "u" parameter. The potential for the case of f levels is

$$\begin{aligned} V(u) =& \frac{1}{a} + \frac{42\sqrt{\pi}}{9}\frac{ze\overline{r^4}}{a^5}Y_4^0(\theta,\phi)\left(\frac{-u^4-6u^2+1}{(2u^2+1)^2}\right) \\ &+\sqrt{\frac{70\pi}{9}}\frac{ze\overline{r^4}}{a^5}(Y_4^4(\theta,\phi)+Y_4^{-4}(\theta,\phi))\left(\frac{-u^4-6u^2+1}{(2u^2+1)^2}\right) \\ &-\frac{3}{13}\sqrt{13\pi}\frac{ze\overline{r^6}}{a^7}Y_6^0(\theta,\phi)\left(\frac{13u^6-75u^4+15u^2-1}{(2u^2+1)^3}\right) \\ -\frac{3}{13}&\sqrt{\frac{91\pi}{2}}\frac{ze\overline{r^6}}{a^7}(Y_6^4(\theta,\phi)+Y_6^{-4}(\theta,\phi))\left(\frac{13u^6-75u^4+15u^2-1}{(2u^2+1)^3}\right). \end{aligned} \tag{5.10}$$

From this we obtain the secular determinant for the f levels and its eigenvalues. We provide the derivations of the matrix and the eigenvalues in the appendix. The secular matrix and the eigenvalues are

$$\begin{array}{c|ccccccc|} & (3) & (2) & (1) & (0) & (-1) & (-2) & (-3) \\ (3) & H_{33}-E & 0 & 0 & 0 & H_{3-1} & 0 & 0 \\ (2) & 0 & H_{22}-E & 0 & 0 & 0 & H_{2-2} & 0 \\ (1) & 0 & 0 & H_{11}-E & 0 & 0 & 0 & H_{1-3} \\ (0) & 0 & 0 & 0 & H_{00}-E & 0 & 0 & 0 \\ (-1) & H_{-13} & 0 & 0 & 0 & H_{-1-1}-E & 0 & 0 \\ (-2) & 0 & H_{-22} & 0 & 0 & 0 & H_{-2-2}-E & 0 \\ (-3) & 0 & 0 & H_{-31} & 0 & 0 & 0 & H_{-3-3}-E \end{array} = 0 \tag{5.11}$$

where

$$
\begin{aligned}
H_{33} = H_{-3-3} &= -\frac{7}{11}A - \frac{5}{286}B, \\
H_{22} = H_{-2-2} &= \frac{49}{33}A + \frac{15}{143}B, \\
H_{11} = H_{-1-1} &= -\frac{7}{33}A - \frac{75}{286}B, \\
H_{00} &= -\frac{14}{11}A - \frac{50}{143}B, \\
H_{3-1} = H_{-13} &= \frac{7}{11}\sqrt{\frac{5}{3}}A + \frac{35\sqrt{15}}{286}B, \\
H_{2-2} = H_{-22} &= -\frac{35}{33}A + \frac{105}{143}B, \\
H_{1-3} = H_{-31} &= \frac{7}{11}\sqrt{\frac{5}{3}}A + \frac{35\sqrt{15}}{286}B.
\end{aligned}
\tag{5.12}
$$

and

$$
\begin{aligned}
A &= \frac{ze\overline{r^4}}{a^5}\left(\frac{-u^4 - 6u^2 + 1}{(2u^2+1)^2}\right), \\
B &= \frac{ze\overline{r^6}}{a^7}\left(\frac{13u^6 - 75u^4 + 15u^2 - 1}{(2u^2+1)^3}\right).
\end{aligned}
\tag{5.13}
$$

The diagonalization of the matrix gives 5 distinct eigenvalues

$$
\begin{aligned}
E1 &= \frac{2}{143}(182A - 45B), \\
E2 &= \frac{14}{11}A - \frac{50}{143}B, \\
E3 &= \frac{2}{429}(91A + 180B), \\
E4 = E5 &= \frac{1}{429}(-182A - 60B + 7\sqrt{2}\sqrt{1352A^2 + 1365AB + 45B^2}), \\
E6 = E7 &= \frac{1}{429}(-182A - 60B + 7\sqrt{2}\sqrt{1352A^2 + 1365AB + 45B^2}).
\end{aligned}
\tag{5.14}
$$

Equation 5.14 and 5.13 show that the CFS for the *f* levels cannot be described by only one parameter unlike the case of the *d* orbitals. This adds an extra complication to the problem. In addition, there is no real information about the size of the constants $ze\overline{r^4}/a^5$ and $ze\overline{r^6}/a^7$.

Figure 5.5 shows the evolution of the energy eigenvalues from octahedral to tetrahedral symmetry with and without full lattice contribution. In order to plot Figure 5.5, as a rough approximation we consider that $ze\overline{r^6}/a^7$ is almost 5 times smaller than $ze\overline{r^4}/a^5$. The dotted line in Figure 5.5 shows the evolution of the eigenvalues from octahedral to tetrahedral symmetry considering only the nearest neighbor atoms.

The solid line represents the case in which the full lattice contribution is taken into account.

It is important to mention that the characteristics of CFS for f levels depends on the ratio between the constants $ze\overline{r^4}/a^5$ and $ze\overline{r^6}/a^7$. For example, if the latter term is negligible compared to the first, we would end up a situation which is identical to the d levels. The degeneracy in the f levels would be at the position which corresponds to the C15 structure almost like in Figure 5.5. Figure 5.6 shows the situation when these two terms are taken equal. It can be seen that the characteristics of the CFS change when the ratio between these two terms changes.[16]

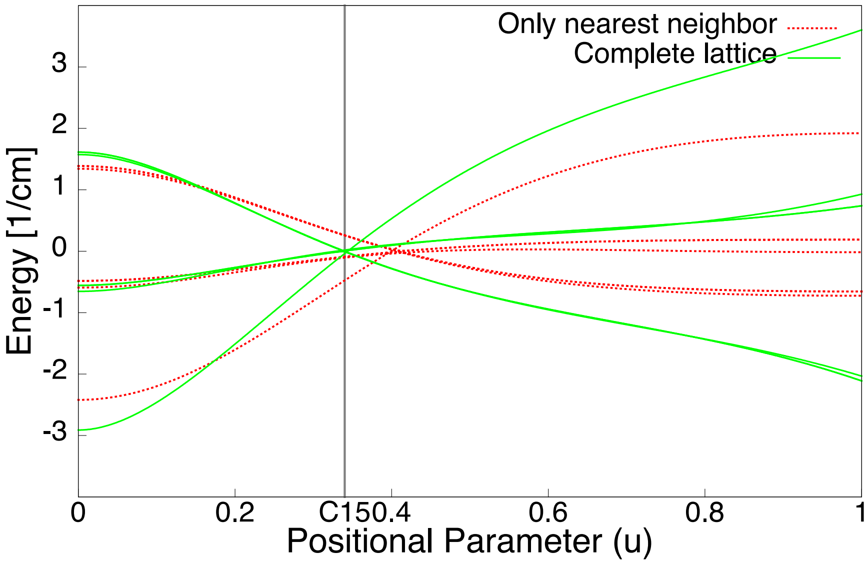

Figure 5.5: Evolution of energy eigenvalues from octahedral to tetrahedral symmetry via C15 structure for the f orbitals when $ze\overline{r^6}/a^7$ 5 times smaller than $ze\overline{r^4}/a^5$. The y-axis is the energy and the x-axis is the positional parameter of the ligand atoms.

We also perform DFT calculations to investigate the CFS in f systems. We select several f compounds which crystallize in the C15 structure: $LaMg_2$, $LaNi_2$, NdS_2, PrS_2, $PuZn_2$ and $ThMg_2$. We investigate the electronic structure of these compounds with and without SOC and we provide their total and partial DOS of them in the appendix.

Here we discuss as an example the electronic structure of $PuZn_2$ and $ThMg_2$. Figure 5.7 and 5.8 show the total and partial DOS of $PuZn_2$ and $ThMg_2$, respectively. The partial DOS of f levels is shown in blue. The comparison between these two figures reveals that the f levels of $PuZn_2$ are more localized than the f levels of $ThMg_2$. It is clear that the 5f levels of both compounds are not as localized as the d levels of $TiBe_2$ and $ZrZn_2$, however. Inclusion of SOC lifts the degeneracies which can be seen in Figure 5.7b and 5.8b. This observation is valid also for other compounds

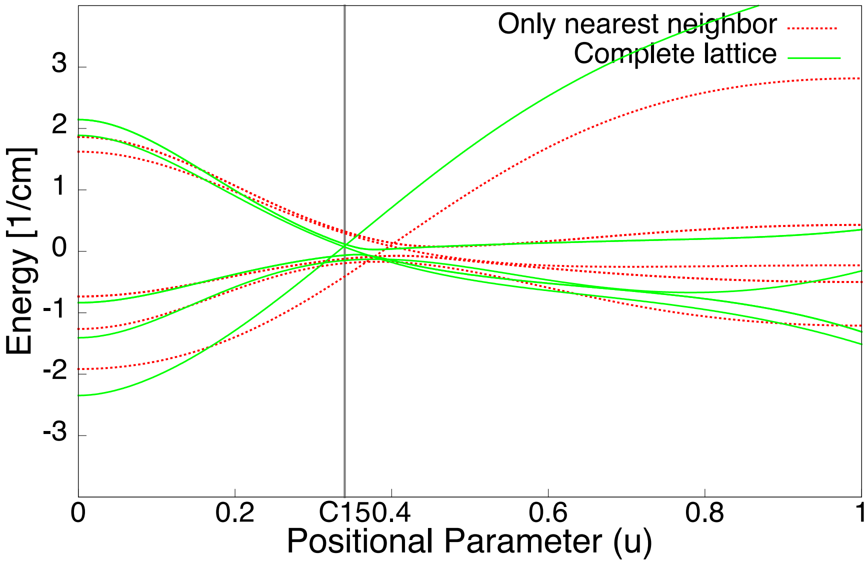

Figure 5.6: Evolution of energy eigenvalues from octahedral to tetrahedral symmetry via C15 structure for the f orbitals when $ze\overline{r^4}/a^5$ and $ze\overline{r^6}/a^7$ are taken as equal. The y-axis is the energy and the x-axis is the positional parameter of ligand atoms.

in, especially, the lanthanide series. Their DOS' are provided in the appendix.

5.5 Conclusions

In conclusion, the unusual occurrence of magnetism in $ZrZn_2$ and $TiBe_2$ can be attributed to the special symmetry of the C15 structure. This leads to a vanishing influence of the non-transition metals on the d states, leading to the unusual narrow peak in the DOS. The point-charge model employed here is expected to give a reliable description in case of coordination by spherical atoms. So, what happens in the case of coordination by non-spherical main-group elements? Enz and Matthias[8] studied the partial substitution of Zn_2 in $ZrZn_2$ by CuAl and found the ferromagnetism is lost. This is exactly what is to be expected with the introduction of the non-spherical aluminium in the lattice.

The CFS in *f*-electron compounds is different from that in the *d*-electron compounds. The analytical analysis that we performed for the *f* levels shows that the CFS cannot be described with only one parameter, unlike the case for the *d* levels. The characteristics of CFS for *f* levels do not only depend on the local point symmetry of the compounds but also the ratio between the two terms in Equation 5.14. We also perform DFT calculations on *f*-electron compounds and observe that it is hard to make a general conclusion about the characteristics of the CFS for the *f* levels.

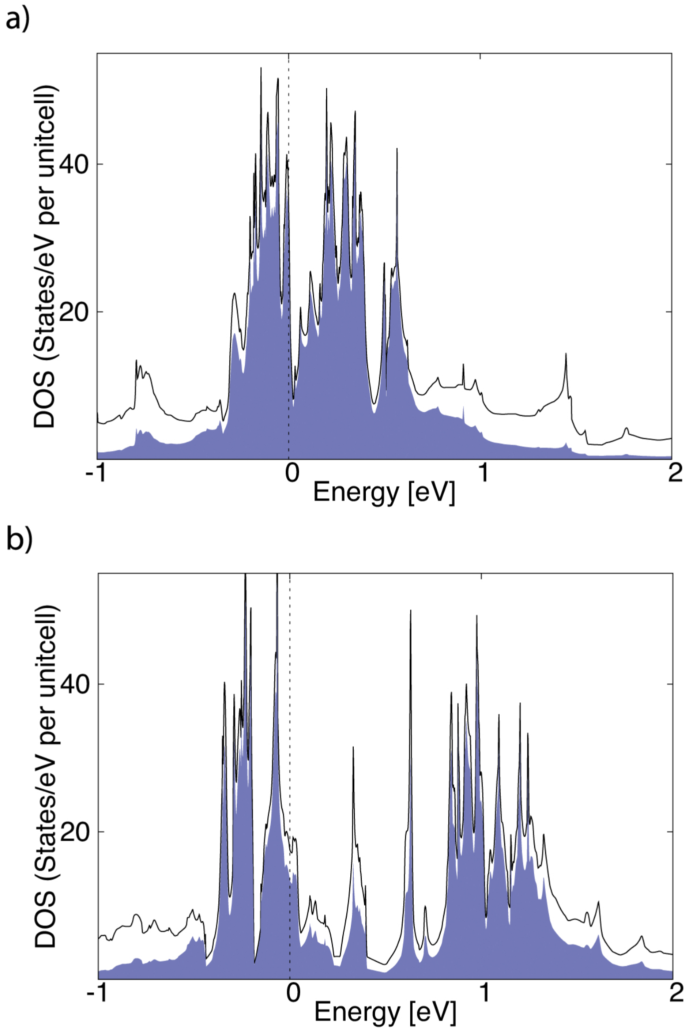

Figure 5.7: The total and the partial DOS of $PuZn_2$ a) without and b) with SOC. The partial DOS of the *f* orbitals is shown in blue. The Fermi level is at 0 eV.

This is an expected observation. DFT calculations also show that the SOC is more prominent in the 5*f* than in the 4*f* compounds. In addition, the 5f levels are not as localized as are the *d* levels in the C15 structure.

Magnetism is one of the manifestations of a high DOS at the Fermi energy in a solid. Superconductivity and heavy Fermion behavior have the same origin. More research in these areas is needed.

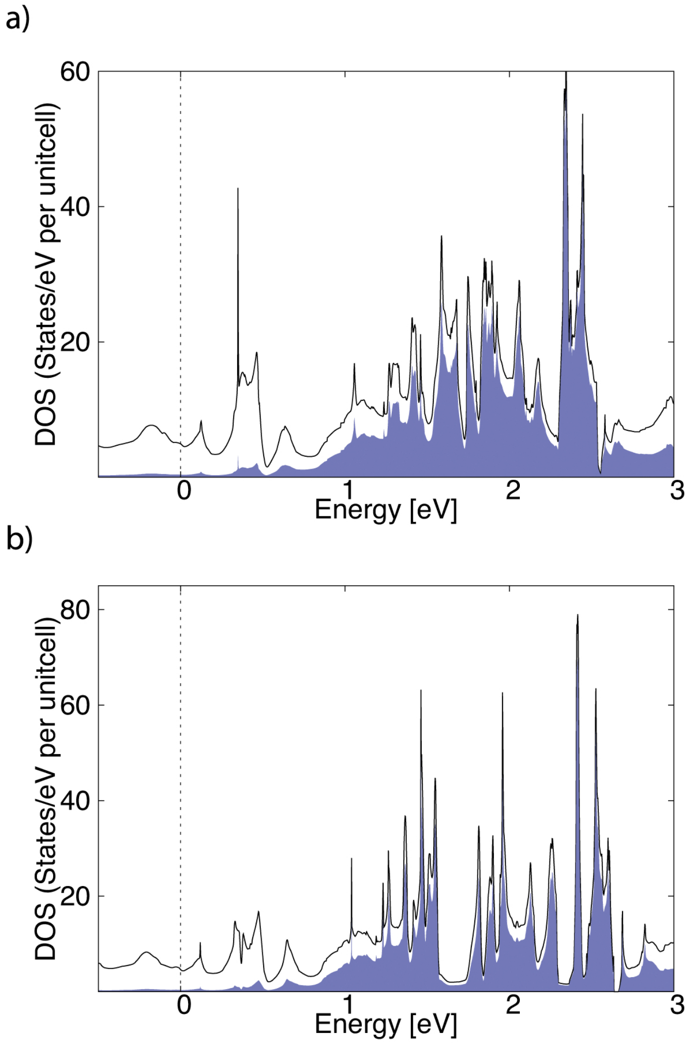

Figure 5.8: The total and the partial DOS of $ThMg_2$ a) without and b) with SOC. The partial DOS of the f orbitals is shown in blue. The Fermi level is at 0 eV.

Bibliography

1. J. Kanamori and Y. Teraoka, Journal of Magnetism and Magnetic Materials **10**, 217 (1979).
2. A. R. Williams, V. L. Moruzzi, C. D. Gelatt Jr. and J. Kübler, Journal of Magnetism and Magnetic Materials **31-4**, 88 (1983).
3. M. van Schilfgaarde, I. A. Abrikosov and B. Johansson, Nature **400**, 46 (1999).
4. N. H. Dung, Z. Q. Ou, L. Caron, L. Zhang, D. T. C. Thanh, G. A. de Wijs, R. A. de Groot, K. H. J. Buschow and E. Brück, Advanced Energy Materials **1**, 1215 (2011).
5. B. T. Matthias and R. M. Bozorth, Phys. Rev. **109**, 604 (1958).
6. P. G. Mattocks and D. Melville, Journal of Physics F: Metal Physics **8**, 1291 (1978).
7. G. S. Knapp, F. Y. Fradin and H. V. Culbert, Journal of Applied Physics **42**, 1341 (1971).
8. C. P. Enz and B. T. Matthias, Science **201**, 828 (1978).
9. R. A. de Groot, F. M. Mueller and D. D. Koelling, Journal of Physics F: Metal Physics **10**, L235 (1980).
10. T. Jarlborg, A. F. Freeman, D. D. Koelling, Journal of Magnetism and Magnetic Materials **23**, 291 (1981).
11. B. T. Matthias, A. L. Giorgi, V. O. Struebing and J. L. Smith, Physics Letters A **69**, 221 (1978).
12. T. Jeong, A. Kyker and W. E. Pickett, Phys. Rev. B **73**, 115106 (2006).
13. A. L. Giorgi, B. T. Matthias, G. R. Stewart, F. Acker and J. L. Smith, Solid State Communications **32**, 455 (1979).
14. J. L. Smith, Physica B+C **107**, 251 (1981).
15. A. L. Giorgi and G. R. Stewart, Solid State Communications **44**, 1465 (1982).

16. B. N. Figgis, Introduction to Ligand Fields, Interscience (1966).
17. C. J. Ballhausen, Introduction to Ligand Field Theory, McGraw-Hill Book Company (1962).
18. P. Hohenberg and W. Kohn, Phys. Rev. **136**, B864 (1964).
19. W. Kohn and L. J. Sham, Phys. Rev. **140**, A1133 (1965).
20. G. Kresse and J. Furthmüller, Phys. Rev. B **54**, 11169 (1996).
21. G. Kresse and J. Furthmüller, Comput. Mat. Sci. **6**, 15 (1996).
22. P. E. Blöchl. Phys. Rev. B **50**, 17953 (1994).
23. G. Kresse and D. Joubert. Phys. Rev. B **59**, 1758 (1999).
24. J. P. Perdew, K. Burke, and M. Ernzerhof. Phys. Rev. Lett. **77**, 3865 (1996).

Appendices

APPENDIX A

Appendix for Chapter 4

A.1 W doped RuO_2 (110) Surfaces

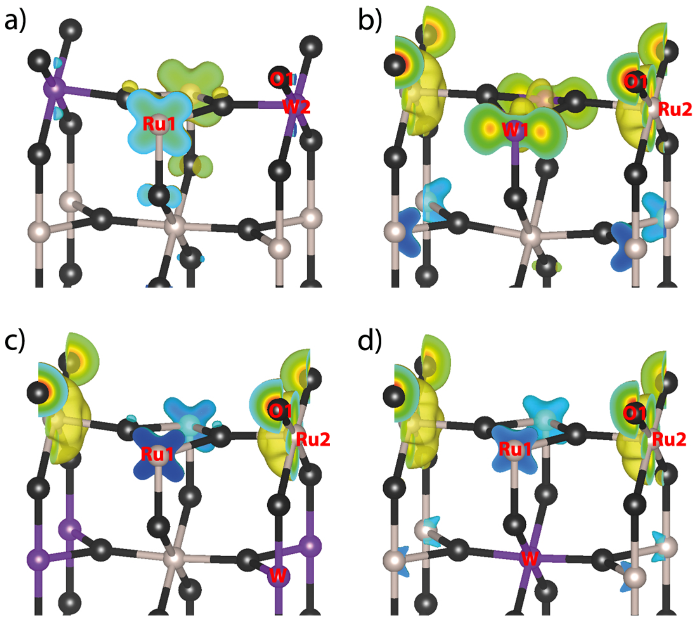

Figure A.1: 1×1 RuO_2 (110) surfaces doped with 1 tungsten. The local magnetic moments of the surface atoms and total energies of the slabs are listed in Table A.1.

Table A.1: The local magnetic moments of the surface atoms and the total energies of 1×1 RuO_2 (110) surfaces shown in Figure A.1. The minimum energy configuration is colored.

	Energy (eV/unit cell)	Magnetic Moment (μ_B)				
		Ru1	Ru2	W1	W2	O1
Bare Surface		-0.18	0.62	—	—	0.19
a	-182.38494	0.22	—	—	-0.07	0.00
b	-181.46830	—	0.86	0.72	—	0.26
c	-181.74418	-0.15	0.64	—	—	0.22
d	-181.58508	-0.14	0.52	—	—	0.17

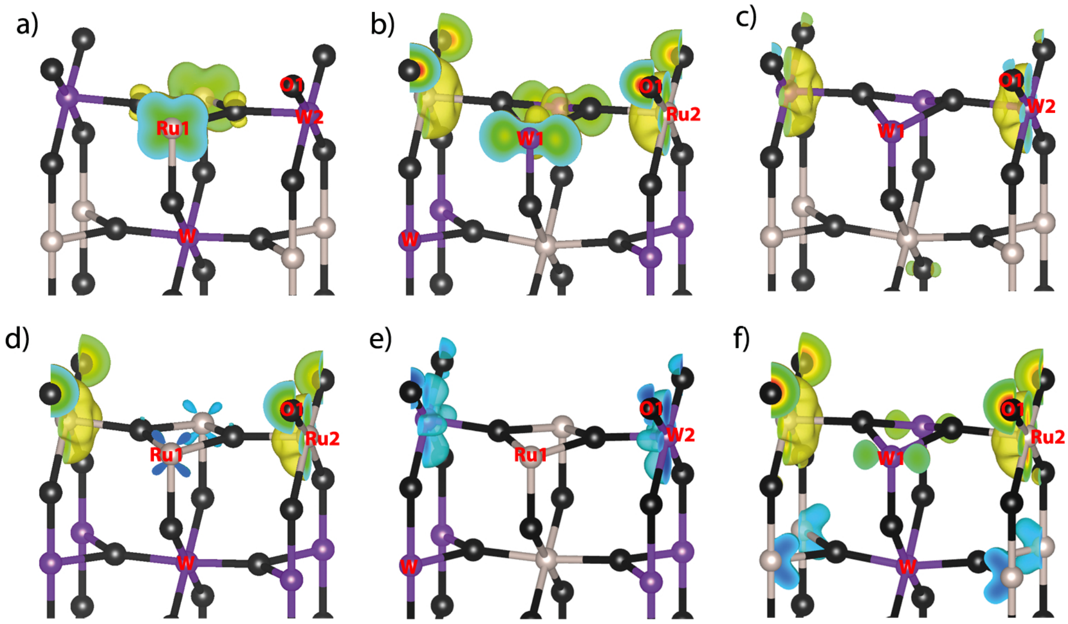

Figure A.2: 1×1 RuO_2 (110) surfaces doped with 2 tungstens. The local magnetic moments of the surface atoms and total energies of the slabs are listed in Table A.2.

Table A.2: The local magnetic moments of the surface atoms and the total energies of 1×1 RuO_2 (110) surfaces shown in Figure A.2. The minimum energy configuration is colored.

	Energy (eV/unit cell)	Magnetic Moment (μ_B)				
		Ru1	Ru2	W1	W2	O1
Bare Surface		-0.18	0.62	—	—	0.19
a	-188.45548	0.33	—	—	0.00	0.00
b	-187.61038	—	0.92	0.71	—	0.30
c	-187.60469	—	—	0.03	0.36	0.00
d	-187.20088	-0.06	0.38	—	—	0.14
e	-188.36635	0.04	—	—	-0.26	-0.02
d	-186.97516	—	0.73	0.15	—	0.22

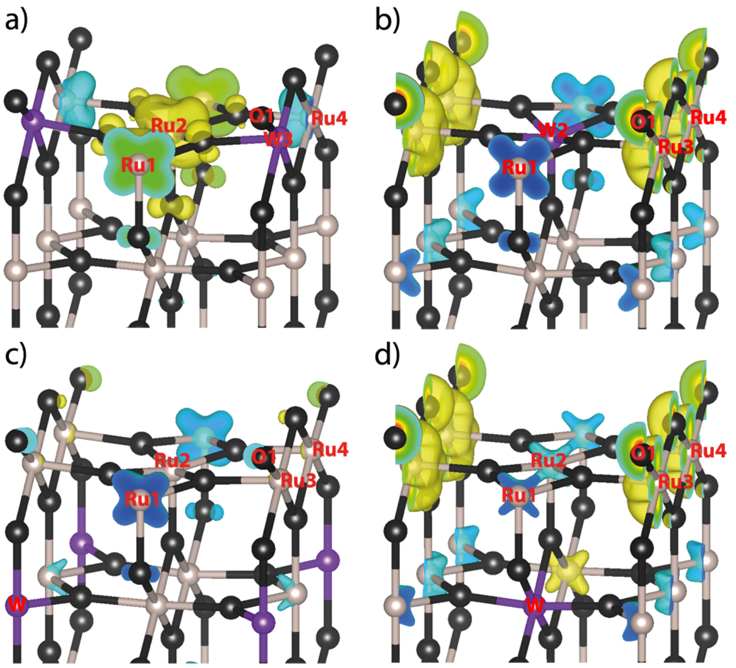

Figure A.3: 2×1 RuO_2 (110) surfaces doped with 1 tungsten. The local magnetic moments of the surface atoms and total energies of the slabs are listed in Table A.3.

Table A.3: The local magnetic moments of the surface atoms and the total energies of 2×1 RuO_2 (110) surfaces shown in Figure A.3. The minimum energy configuration is colored.

	Energy (eV/unit cell)	Magnetic Moment (μ_B)						
		Ru1	Ru2	Ru3	Ru4	W2	W3	O1
Bare Surface		-0.18	-0.18	0.62	0.62	—	—	0.19
a	-358.66581	0.38	0.40	—	-0.19	—	0.01	0.00
b	-357.29827	-0.20	—	0.72	0.72	-0.06	—	0.21
c	-357.50455	-0.13	-0.03	0.07	0.07	—	—	0.03
d	-357.32765	-0.10	-0.10	0.57	0.58	—	—	0.18

A.2 Ni doped RuO$_2$ (110) Surfaces

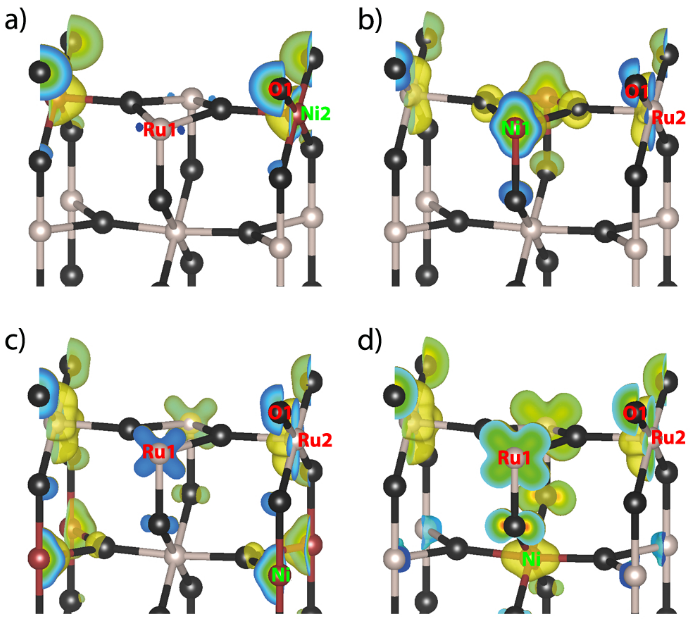

Figure A.4: 1×1 RuO$_2$ (110) surfaces doped with 1 nickel. The local magnetic moments of the surface atoms and total energies of the slabs are listed in Table A.4.

Table A.4: The local magnetic moments of the surface atoms and the total energies of 1×1 RuO$_2$ (110) surfaces shown in Figure A.4. The minimum energy configuration is colored.

	Energy (eV/unit cell)	Magnetic Moment (μ_B)				
		Ru1	Ru2	Ni1	Ni2	O1
Bare Surface		-0.18	0.62	—	—	0.19
a	-169.99621	-0.15	—	—	0.78	0.52
b	-171.28015	—	0.36	0.98	—	0.14
c	-170.51115	0.23	0.64	—	—	0.19
d	-170.84345	0.49	0.46	—	—	0.15

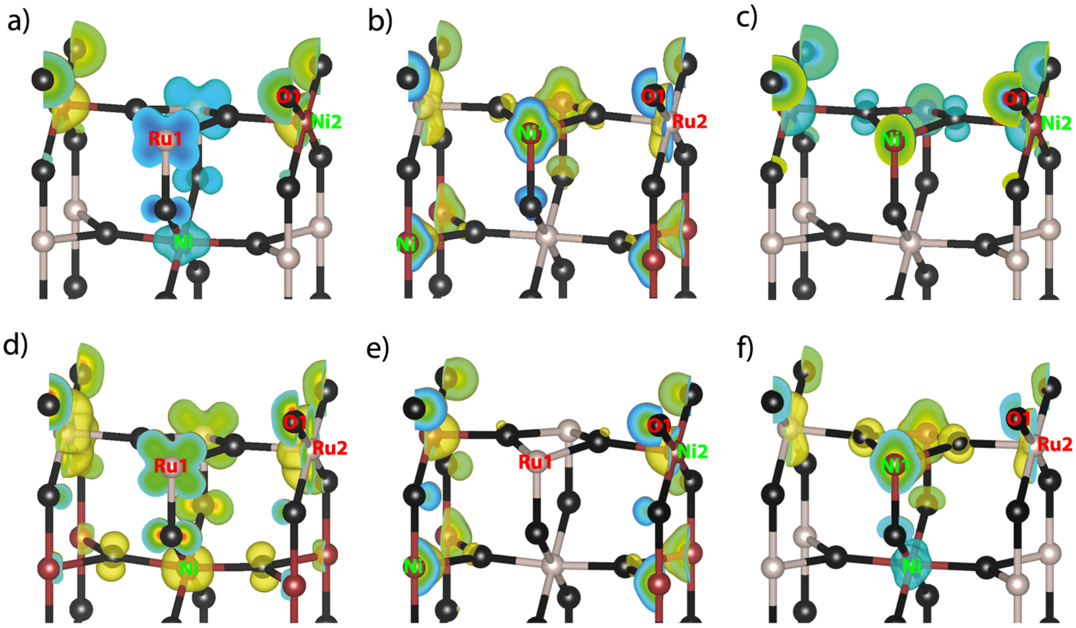

Figure A.5: 1×1 RuO_2 (110) surfaces doped with 2 nickel. The local magnetic moments of the surface atoms and total energies of the slabs are listed in Table A.5.

Table A.5: The local magnetic moments of the surface atoms and the total energies of 1×1 RuO_2 (110) surfaces shown in Figure A.5. The minimum energy configuration is colored.

	Energy (eV/unit cell)	Magnetic Moment (μ_B)				
		Ru1	Ru2	Ni1	Ni2	O1
Bare Surface		-0.18	0.62	—	—	0.19
a	-165.42955	-0.54	—	—	0.87	0.55
b	-166.34546	—	0.48	0.99	—	0.25
c	-165.26297	—	—	-0.25	-0.69	-0.61
d	-165.40864	0.43	0.69	—	—	0.19
e	-164.96375	0.03	—	—	0.49	0.36
f	-166.23092	—	0.28	0.89	—	0.13

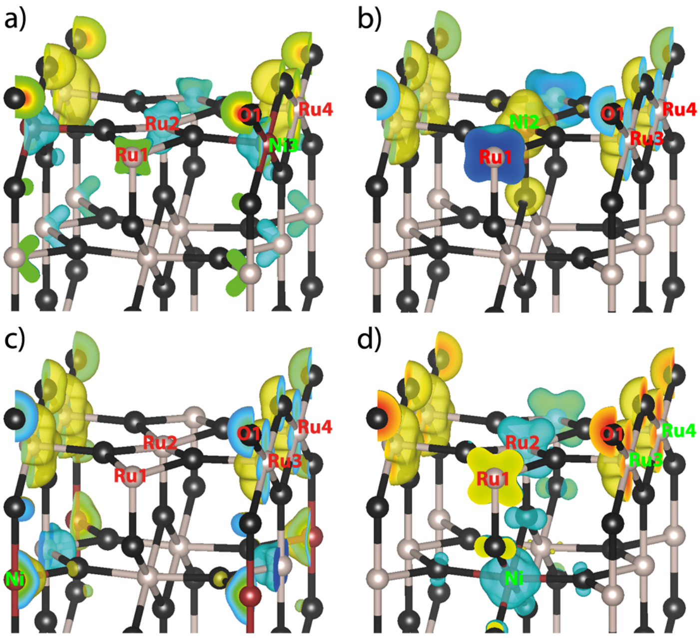

Figure A.6: 2×1 RuO_2 (110) surfaces doped with 1 nickel. The local magnetic moments of the surface atoms and total energies of the slabs are listed in Table A.6.

Table A.6: The local magnetic moments of the surface atoms and the total energies of 2×1 RuO_2 (110) surfaces shown in Figure A.6. The minimum energy configuration is colored.

	Energy (eV/unit cell)	Magnetic Moment (μ_B)						
		Ru1	Ru2	Ru3	Ru4	Ni2	Ni3	O1
Bare Surface		-0.18	-0.18	0.62	0.62	—	—	0.19
a	-346.06071	-0.13	-0.12	—	0.67	—	-0.24	0.17
b	-347.00535	-0.54	—	0.60	0.60	1.08	—	0.20
c	-346.18273	-0.07	-0.05	0.66	0.66	—	—	0.19
d	-346.39789	-0.30	-0.30	0.59	0.63	—	—	0.19

A.3 Ir doped RuO_2 (110) Surfaces

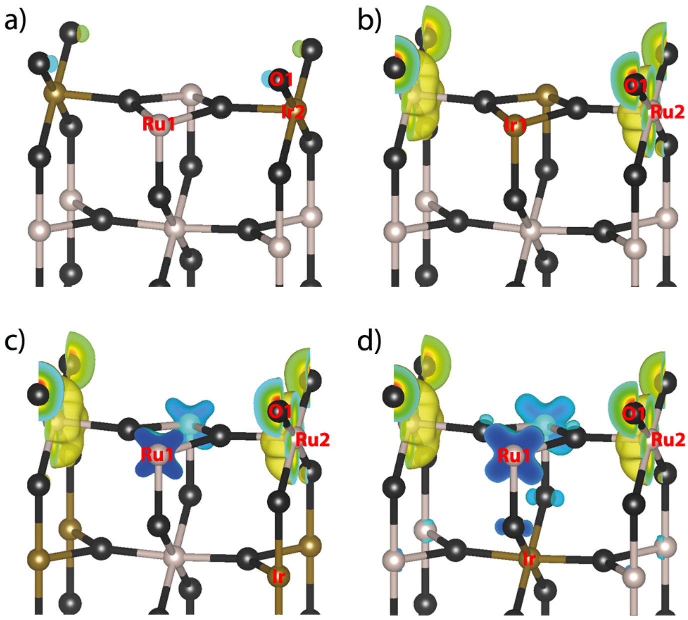

Figure A.7: 1×1 RuO_2 (110) surfaces doped with 1 iridium. The local magnetic moments of the surface atoms and total energies of the slabs are listed in Table A.7.

Table A.7: The local magnetic moments of the surface atoms and the total energies of 1×1 RuO_2 (110) surfaces shown in Figure A.7. The minimum energy configuration is colored.

	Energy (eV/unit cell)	Magnetic Moment (μ_B)				
		Ru1	Ru2	Ir1	Ir2	O1
Bare Surface		-0.18	0.62	—	—	0.19
a	-174.30491	-0.05	—	—	0.03	0.02
b	-174.06932	—	0.57	-0.05	—	0.18
c	-174.29403	-0.14	0.63	—	—	0.20
d	-174.16114	-0.22	0.60	—	—	0.18

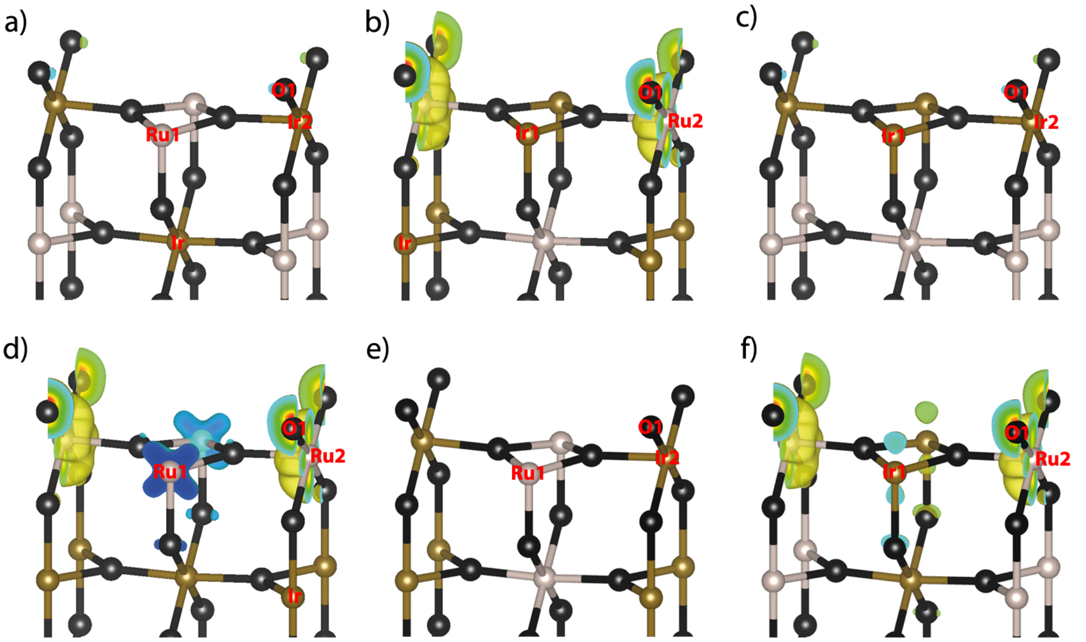

Figure A.8: 1×1 RuO$_2$ (110) surfaces doped with 2 iridiums. The local magnetic moments of the surface atoms and total energies of the slabs are listed in Table A.8.

Table A.8: The local magnetic moments of the surface atoms and the total energies of 1×1 RuO$_2$ (110) surfaces shown in Figure A.8. The minimum energy configuration is colored.

	Energy (eV/unit cell)	Magnetic Moment (μ_B)				
		Ru1	Ru2	Ir1	Ir2	O1
Bare Surface		-0.18	0.62	—	—	0.19
a	-173.00999	-0.02	—	—	0.02	0.01
b	-172.89561	—	0.58	-0.03	—	0.19
c	-172.88614	—	—	-0.01	0.02	0.01
d	-172.89809	-0.17	0.65	—	—	0.20
e	-173.13073	-0.05	—	—	0.01	0.01
f	-172.73187	—	0.56	0.07	—	0.17

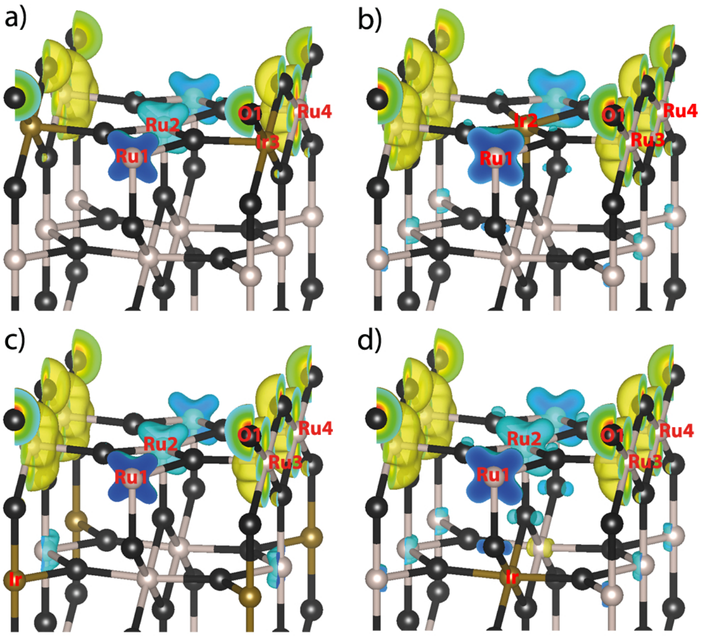

Figure A.9: 2×1 RuO_2 (110) surfaces doped with 1 iridium. The local magnetic moments of the surface atoms and total energies of the slabs are listed in Table A.9.

Table A.9: The local magnetic moments of the surface atoms and the total energies of 2×1 RuO_2 (110) surfaces shown in Figure A.9. The minimum energy configuration is colored.

	Energy (eV/unit cell)	Magnetic Moment (μ_B)						
		Ru1	Ru2	Ru3	Ru4	Ir2	Ir3	O1
Bare Surface		-0.18	-0.18	0.62	0.62	—	—	0.19
a	-349.75479	-0.16	-0.16	—	0.82	—	0.05	0.15
b	-349.55251	-0.25	—	0.61	0.61	-0.05	—	0.19
c	-349.80471	-0.16	-0.16	0.62	0.62	—	—	0.20
d	-349.66673	-0.22	-0.22	0.59	0.62	—	—	0.19

APPENDIX B

Appendix for Chapter 5

B.1 Derivation of crystal field splitting for *d* levels in terms of parameter "*u*"

In order to investigate the evolution of the crystal field splitting (CFS) from octahedral (where $u = 0$) to tetrahedral (where $u = 1$) symmetry, the crystal field potential (CFP) needs to be written in terms of parameter "u". This means that $1/r_{ij}$ should be written in terms of "u"

$$\frac{1}{r_{ij}} = \sum_{n=0}^{\infty} \sum_{m=-n}^{n} \frac{4\pi}{2n+1} \frac{r_<^n}{r_>^{n+1}} Y_{nj}^{m} Y_{ni}^{m^*}. \tag{B.1}$$

In Equation B.1, the second spherical harmonic is from the ligand atoms and the first one is from the d or f orbitals of the central atom. $r_<$ is defined as the radius of the orbitals. It will be replaced with "r" in the rest of the appendix. $r_>$ is the distance between the ligand and the central atom. It will be replaced with "a" in the rest of the appendix. The matrix elements, and consequently the splitting of the d and f levels because of the ligands, can be obtained with the help of Equation B.1.

A general definition for the spherical harmonic is

$$Y_n^m(\theta, \phi) = (2\pi)^{-1/2} e^{im\phi} \Theta_n^m, \tag{B.2}$$

where Θ_n^m is a Legendre polynomial.

As discussed before, in this formalism there are two "sources" of spherical harmonics; one is from the ligands and the other one is from the orbitals. In order to distinguish between these two, we write the spherical harmonics from potential as $Y_n^m(\theta, \phi)$ and from the orbitals as $Y_l^{m_l}(\theta, \phi)$.

Table B.1: The positions of the nearest neighbor atoms of the central atom in the C15 structure in terms of parameter “u”. The first three columns correspond to the positions of atoms in the Cartesian coordinates. The next four columns correspond to the positions in the spherical coordinates. When $u = 0$ the coordinates are for the octahedral symmetry and when $u = 1$ they are for the tetrahedral symmetry.

	x	y	z	sinθ	cosθ	sinϕ	cosϕ
1	u	u	1	$\sqrt{\frac{2u^2}{(2u^2+1)}}$	$\frac{1}{\sqrt{(2u^2+1)}}$	$\frac{1}{\sqrt{2}}$	$\frac{1}{\sqrt{2}}$
2	u	-u	-1	$\sqrt{\frac{2u^2}{(2u^2+1)}}$	$\frac{1}{\sqrt{(2u^2+1)}}$	-$\frac{1}{\sqrt{2}}$	$\frac{1}{\sqrt{2}}$
3	-u	u	-1	$\sqrt{\frac{2u^2}{(2u^2+1)}}$	$\frac{1}{\sqrt{(2u^2+1)}}$	$\frac{1}{\sqrt{2}}$	-$\frac{1}{\sqrt{2}}$
4	-u	-u	1	$\sqrt{\frac{2u^2}{(2u^2+1)}}$	$\frac{1}{\sqrt{(2u^2+1)}}$	-$\frac{1}{\sqrt{2}}$	-$\frac{1}{\sqrt{2}}$
5	1	u	u	$\sqrt{\frac{(1+u^2)}{(2u^2+1)}}$	$\frac{u}{\sqrt{(2u^2+1)}}$	$\frac{u}{\sqrt{u^2+1}}$	$\frac{1}{\sqrt{u^2+1}}$
6	1	-u	-u	$\sqrt{\frac{(1+u^2)}{(2u^2+1)}}$	$\frac{-u}{\sqrt{(2u^2+1)}}$	$\frac{-u}{\sqrt{u^2+1}}$	$\frac{1}{\sqrt{u^2+1}}$
7	-1	u	-u	$\sqrt{\frac{(1+u^2)}{(2u^2+1)}}$	$\frac{-u}{\sqrt{(2u^2+1)}}$	$\frac{u}{\sqrt{u^2+1}}$	$\frac{-1}{\sqrt{u^2+1}}$
8	-1	-u	u	$\sqrt{\frac{(1+u^2)}{(2u^2+1)}}$	$\frac{u}{\sqrt{(2u^2+1)}}$	$\frac{-u}{\sqrt{u^2+1}}$	$\frac{-1}{\sqrt{u^2+1}}$
9	u	1	u	$\sqrt{\frac{(1+u^2)}{(2u^2+1)}}$	$\frac{u}{\sqrt{(2u^2+1)}}$	$\frac{1}{\sqrt{u^2+1}}$	$\frac{u}{\sqrt{u^2+1}}$
10	u	-1	-u	$\sqrt{\frac{(1+u^2)}{(2u^2+1)}}$	$\frac{-u}{\sqrt{(2u^2+1)}}$	$\frac{-1}{\sqrt{u^2+1}}$	$\frac{u}{\sqrt{u^2+1}}$
11	-u	1	-u	$\sqrt{\frac{(1+u^2)}{(2u^2+1)}}$	$\frac{-u}{\sqrt{(2u^2+1)}}$	$\frac{1}{\sqrt{u^2+1}}$	$\frac{-u}{\sqrt{u^2+1}}$
12	-u	-1	u	$\sqrt{\frac{(1+u^2)}{(2u^2+1)}}$	$\frac{u}{\sqrt{(2u^2+1)}}$	$\frac{-1}{\sqrt{u^2+1}}$	$\frac{-u}{\sqrt{u^2+1}}$

For the d orbitals ($l = 2$), there is no contribution from the terms with higher n than 4 because of the following relation

$$\int_0^{\pi}\int_0^{2\pi} Y_l^{m_l^*} Y_n^m Y_l^{m_l'} \sin\theta d\theta d\phi = 0 \text{ if } n > 4. \tag{B.3}$$

There is no contribution to the sum in Equation B.1 when n is odd. Therefore $1/r_{ij}$ should be expanded for only n=0, 2 and 4 (for the d electrons). The odd spherical harmonics do not have an effect on the splitting of the orbitals

$$\frac{1}{r_{ij}} = 4\pi\frac{1}{a}Y_0^0 Y_0^{0^*} + \sum_{m=-2}^{2}\frac{4\pi}{5}\frac{r^2}{a^3}Y_2^m Y_2^{m^*} + \sum_{m=-4}^{4}\frac{4\pi}{9}\frac{r^4}{a^5}Y_4^m Y_4^{m^*}. \tag{B.4}$$

The first term in Equation B.4 is for $n = 0$, the second one is for $n = 2$ and the last one is for $n = 4$. If we take the contributions of all the nearest neighbor atoms to this sum, several terms cancel each other. The terms that give non-zero contribution to the sum are those with Y_0^0, Y_4^0 and $Y_4^{\pm 4}$. The definitions of these spherical harmonics in spherical coordinates are

$$\begin{aligned} Y_0^0(\theta,\phi) &= \frac{1}{2}\sqrt{\frac{1}{\pi}}, \\ Y_4^0(\theta,\phi) &= \frac{3}{16}\sqrt{\frac{1}{\pi}}\left(35\cos^4(\theta) - 30\cos^2(\theta) + 3\right), \\ Y_4^{\pm 4}(\theta,\phi) &= \frac{3}{16}\sqrt{\frac{35}{2\pi}}\left(\sin^4(\theta)\, e^{\pm 4i\phi}\right). \end{aligned} \tag{B.5}$$

The spherical harmonics in equation B.5 can be written in terms of "u" using the coordinates in Table B.1.

$$\begin{aligned} Y_0^0(\theta,\phi) &= \frac{1}{2}\sqrt{\frac{1}{\pi}}, \\ Y_4^0(\theta,\phi) &= \frac{21}{2\sqrt{\pi}}\left(\frac{-u^4 - 6u^2 + 1}{(2u^2+1)^2}\right), \\ Y_4^{\pm 4}(\theta,\phi) &= \frac{3}{2}\sqrt{\frac{35}{2\pi}}\left(\frac{-u^4 - 6u^2 + 1}{(2u^2+1)^2}\right). \end{aligned} \tag{B.6}$$

The definitions which are shown in Equation B.6 can be used to write the CFP in terms of "u"

$$\begin{aligned} V(u) =& \frac{1}{a} + \frac{42\sqrt{\pi}}{9}\frac{ze\overline{r^4}}{a^5}Y_4^0(\theta,\phi)\left(\frac{-u^4 - 6u^2 + 1}{(2u^2+1)^2}\right) \\ &+ \sqrt{\frac{70\pi}{9}}\frac{ze\overline{r^4}}{a^5}\left(Y_4^4(\theta,\phi) + Y_4^{-4}(\theta,\phi)\right)\left(\frac{-u^4 - 6u^2 + 1}{(2u^2+1)^2}\right). \end{aligned} \tag{B.7}$$

The first part of Equation B.7 leads to an equal shift to all the d orbitals. So, it is not necessary to take it into account for the discussion here. In order to find the splitting of the d orbitals, the elements of the secular matrix should be calculated. The matrix elements are

$$\begin{aligned} \langle m_l / V(u) / m_l^{'} \rangle = \int (m_l)^* V(u) (m_l^{'}) d\tau, \\ (m_l) = R_{n,2} Y_2^{m_l}. \end{aligned} \tag{B.8}$$

The "r" part of Equation B.8 can be "integrated" using the following definition

$$\int_0^{\infty} R_{n,l}^* r^s R_{n,l} r^2 dr = \overline{r_{n,l}^s}. \tag{B.9}$$

Using Equation B.9, the matrix elements can be calculated as

$$\begin{aligned} \int (m_l)^* V(u) (m_l^{'}) d\tau =& A \int_0^{\pi} \int_0^{2\pi} Y_2^{ml*} Y_4^0 Y_2^{ml'} \sin\theta d\theta d\phi + \\ & B \int_0^{\pi} \int_0^{2\pi} \left(Y_2^{ml*} Y_4^4 Y_2^{ml'} + Y_2^{ml*} Y_4^{-4} Y_2^{ml'} \right) \sin\theta d\theta d\phi, \end{aligned} \tag{B.10}$$

where

$$\begin{aligned} A =& \frac{42\sqrt{\pi}}{9} \frac{ze\overline{r^4}}{a^5} \left(\frac{-u^4 - 6u^2 + 1}{\left(2u^2+1\right)^2} \right), \\ B =& \sqrt{\frac{70\pi}{9}} \frac{ze\overline{r^4}}{a^5} \left(\frac{-u^4 - 6u^2 + 1}{\left(2u^2+1\right)^2} \right). \end{aligned} \tag{B.11}$$

Equation B.10 can be simplified by using

$$\begin{aligned} \int_0^{2\pi} Y_{l1}^{ml_1} Y_{l2}^{ml_2} Y_{l3}^{ml_3} d\phi \neq& 0, \\ \text{if } m_{l1} + m_{l2} + m_{l3} =& 0. \end{aligned} \tag{B.12}$$

According to Equation B.12 the integral which includes Y_4^0 in Equation B.10 is zero unless $(m_l^{'}) = (m_l)$. The integrals which include Y_4^4 are zero unless $(m_l^{'}) = (-m_l) = -2$ and the integrals which contain Y_4^{-4} are zero unless $(m_l^{'}) = (-m_l) = 2$.

The matrix elements can be written in a simpler form by using Equation B.12. It becomes even simpler if the definition of spherical harmonics (Equation B.2) is used and the integration over ϕ is performed which gives $(2\pi)^{-1/2}$ or 0.

$$\begin{aligned} & \int (m_l)^* V(u) (m_l) d\tau = \\ & \qquad \frac{42}{9\sqrt{2}} \frac{ze\overline{r^4}}{a^5} \left(\frac{-u^4 - 6u^2 + 1}{\left(2u^2+1\right)^2} \right) \int_0^{\pi} \Theta_2^{ml*} \Theta_4^0 \Theta_2^{ml} sin\theta d\theta, \\ & \int (\pm 2)^* V(u) (\mp 2) d\tau = \\ & \qquad \sqrt{\frac{70}{18}} \frac{ze\overline{r^4}}{a^5} \left(\frac{-u^4 - 6u^2 + 1}{\left(2u^2+1\right)^2} \right) \int_0^{\pi} \Theta_2^{2*} \Theta_4^{\pm 4} \Theta_2^{-2} sin\theta d\theta. \end{aligned} \tag{B.13}$$

The integrations in Equation B.13 can be calculated

$$\begin{aligned}\int_0^\pi \Theta_2^{0*}\Theta_4^0\Theta_2^0 sin\theta d\theta &= \frac{\sqrt{18}}{7},\\ \int_0^\pi \Theta_2^{1*}\Theta_4^0\Theta_2^1 sin\theta d\theta &= -\frac{\sqrt{8}}{7},\\ \int_0^\pi \Theta_2^{2*}\Theta_4^0\Theta_2^2 sin\theta d\theta &= \frac{\sqrt{2}}{14},\\ \int_0^\pi \Theta_2^{2*}\Theta_4^4\Theta_2^{-2} sin\theta d\theta &= \frac{\sqrt{35}}{7}.\end{aligned} \tag{B.14}$$

Using the results in Equation B.14, the matrix element can be evaluated

$$\begin{aligned}\int (0)^* V(u)(0)d\tau &= 2\frac{ze\overline{r^4}}{a^5}\left(\frac{-u^4-6u^2+1}{\left(2u^2+1\right)^2}\right),\\ \int (\pm1)^* V(u)(\pm1)d\tau &= \frac{-4}{3}\frac{ze\overline{r^4}}{a^5}\left(\frac{-u^4-6u^2+1}{\left(2u^2+1\right)^2}\right),\\ \int (\pm2)^* V(u)(\pm2)d\tau &= \frac{1}{3}\frac{ze\overline{r^4}}{a^5}\left(\frac{-u^4-6u^2+1}{\left(2u^2+1\right)^2}\right),\\ \int (\pm2)^* V(u)(\mp2)d\tau &= \frac{5}{3}\frac{ze\overline{r^4}}{a^5}\left(\frac{-u^4-6u^2+1}{\left(2u^2+1\right)^2}\right).\end{aligned} \tag{B.15}$$

Then the secular matrix is

$$\begin{array}{c|ccccc|} & (2) & (1) & (0) & (-1) & (-2) \\ (2) & D-E & 0 & 0 & 0 & 5D \\ (1) & 0 & -4D-E & 0 & 0 & 0 \\ (0) & 0 & 0 & 6D-E & 0 & 0 \\ (-1) & 0 & 0 & 0 & -4D-E & 0 \\ (-2) & 5D & 0 & 0 & 0 & D-E \end{array} = 0 \tag{B.16}$$

where

$$D = \frac{1}{3}\frac{ze\overline{r_2^4}}{a^5}\left(\frac{-u^4-6u^2+1}{\left(2u^2+1\right)^2}\right). \tag{B.17}$$

The secular matrix has two distinct eigenvalues.

$$\begin{aligned}E1 &= \frac{-4}{3}\frac{ze\overline{r^4}}{a^5}\left(\frac{-u^4-6u^2+1}{\left(2u^2+1\right)^2}\right),\\ E2 &= \frac{6}{3}\frac{ze\overline{r^4}}{a^5}\left(\frac{-u^4-6u^2+1}{\left(2u^2+1\right)^2}\right).\end{aligned} \tag{B.18}$$

B.2 Derivation of crystal field splitting for f levels in terms of parameter “u”

For f orbitals the expansion of $1/r_{ij}$ should be continued till $n = 6$ as shown in Equation B.19.

$$\begin{aligned}\frac{1}{r_{ij}} = \frac{4\pi}{a}Y_0^0Y_0^{0^*} + \sum_{m=-2}^{2}\frac{4\pi}{5}\frac{r^2}{a^3}Y_2^mY_2^{m^*} + \\ \sum_{m=-4}^{4}\frac{4\pi}{9}\frac{r^4}{a^5}Y_4^mY_4^{m^*} + \sum_{m=-6}^{6}\frac{4\pi}{13}\frac{r^6}{a^7}Y_6^mY_6^{m^*}.\end{aligned} \tag{B.19}$$

The first three terms are the same as for the d electrons. We have to deal with the last term. There are only two terms which contribute to this sum as given in page 41 of reference 1, these are

$$\begin{aligned}Y_6^0(\theta,\phi) =& \frac{1}{32}\sqrt{\frac{13}{\pi}}\left(231cos^6(\theta) - 315cos^4(\theta) + 105cos^2(\theta) - 5\right),\\ Y_6^{\pm 4}(\theta,\phi) =& \frac{3}{32}\sqrt{\frac{91}{2\pi}}e^{\pm 4i\phi}sin^4(\theta)\left(11cos^2(\theta) - 1\right).\end{aligned} \tag{B.20}$$

The spherical harmonics which are shown in Equation B.20 can be written in terms of “u” by taking into account all the nearest neighbor atoms. Their coordinates are shown in Table B.1.

$$\begin{aligned}Y_6^0(\theta,\phi) &= -\frac{3}{4}\sqrt{\frac{13}{\pi}}\left(\frac{13u^6 - 75u^4 + 15u^2 - 1}{(2u^2+1)^3}\right),\\ Y_6^{\pm 4}(\theta,\phi) &= \frac{3}{4}\sqrt{\frac{91}{2\pi}}\left(\frac{13u^6 - 75u^4 + 15u^2 - 1}{(2u^2+1)^3}\right).\end{aligned} \tag{B.21}$$

The CFP for the f orbitals can be written in terms of the “u” as

$$\begin{aligned}V(u) =& \frac{1}{a} + \frac{42\sqrt{\pi}}{9}\frac{ze\overline{r^4}}{a^5}Y_4^0(\theta,\phi)\left(\frac{-u^4 - 6u^2 + 1}{(2u^2+1)^2}\right)\\ &+ \sqrt{\frac{70\pi}{9}}\frac{ze\overline{r^4}}{a^5}(Y_4^4(\theta,\phi) + Y_4^{-4}(\theta,\phi))\left(\frac{-u^4 - 6u^2 + 1}{(2u^2+1)^2}\right)\\ &- \frac{3}{13}\sqrt{13\pi}\frac{ze\overline{r^6}}{a^7}Y_6^0(\theta,\phi)\left(\frac{13u^6 - 75u^4 + 15u^2 - 1}{(2u^2+1)^3}\right)\\ &-\frac{3}{13}\sqrt{\frac{91\pi}{2}}\frac{ze\overline{r^6}}{a^7}(Y_6^4(\theta,\phi) + Y_6^{-4}(\theta,\phi))\left(\frac{13u^6 - 75u^4 + 15u^2 - 1}{(2u^2+1)^3}\right).\end{aligned} \tag{B.22}$$

In order to investigate the evolution of the energies of f orbitals from octahedral to tetrahedral symmetry, the secular determinant of a 7 × 7 matrix should be constructed. With the help of the analysis which is performed for the free ion energy levels in the reference 1, we calculate the elements of the secular matrix and obtain the eigenvalues using a Mathematica code. The matrix is in the following form

$$\begin{array}{c|ccccccc|}
 & (3) & (2) & (1) & (0) & (-1) & (-2) & (-3) \\
(3) & H_{33}-E & 0 & 0 & 0 & H_{3-1} & 0 & 0 \\
(2) & 0 & H_{22}-E & 0 & 0 & 0 & H_{2-2} & 0 \\
(1) & 0 & 0 & H_{11}-E & 0 & 0 & 0 & H_{1-3} \\
(0) & 0 & 0 & 0 & H_{00}-E & 0 & 0 & 0 \\
(-1) & H_{-13} & 0 & 0 & 0 & H_{-1-1}-E & 0 & 0 \\
(-2) & 0 & H_{-22} & 0 & 0 & 0 & H_{-2-2}-E & 0 \\
(-3) & 0 & 0 & H_{-31} & 0 & 0 & 0 & H_{-3-3}-E
\end{array} = 0 \tag{B.23}$$

where

$$\begin{aligned}
H_{33} = H_{-3-3} &= -\frac{7}{11}A - \frac{5}{286}B, \\
H_{22} = H_{-2-2} &= \frac{49}{33}A + \frac{15}{143}B, \\
H_{11} = H_{-1-1} &= -\frac{7}{33}A - \frac{75}{286}B, \\
H_{00} &= -\frac{14}{11}A - \frac{50}{143}B, \\
H_{3-1} = H_{-13} &= \frac{7}{11}\sqrt{\frac{5}{3}}A + \frac{35\sqrt{15}}{286}B, \\
H_{2-2} = H_{-22} &= -\frac{35}{33}A + \frac{105}{143}B, \\
H_{1-3} = H_{-31} &= \frac{7}{11}\sqrt{\frac{5}{3}}A + \frac{35\sqrt{15}}{286}B,
\end{aligned} \tag{B.24}$$

and

$$\begin{aligned}
A &= \frac{ze\overline{r^4}}{a^5} * \left(\frac{-u^4-6u^2+1}{(2u^2+1)^2}\right), \\
B &= \frac{ze\overline{r^6}}{a^7} * \left(\frac{13u^6-75u^4+15u^2-1}{(2u^2+1)^3}\right).
\end{aligned} \tag{B.25}$$

The diagonalization of the matrix gives 5 distinct eigenvalues

$$\begin{aligned}
E1 &= \frac{2}{143}(182A - 45B), \\
E2 &= \frac{14}{11}A - \frac{50}{143}B, \\
E3 &= \frac{2}{429}(91A + 180B), \\
E4 = E5 &= \frac{1}{429}(-182A - 60B + 7\sqrt{2}\sqrt{1352A^2 + 1365AB + 45B^2}), \\
E6 = E7 &= \frac{1}{429}(-182A - 60B + 7\sqrt{2}\sqrt{1352A^2 + 1365AB + 45B^2}).
\end{aligned} \tag{B.26}$$

B.3 Electronic Structures of Some Lanthanide and Actinide Series Compounds

Table B.2: Lattice constants of the *d* and *f* electron compounds which crystallize in the C15 structure.

	$a = b = c$(Å)	V(Å^3)	α, γ, β
$TiBe_2$ [2]	6.4538	268.81	90
$ZrZn_2$ [3]	7.3969	404.71	90
$PuZn_2$ [4]	7.7600	467.29	90
$ThMg_2$ [5]	8.5700	629.42	90
$LaMg_2$ [6]	8.8090	683.57	90
$LaNi_2$ [6]	7.3120	390.94	90
NdS_2 [7]	8.0110	514.11	90
PrS_2 [8]	8.0760	526.73	90

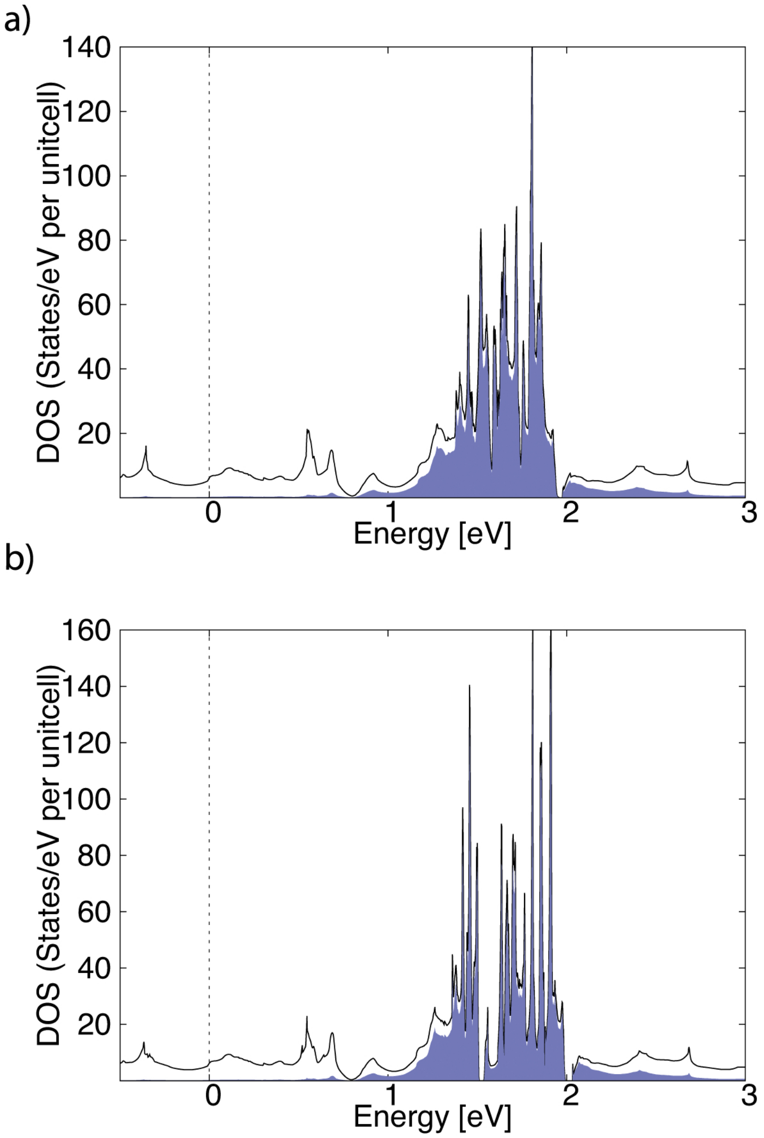

Figure B.1: The total and the partial DOS of $LaMg_2$ a) without and b) with SOC. The partial DOS of the *f* orbitals is shown in blue. The Fermi level is at 0 eV.

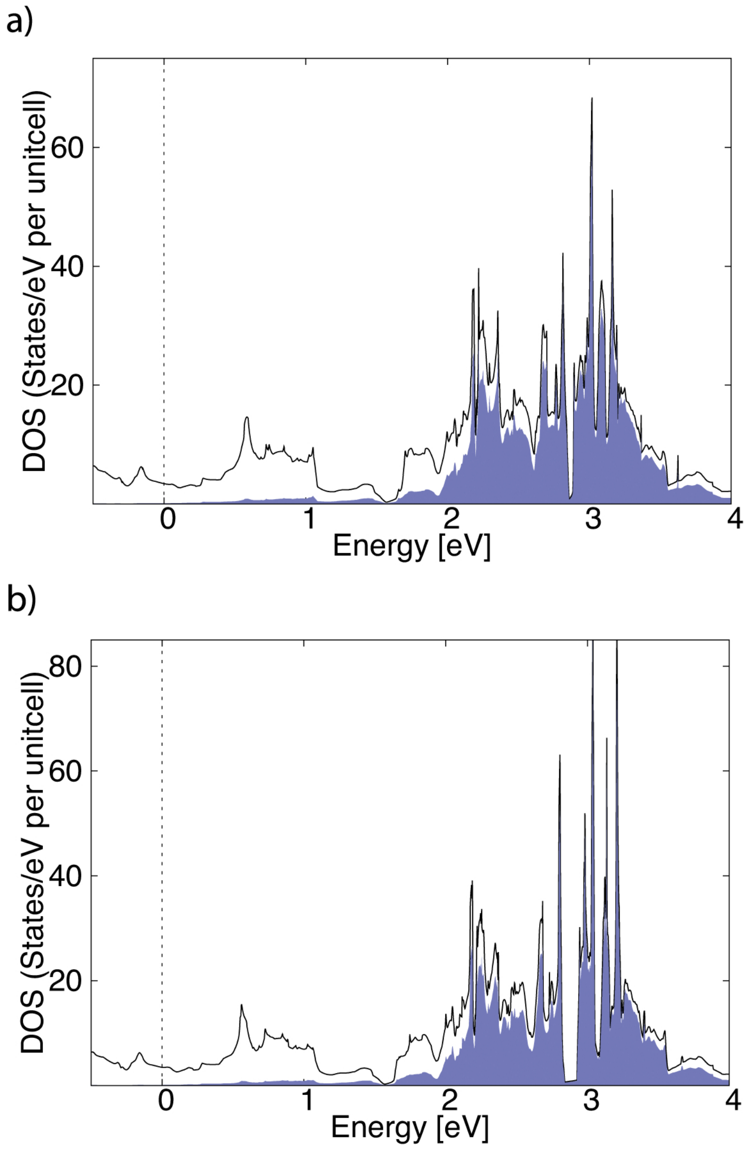

Figure B.2: The total and the partial DOS of $LaNi_2$ a) without and b) with SOC. The partial DOS of the f orbitals is shown in blue. The Fermi level is at 0 eV.

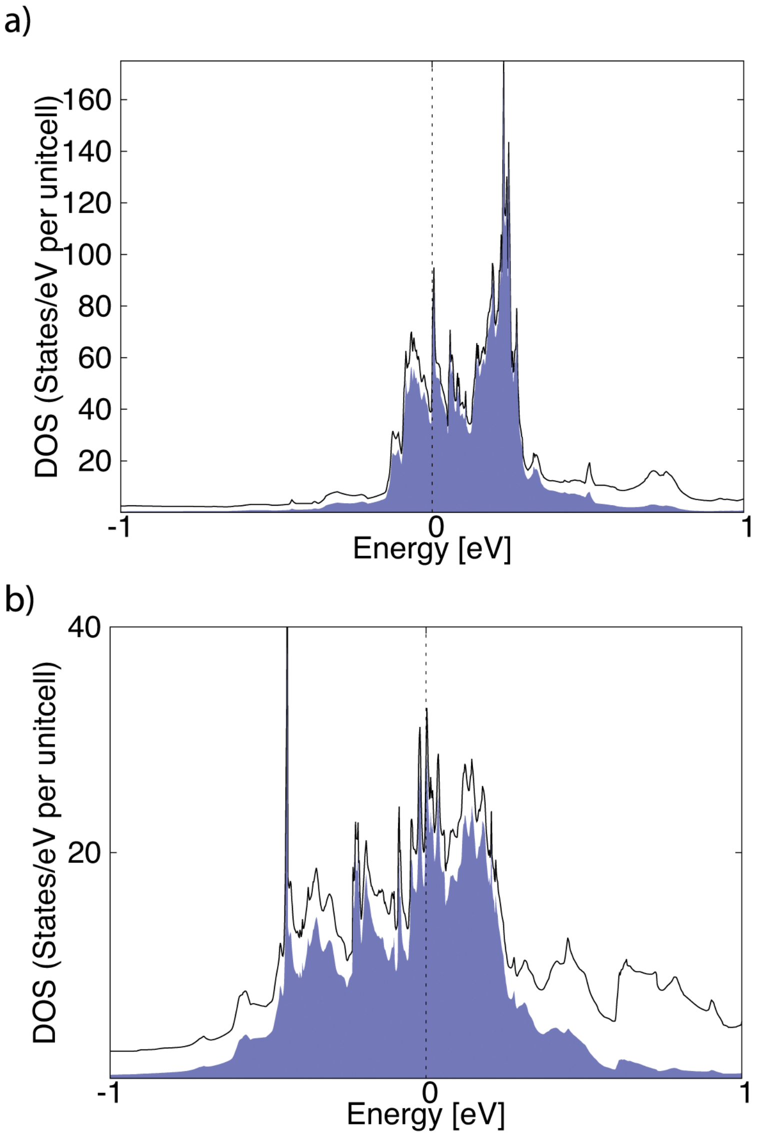

Figure B.3: The total and the partial DOS of NdS_2 a) without and b) with SOC. The partial DOS of the f orbitals is shown in blue. The Fermi level is at 0 eV.

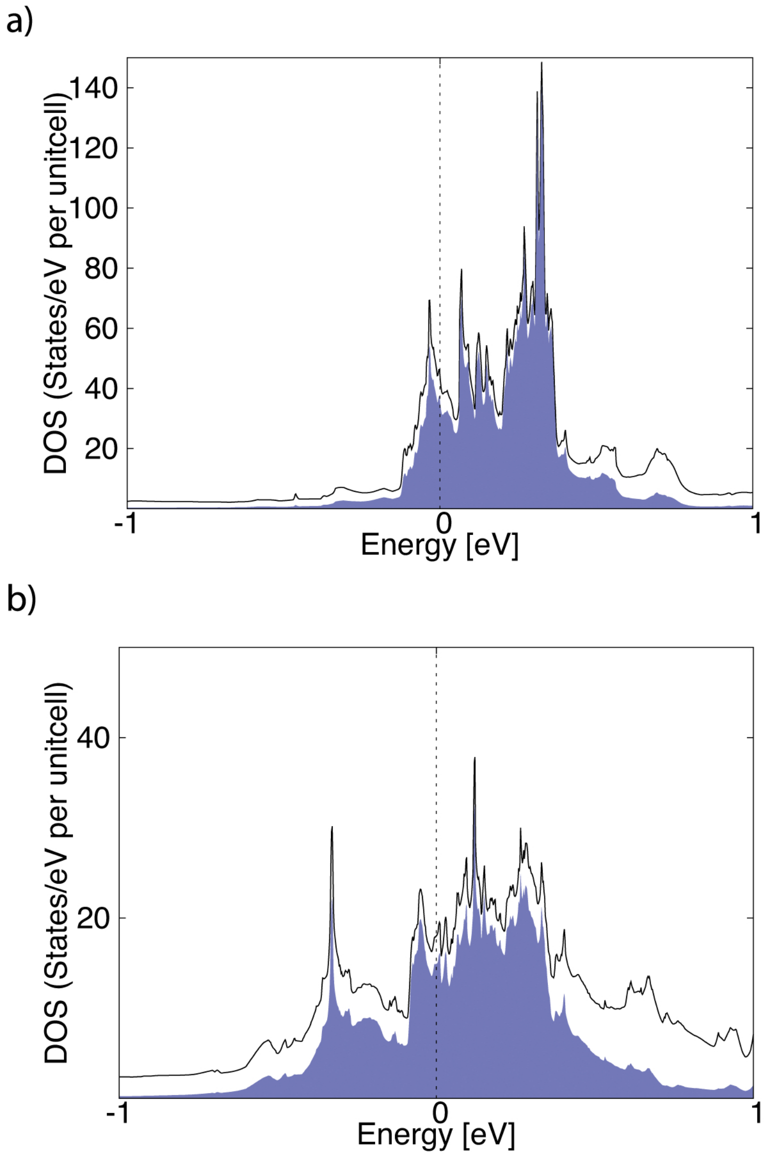

Figure B.4: The total and the partial DOS of PrS_2 a) without and b) with SOC. The partial DOS of the f orbitals is shown in blue. The Fermi level is at 0 eV.

Bibliography

1. B. N. Figgis, Introduction to Ligand Fields, Interscience (1966).
2. A. L. Giorgi and G. R. Stewart, Solid State Communications **44**, 1465 (1982).
3. L. W. M. Schreurs, H. M. Weijers, A. P. J. van Deursen, A. R. de Vroomen. Materials Research Bulletin **24**, 1141 (1989).
4. E. M. Cramer, F. H. Ellinger, C. C. Land, Extract. Phys. Met. Plutonium and Alloys, Symposium, San Francisco, Calif. **1959**, 169 (1960).
5. G. R. Stewart, B. T. Matthias, A. L. Giorgi, E. G. Szklarz, J. L. Smith, Solid State Communications **30**, 709 (1979).
6. A. L. Shilov, Russian Journal of Inorganic Chemistry **36**, 1256 (1991).
7. A. W. Webb and H. T. Hall. Inorganic Chemistry **9**, 1084 (1970).
8. B. le Rolland, P. McMillan, P. Colombet, Comptes Rendus Hebdomadaires des Seances de l'Academie des Sciences **312**, 217 (1991).

Summary

In this thesis, we have investigated physical properties of several condensed matter systems using density functional theory (DFT). In this section, we will summarize the main conclusions of this thesis.

In **Chapter 2**, we have focused on the Dirac-like linear energy dispersion in the band structures of rutile RuO_2 and OsO_2. Linearly dispersing bands in the band structures of materials are not rare, however having one at the Fermi level is quite special. For example, graphene has a Dirac point in its band structure at the Fermi level. This unique band structure of graphene plays a crucial role in its fascinating physical properties.

RuO_2 has abnormal thermal expansion. With increasing temperature, the a and b lattice parameters expand whereas the c lattice parameter shrinks. In order to see the effect of the c/a ratio on the electronic structure of the material, we perform DFT calculations including spin-orbit coupling using different c/a ratios. Our calculations show that the starting point of the linear dispersion relative to the Fermi level depends on the c/a ratio. This could be the reason why the low temperature electron transport of RuO_2 is very sensitive to small variations in the chemical composition. We have also shown that for a specific c/a ratio, the Fermi level and the starting point of Dirac-like dispersion coincide with each other which could be related with high electrical conductivity of RuO_2 at low temperature.

In **Chapter 3**, we have investigated the RuO_2 (110) surface to understand why it is one of the best anodes for electrolysis of water. Chemical reactions are governed by selection rules and angular momentum conservation is one of the basic ones. Angular momentum seems not to be conserved in chemical reactions where only one of the reactants or products is magnetic an example of which is electrolysis of water. Electrolysis of water is important for the production of hydrogen but it has its own drawback; overpotential.

In experiments it is known that the oxygen evolution reaction contributes to the overpotential more than the hydrogen evolution reaction. We predict that on a non-magnetic anode the oxygen molecule, which has a magnetic ground state, can not be produced in its ground state directly. The reason is the conservation of angular momentum and this could be the explanation of the high overvoltage of some anodes. A magnetic anode, however, can provide a mechanism to produce an oxygen molecule in its ground state while respecting angular momentum conservation. Our DFT calculations show that the RuO_2 (110) surface carries magnetization, indeed. We conclude that this could be one of the reasons why RuO_2 is one of the best anodes for electrolysis of water.

Chapter 4 is an extension of the work carried out in **Chapter 3**. In this chapter, we doped the RuO_2 (110) surface with different transition metals. We have obtained a correlation between the experimental oxygen evolution activity of the doped RuO_2 anodes and changes in the surface magnetism of RuO_2 (110) surface because of dopants by using first-principle calculations. We have also investigated the effect of surface magnetism on the molecular oxygen-surface interactions in general.

In **Chapter 5**, we have explored the existence of weak magnetism in $TiBe_2$ and $ZrZn_2$ compounds which crystallize in the C15 structure. We have shown that because of the special symmetry of the C15 structure, no crystal field splitting occurs for the d levels in these compounds. The vanishingly small crystal field splitting leads to a high peak at the Fermi level which fulfills the Stoner criterion of magnetism. That is the reason why $TiBe_2$ and $ZrZn_2$ show weak magnetism. The situation for f levels in the C15 structure is different and more complicated than for the d levels. Our analytical investigation shows that the characteristics of the CFS in f levels are described with two parameters unlike the case of the d levels. The ratio of these two parameters as well as the local point symmetry of the compound determine the characteristics of the CFS in f orbitals. Our DFT calculations on f-electron compounds which crystallize in the C15 structure have shown that the CFS varies from one compound to another which fits our analytical investigation.

Samenvatting

In dit proefschrift hebben we fysische eigenschappen van verscheidene gecondenseerde materie systemen met behulp van dichtheidsfunctionaal theorie (DFT) bestudeerd. In dit hoofdstuk vatten we de belangrijkste conclusies van dit proefschrift samen.

In **Hoofdstuk 2** hebben we ons gericht op de "Dirac"-achtige lineaire energie dispersie in de band structuren van rutiel RuO_2 en OsO_2. Materialen met band structuren met lineaire dispersie zijn niet zeldzaam, maar zo een lineaire dispersie bij het Fermi niveau is nogal bijzonder. Grafeen, bijvoorbeeld, heeft in zijn band structuur een Dirac punt aan het Fermi niveau. Deze unieke eigenschap van grafeen speelt een rol van cruciale betekenis voor zijn fascinerende fysische eigenschappen.

RuO_2 heeft een ongebruikelijke thermische expansie. De rooster parameters a en b nemen toe met toenemende temperatuur, terwijl c afneemt. Om het effect van de c/a verhouding op de elektronen structuur van het materiaal te bestuderen, zijn DFT berekeningen gedaan voor verschillende c/a verhoudingen. In deze berekeningen is het effect van de spin-baan wisselwerking meegenomen. Onze berekeningen laten zien dat het position van de lineaire dispersie ten opzichte van het Fermi niveau afhangt van de c/a verhouding. Dit verklaart waarom het elektron transport in RuO_2 bij lage temperatuur zo gevoelig is voor kleine variaties in de chemische samenstelling. We hebben ook laten zien dat voor een specifieke c/a verhouding het Fermi niveau en het position van de lineaire, Dirac-achtige dispersie samenvallen. Dit kan een relatie hebben het de hoge electrische geleiding van RuO_2 bij lage temperatuur.

In **hoofdstuk 3** hebben we het RuO_2 (110) oppervlak onderzocht, om te begrijpen waarom het een van de beste anode materialen is voor de elektrolyse van water. Chemische reacties zijn aan selectie regels onderhevig. Behoud van impulsmoment is een van de fundamentele selectie regels. Het lijkt alsof impulsmoment niet is behouden in chemische reacties waar slechts één van reactanten en producten magnetisch is. Een voorbeeld hiervan is de elektrolyse van water. Dit proces is belangrijk voor de productie van waterstof.

Experimenteel is bekend dat de vorming van zuurstof meer bijdraagt aan de overpotentiaal dan die van waterstof. Wij voorspellen dat op een niet-magnetische anode het zuurstof molecuul, dat een magnetische grondtoestand heeft, niet direct gemaakt kan worden in de grond-toestand. De reden is het behoud van impulsmoment. Dit zou de hoge overpotentiaal van sommige anodes kunnen verklaren. Echter, een magnetische anode maakt een mechanisme mogelijk dat het zuurstof molecuul in zijn grond toestand produceert en tegelijkertijd het impulsmoment behoudt. Onze DFT berekeningen tonen aan dat het RuO_2 (110) oppervlak inderdaad een magnetisatie heeft. We concluderen dat dit een van de redenen zou kunnen zijn waarom RuO_2 een van de beste anodes is voor de elektrolyse van water.

Hoofdstuk 4 is een uitbreiding van het werk van **hoofdstuk 3**. Hier hebben we het RuO_2 (110) oppervlak gedoteerd met verschillende overgangsmetalen. We hebben een correlatie gevonden tussen de experimentele zuurstof evolutie activiteit van gedoteerde RuO_2 anodes en veranderingen in het oppervlakte magnetisme van het RuO_2 (110) oppervlak zoals gevonden met *first-principles* berekeningen. Ook hebben we het effect van oppervlakte magnetisme op interacties tussen moleculair zuurstof en een oppervlak in zijn algemeenheid onderzocht.

In **hoofdstuk 5** behandelt het voorkomen van zwak magnetisme in de verbindingen als $TiBe_2$ en $ZrZn_2$, welke in de C15 structuur kristalliseren. We laten zien dat vanwege de speciale symmetrie van de C15 structuur er in de verbindingen geen kristal veld splitsing (KVS) van de d niveaus optreedt. De afwezigheid van de kristal veld splitsing resulteert in een hoge piek in de toestandsdichtheid aan het Fermi niveau welke aan het Stoner criterium voldoet. Derhalve vertonen $TiBe_2$ en $ZrZn_2$ zwak magnetisme. Voor de f niveaus in de C15 structuur is de situatie anders en ook ingewikkelder dan voor de d niveaus. Ons analytische onderzoek laat zijn dat de KVS van de f niveaus beschreven wordt door twee parameters, anders dan in het geval van de d niveaus. De verhouding van deze twee parameters en de locale punt groep symmetrie van de verbinding bepalen de karakteristieken van de KVS van de f orbitalen. Onze DFT berekeningen voor f-elektron verbindingen welke in de C15 structuur kristalliseren hebben laten zien dat de KVS varieert van de ene verbinding tot de andere in overeenstemming met ons analytische model.

Acknowledgments

I would like to thank my supervisor Prof. dr. R. A. de Groot and daily supervisor Dr. ir. G. A. de Wijs for their guidance during my PhD period. Rob, your experience and wide knowledge in physics and chemistry always amazed me, I respect your enthusiasm in science and technology. You are not only a good scientist but also a great storyteller, I will always remember your interesting stories with pleasure. Gilles, you have very good insight in physical problems, I would like to thank you for the discussions that we had in your office, they helped me gaining better understanding on various physical concepts. I owe many thanks to you for your efforts during the writing process of my thesis, without your help it would be more difficult to finish this thesis.

During my PhD period I benefited from discussions with good scientists so I thank Dr. Changming Fang and Prof. dr. A. Janner for their contributions to the manuscript.

I would like to thank Prof. dr. ir. G. C. Groenenboom, Prof. dr. A. Fasolino and Prof. dr. T. T. M. Palstra for accepting to be in my reading committee and examination board. Their comments and suggestions definitely improved the manuscript. Especially, I would like to thank Annalisa for the discussions that we had in order to improve the introduction of the thesis. Annalisa, the introduction is more clear and insightful with your comments. I would like to thank Prof. dr. A. Janner, Dr. R. W. A. Havenith and Dr. P. J. M. van Bentum for accepting to be in my examination board.

During these four and half years, I had very enjoyable times in Electronic Structure of Materials (ESM) group so I would like to acknowledge all past and present members of ESM: Filipe, Baomin, Ebrahim, Pegah, Prasenjit and Karol, thank you all for the fun times that we had together and very helpful scientific discussions. Through the end of my PhD ESM and Theoretical Chemistry groups merged, I would like to thank all members of the Theoretical Chemistry group for their kind and welcoming attitude toward us.

Benden bu süreç zarfında yardımlarını esirgemeyen bütün arkadaşlarıma özellikle

Ender, Burak, Özge, Onur, Türkan, Boran, sevgili Pisotti, kardeşlerim Sezgin ve Yetkin, bana her zaman destek olan anne ve babama çok teşekkür ediyorum. Son olarak bu süreçte bana herkesten daha fazla destek olan, biraz da bu tezin var olmasina vesile olan Duygu'ya ne kadar teşekkür etsem azdır. Duygu, bu süreçte hep yanımda olduğun için çok teşekkür ederim.

Curriculum Vitae

Personal Details

Engin Torun
Born on March 2$^{\mathrm{nd}}$, 1983
in Tunceli, Turkey

Education

2010-2015 Ph.D in Physics,
Electronic Structure of Materials, IMM,
Radboud University Nijmegen, The Netherlands
Promoter: Prof. dr. R. A. de Groot
Co-promoter: Dr. ir. G. A. de Wijs

2007-2009 M.Sc. in Physics,
Middle East Technical University, Ankara, Turkey
Promoter: Assoc. prof. dr. Hande Üstunel Toffoli
Co-promoter: Prof. dr. Şinasi Ellialtıoğlu

2002-2007 B.Sc. in Physics,
Middle East Technical University, Ankara, Turkey

2001-2002 Dept. of Basic English, part of the Physics education,
Middle East Technical University, Ankara, Turkey